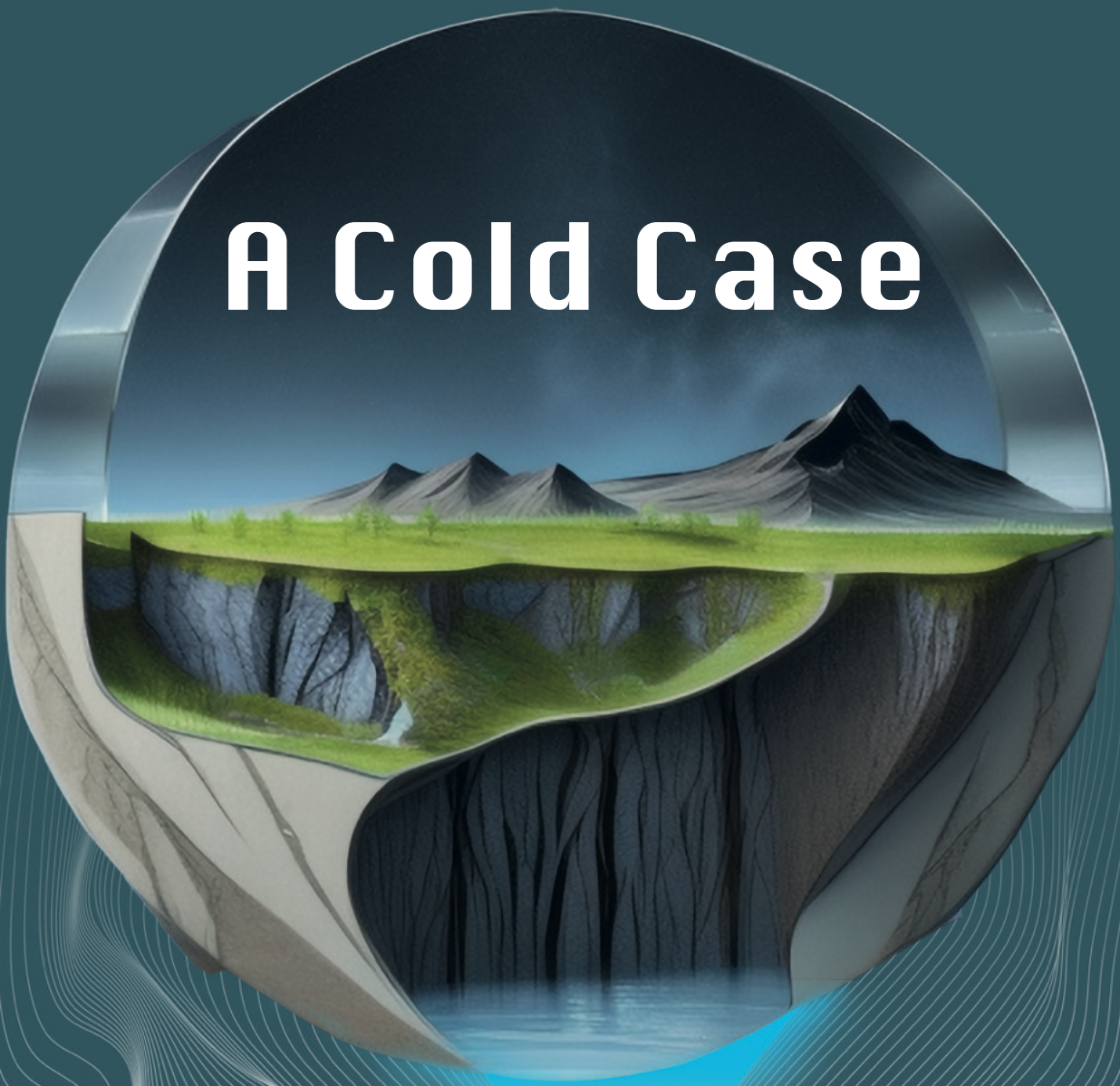

A Cold Case

Reducing the uncertainty in permafrost models and observations

Jelte G.H. de Bruin

Propositions

1 | Reports of model uncertainty should include both data misfit and misfit due to modeller's choices.
(this thesis)

2 | Not correcting permafrost sub-zero resistivity observations for temperature increases the likelihood of data misinterpretation.
(this thesis)

3 | A researcher can only truly appreciate the value of data if they were involved in their collection.

4 | Carbon dioxide emissions should not be an argument for Wageningen University to restrict air travel for scientific field observations of permafrost.

5 | All University employees and PhD candidates should have a personal desk at the office available at all times in order to sustainably conduct research.

6 | In the quest to find international research collaborations, local collaborations are often overlooked.

Propositions belonging to the thesis, entitled:

A Cold Case – Reducing the uncertainty in permafrost models and observations

Jelte de Bruin
Wageningen, 26 June 2024

A Cold Case

Reducing the uncertainty in permafrost models and observations

Jelte Geert Hendrik de Bruin

Thesis committee

Promotors
Dr V. F. Bense
Associate Professor, Hydrology and Environmental Hydraulics Group
Wageningen University & Research

Prof. Dr ir M. J. van der Ploeg
Professor of Hydrology and Environmental Hydraulics Group
Wageningen University & Research

Other members
Prof. Dr J. Wallinga, Wageningen University & Research
Prof. Dr H. K. French, NMBU Ås, Norway
Prof. Dr J. Molson, Laval University, Laval, Canada
Dr M. Langer, Vrije Universiteit, Amsterdam

This research was conducted under the auspices of the Graduate School for Socio-Economic and Natural Sciences of the Environment (SENSE).

A Cold Case

Reducing the uncertainty in permafrost models and observations

Jelte Geert Hendrik de Bruin

Thesis
submitted in fulfilment of the requirements for the degree of doctor
at Wageningen University
by the authority of the Rector Magnificus,
Prof. Dr C. Kroeze,
in the presence of the
Thesis Committee appointed by the Academic Board
to be defended in public
on Wednesday 26 June 2024
at 11:00 am in the Omnia Auditorium.

J. G. H. de Bruin
A Cold Case – Reducing the uncertainty in permafrost models and observations,
vii+138 pages.

PhD thesis, Wageningen University, Wageningen, The Netherlands (2024)
With references, with summaries in English and Dutch

DOI 10.18174/653013
© 2024 J. G. H. de Bruin

Nomenclature

List of abbreviations

ALT	Active Layer Thickness
CALM	Circumpolar Active Layer Monitoring Program
ERT	Electrical Resistivity Tomography
DOC	Dissolved Organic Carbon
HDPE	High-Density Polyethylene
IPCC	Intergovernmental Panel on Climate Change
KGE	Kling–Gupta efficiency
LOI	Loss on Ignition
NMR	Nuclear Magnetic Resonance
OM	Organic Matter
QTP	Qinghai-Tibet Plateau
RMSE	Root Mean Squared Error
SFCC	Soil Freezing Characteristic Curve
TDS	Total Dissolved Solids

List of symbols

D_{50}	Mean particle size (µm)
ϕ	Porosity (-)
λ_a	Thermal conductivity aluminium (W/mK)
λ_h	Thermal conductivity HDPE (W/mK)
λ_{ins}	Thermal conductivity insulation (W/mK)
λ_w	Thermal conductivity water (W/mK)
λ_i	Thermal conductivity ice (W/mK)
λ_s	Thermal conductivity solid grains(W/mK)
λ_v	Bulk thermal conductivity (W/mK)
C_a	Volumetric heat capacity aluminium (J/m^3K)
C_h	Volumetric heat capacity HDPE (J/m^3K)
C_{ins}	Volumetric heat capacity insulation (J/m^3K)
C_w	Volumetric heat capacity water (J/m^3K)
C_i	Volumetric heat capacity ice (J/m^3K)
C_s	Volumetric heat capacity solid grains (J/m^3K)
C_v	Bulk Volumetric heat capacity (J/m^3K)
ρ_w	Density water (kg/m^3)
ρ_i	Density ice (kg/m^3)
ρ_s	Density solid grains, (kg/m^3)
L_i	Latent heat of fusion (J/kgK)
R	Transfer resistances (Ω)
S_w	Water saturation curve (m^3m^{-3})
S_{w0}	Initial water saturation (m^3m^{-3})
S_{wres}	Residual saturation (m^3m^{-3})
S_{wl}	Liquid saturation level (m^3m^{-3})
S_r	Relative saturation (m^3m^{-3})
W	Fitting parameter for freezing function (-)
ρ_{bulk}	Bulk resistivity (Ωm)
ρ_f	Fluid resistivity (Ωm)
ρ_{f_ref}	Reference fluid resistivity (Ωm)
C_0	Porewater TDS concentration (gL^{-1})
C	Liquid water concentration (gL^{-1})
k	Correlation factor fluid resistivity at 25 °C $(\Omega m\, gL^{-1})$
a	Tortuosity factor (-)
m	Cementation exponent (-)
n	Saturation exponent (-)

Contents

Nomenclature v

1 | Introduction 1

2 | Determining thermal properties of permafrost from temperature observations 23

3 | Relating thermal properties to soil characteristics 39

4 | Tracking a freeze-thaw front using Electrical Resistivity Tomography 63

5 | Synthesis 81

6 | Appendices 95

Bibliography 107

Statement of authorship contribution 123

Summary 125

Samenvatting 129

Acknowledgements 133

List of publications 135

Graduate school certificate 136

1

Introduction

1.1 | The global importance of permafrost

1.1.1 | The permafrost environment

Permafrost is often referred to as the "sleeping giant of climate change" Mascarelli (2009), as it contains a vast store of organic carbon that could be released into the atmosphere as the permafrost thaws (Miner et al., 2022; Schuur et al., 2015; Bruhwiler et al., 2021; Strauss et al., 2017). Clearly, permafrost thaw affects not only the local environment, but it has the potential to affect many global cycles as well. What elements define that permafrost and permafrost thaw have such an impact on a global scale? To answer this question we need to have an understanding of the origin of permafrost, and the processes and feedbacks that play a role in permafrost freeze-thaw cycles on a local scale as well as on a global scale.

Permafrost is defined as a soil that has a temperature that continuously remains below 0°C for two or more consecutive years (Van Everdingen et al., 1998). These perennially frozen soils are spread across the Northern Hemisphere, the Qinghai Tibetan Plateau, the Antarctic and high mountainous regions (Figure 1.1). In total, permafrost underlies 24% of the exposed Northern Hemisphere surface area (Obu, 2021; Dobinski, 2011). Permafrost in combination with surface vegetation forms a delicately balanced ecosystem. The permafrost ecosystem includes distinct landscapes with unique vegetation types that thrive under harsh cold climate conditions. These landscapes vary from dry barren soils, to vegetation rich landscapes with an abundance of water (Van Huissteden, 2020). Seasonal freezing and thawing cycles impact these landscapes differently due to the large variety in composition of the various landscapes.

The frozen nature of permafrost restricts many environmental cycles and processes from taking place. While during summer thaw the upper layer of the permafrost thaws, also known as the active layer, the majority of the underlying permafrost remains frozen (Van Everdingen et al., 1998). This limits the movement of, for example, groundwater, since infiltration and percolation of rain water and snow melt into the groundwater are blocked by frozen pores. Similarly, deep groundwater flow is also limited, preventing the formation of an active groundwater system. Consequently, the absence of an active groundwater system restricts groundwater solute transport of dissolved solids and trapped gasses to the surface and atmosphere. Likewise, bacterial decomposition processes in the subsurface are highly reduced at sub 0°C temperatures (Graham et al., 2012).

However, permafrost is threatened by global warming due to increasingly higher air temperatures. This causes the permafrost to thaw at increasingly higher rates and to

increasingly greater depths. Consequently, the permafrost regions will start to adapt to the changing conditions, reactivating environmental cycles. Rainwater will start to infiltrate into the thawed topsoil, groundwater flowpaths will start to develop and bacterial activity will intensify. As a result of the changing environmental conditions, the permafrost landscape will evolve and become more dynamic, until a new stable state is reached (Bruhwiler et al., 2021). The question is however, what does the new permafrost environment look like, how do the dynamics change, and are there any unforeseen feedbacks? In order to predict how the permafrost might evolve over the coming decades, it is important to understand the origin and buildup of permafrost, as it is key in understanding the processes and feedbacks of permafrost thaw.

1.1.2 | The formation of permafrost

Before the last ice age, the arctic regions were covered with a large variety of lush vegetation and thick peat bogs, capturing vast quantities of carbon from the atmosphere and fixating it in the organic material, acting as a carbon sink (Väliranta et al., 2021). In the water-rich bog areas, the anaerobe conditions limited bacterial decomposition of the organic material and the associated bacterial respiration (Schuur et al., 2008).

During the last ice age, annual air temperatures dropped to far below 0°C, thereby freezing the landscape. The Northern Hemisphere remained for large parts unglaciated (Lindgren et al., 2016). This allowed the soils to freeze up to great depths, in some areas exceeding over 1000 meters in depth from the surface (Strauss et al., 2017). As a result, the soil, bacteria, and stored carbon were frozen in a solid and inactive state.

Depending on the landscape, permafrost can exist in a wide variety of materials, from fine to coarse sands, silt, clay and gravel containing varying organic matter contents (Hugelius et al., 2013). A special category of permafrost is the so-called "Yedoma" permafrost. Current yedoma permafrost has formed during and after the last ice-age and is characterised by a mixture of ice-rich fine grained sand, with a high content of fossil plant material and animal remains (Zimov et al., 2006; Schuur et al., 2008). Yedoma permafrost in Siberia is estimated to contain one-third of the total organic carbon on Earth (Figure 1.2) (Altshuler et al., 2017; Vonk et al., 2013b). These Yedoma permafrost deposits are extra vulnerable to climate warming due to the high ice-content, where thaw triggers landscape deformation, turning it into a carbon source due to the large amounts of legacy carbon that is sequestered within the material (Vonk et al., 2013b; Miner et al., 2022; Bockheim & Hinkel, 2007; Schuur et al., 2008).

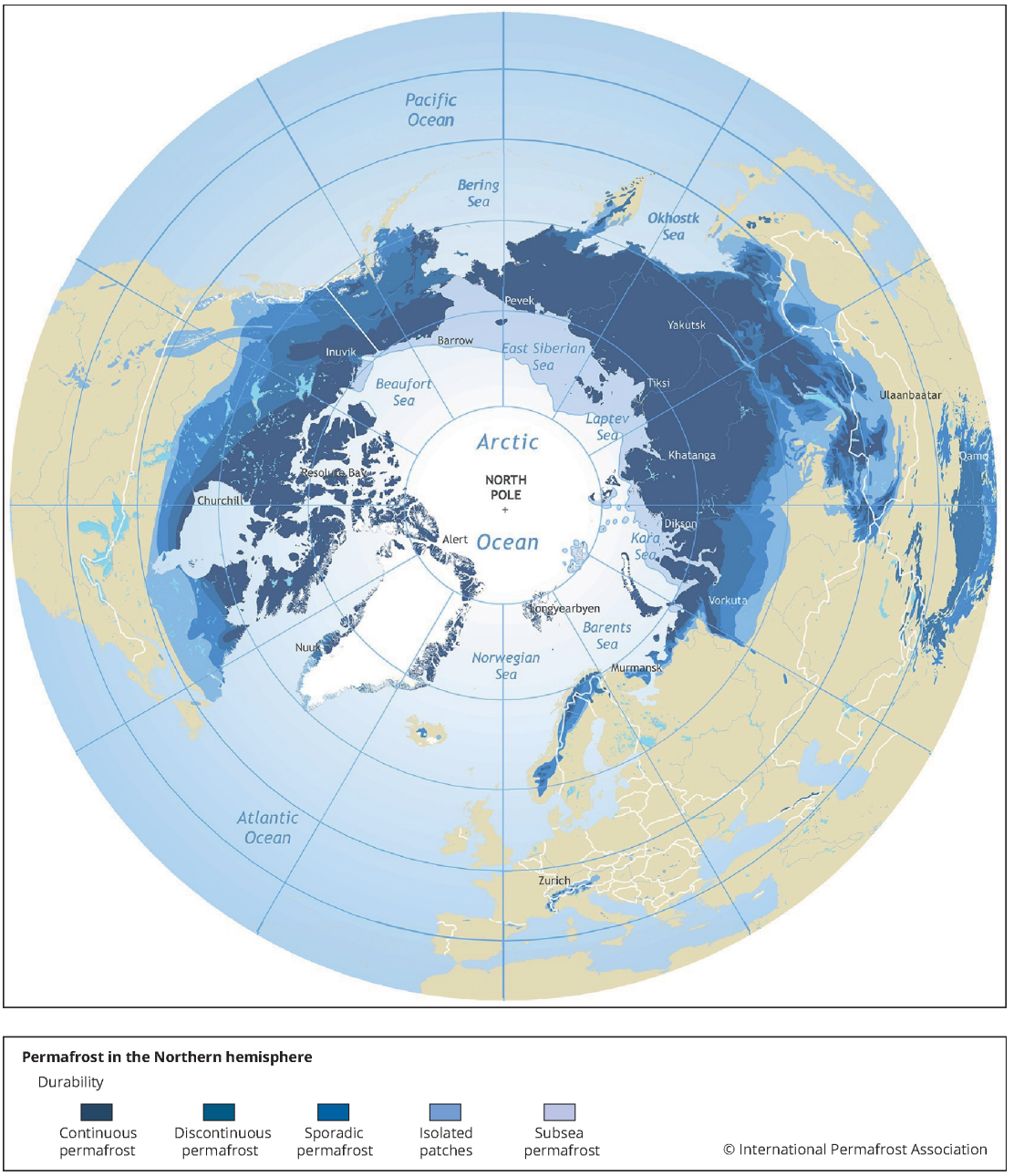

Figure 1.1 | Map of the distribution of various types of permafrost across the Northern Hemisphere (Brown et al., 1997).

1.1.3 | Arctic global warming

Since the late 1900's, the global air temperatures are rising at an accelerating rate due to anthropogenic emissions leading to warming (IPCC, 2021). Global annual air temperatures have risen with 0.12–0.15°C per decade since 1980 (Nita et al., 2022). This global warming effect is amplified towards the poles due to an effect called 'Arctic Amplification', increasing annual air temperatures over three times faster com-

pared to the global average in the polar regions (Shijin et al., 2023; Previdi et al., 2021; Rantanen et al., 2022). The increase in air temperatures over the arctic regions prompts anthropogenic induced permafrost thaw (Biskaborn et al., 2019), which contributes to a significant reduction in permafrost thickness (Box et al., 2019). This thaw goes beyond seasonal freeze-thaw cycles, as it involves a more permanent thaw where the permafrost will disappear completely in certain regions. Currently, permafrost temperatures are between −5 and 0°C, the interval where permafrost freezing and thawing take place for more than a quarter of the year (Overduin et al., 2006). Permafrost is clearly undergoing a transition in dynamics, raising the question of what will be the potential consequences for the Arctic region and globally of the changing permafrost dynamics.

1.1.4 | The changing role of permafrost

Permafrost thaw and subsequent degradation is a multi-scale process, including large scale deepening of the seasonal active layer, but also localised rapid degradation, in the form of deep thaw features such as thaw slumps (Strauss et al., 2017). The impact of permafrost thaw extends beyond the Arctic and subarctic regions, as it affects the biodiversity in a larger region, the water and the global carbon cycles (Schaefer et al., 2014).

It may sound counter-intuitive at first to describe the role of the water cycles in frozen permafrost areas. Yet, as is the case for all soils around the world, permafrost contains a vast amount of fresh water indeed, 69% of the global surface fresh water is trapped within ground ice and permafrost (Gleick et al., 1993). Permafrost thereby acts as a buffer area for groundwater. During various stages of permafrost thaw, groundwater fluxes could start to evolve, despite the normally frozen state of the material. This groundwater typically discharges in streams and rivers. The varying influx of groundwater in combination with summer snow melt leads to seasonal variation in stream discharge between summer and winter (Ye et al., 2009). As permafrost thaw increases, new groundwater pathways will likely start to emerge, leading to a more developed, and over time continuous groundwater system with more groundwater discharge (Song et al., 2020; Bense et al., 2009; Walvoord & Kurylyk, 2016). The change in the hydrological functioning of a system leads to large uncertainties when modelling future water fluxes (Sjöberg et al., 2021). As an example, the Qinghai Tibetan Plateau (QTP) is overlain by a vast permafrost area that has an evolving groundwater system. It is the source area of a number of large-scale basins and is therefore known as the "water tower" of Asia, supplying the Yellow river, Yangtze river and Mekong river with water (Zhang et al., 2022). Changing groundwater dynamics at the QTP will change the annual and long-term discharge dynamics of these rivers, thereby

affecting highly populated areas downstream (Wang et al., 2023).

Similar to the water cycle, permafrost and the global carbon cycle are intertwined. As permafrost degrades and thaws, previously frozen organic material becomes mobile. Once mobile, the organic material can be directly decomposed when under aerobic conditions, or it can be transported with groundwater. As the organic material comes into contact with bacteria, the organic material will degrade and through respiration will be released as the greenhouse gasses carbon dioxide (CO_2) and methane (CH_4) into the atmosphere (Schuur et al., 2008; Zimov et al., 2006; Schaphoff et al., 2013). Alternatively, organic material has the ability to dissolve into the groundwater as Dissolved Organic Carbon (DOC), allowing it to be transported via ground and surface water (Ma et al., 2019; Wild et al., 2019). Deep emerging groundwater flows, triggered by permafrost degradation, form a pathway for DOC stored within deeper layers of permafrost to be transported to the surface. Previously immobile organic carbon could thereby become part of the global carbon cycle (Walvoord & Striegl, 2007; Dutta et al., 2006). It is feared that the vast stores of organic carbon, trapped within the Yedoma permafrost, will act as a large greenhouse gas emitter as permafrost thaws (Vonk et al., 2013a). There remain, however, many uncertainties, since there is hardly any data on the occurrence and magnitude of this phenomenon. The release of CO_2 and CH_4 from permafrost is a positive feedback cycle, where the increase in greenhouse gasses leads to higher air temperatures, which in turn leads to a further deepening of the active layer and acceleration of the process (Schaefer et al., 2014). On the other hand, vegetation growth will increase as permafrost thaws, thereby increasing the carbon sequestration capability of the area. There are still large uncertainties on the magnitude of both processes, leaving questions if the permafrost environment will eventually turn out to be a sink or a source of organic carbon (Turetsky et al., 2020; McGuire et al., 2018). It is estimated that the permafrost regions contain roughly 1672 Pg of organic carbon, which accounts for roughly 50% of the reported global subsurface carbon (Figure 1.2) (Tarnocai et al., 2009).

1.1.5 | Societal impact of permafrost thaw

Although permafrost thaw occurs in the polar regions in mostly sparsely populated areas, the implications stretch over multiple scales both spatially and temporally, affecting not only the local environment, but also on a regional and global scale. Locally, community infrastructure is typically built on top of the permafrost, which provided a stable foundation for many centuries. Yet, the deepening of the active layer causes a degradation of infrastructure foundations. Roads, buildings and pipelines are destabilised as the ground shifts, leading to structural damages and an increase in maintenance costs (Melnikov et al., 2022). Regionally, permafrost thaw and asso-

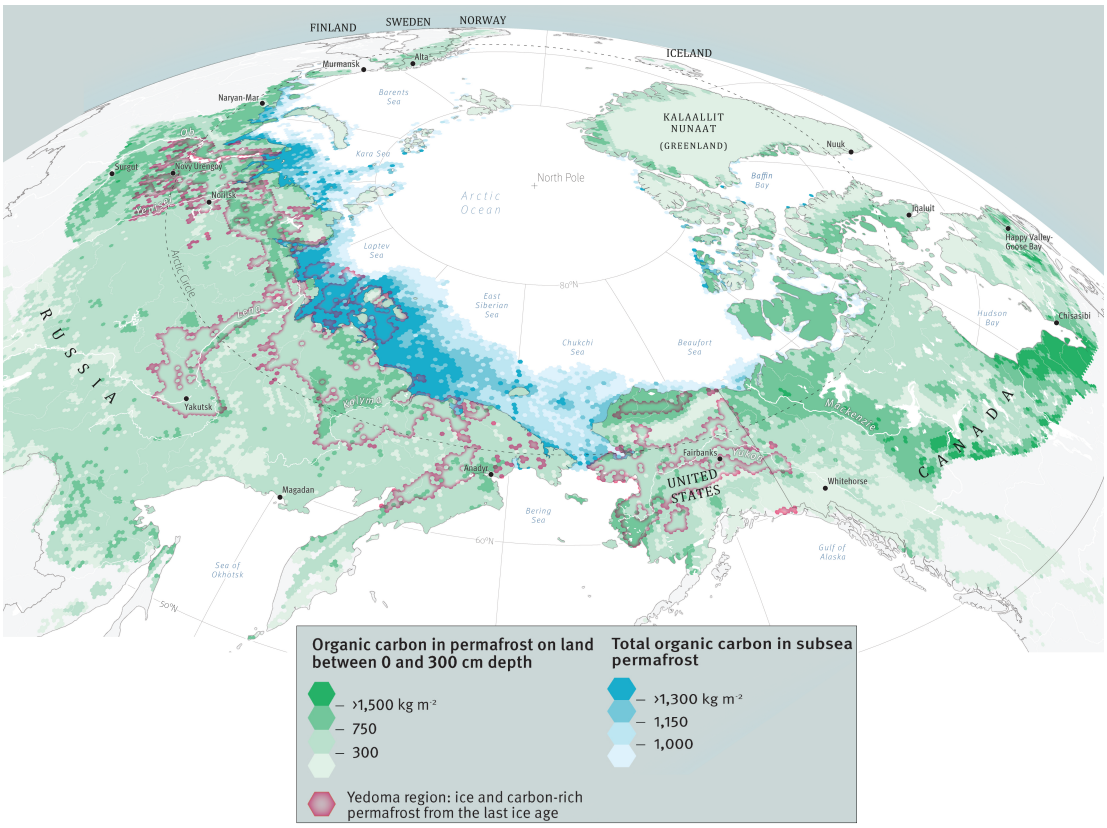

Figure 1.2 | Distribution and quantity of organic carbon in the top 3 m of terrestrial permafrost and organic carbon in subsea permafrost summed over the sediment accumulated over the last 450 kyr. Adjusted from (Westerveld, 2023) based upon (Hugelius et al., 2013; Strauss et al., 2017; Miesner et al., 2023).

ciated shifts in river discharge regimes affects the socio-economic functioning of a river system. Economic activities that rely on certain discharge regimes, including for hydro power, all rely on predictable discharges. Yet, the changing permafrost dynamics result in more uncertainty, making discharge predictions significantly more challenging. On a global scale, the additional release of greenhouse gasses creates a feedback loop, further accelerating global warming. The subsequent increase in global air temperatures accelerates the thaw of land-ice, contributing to global sea level rise.

1.2 | The dynamic behaviour of permafrost

Despite the frozen nature of permafrost, internal freeze and thaw processes are ongoing. Even if permafrost is at below 0°C temperatures for a significant time, part of the porewater might be in a liquid state due to a delay in the freezing process (Tian et al., 2014). Similarly during summer with above 0°C temperatures, permafrost can

undergo both slow thawing of the active layer, but certain areas are susceptible to a rapid localised thaw event in the form of a thawslump (Turetsky et al., 2020). Permafrost is therefore more dynamic than one would assume at first glance.

The dynamical behaviour of permafrost depends on many factors, including amongst others; surface characteristics, the type of permafrost, geographical location, soil layering, material composition, and the thermal properties. For example, the permafrost surface characteristics define the interface between the air and the soil, where intricate dynamics occur that govern the transfer of heat into the permafrost. Vegetation, precipitation and snow cover control the transfer of heat into the permafrost (Heijmans et al., 2022). In order to make predictions on internal permafrost dynamics we need a thorough understanding of the composition of, and physical processes that occur within permafrost.

1.2.1 | Permafrost fundamentals

Permafrost can be distributed in various horizontal and vertical extents (Figure 1.3). Depending on the spatial coverage, permafrost can be isolated in patches, where $0 - 10\%$ of an area is underlain by permafrost. Here the permafrost can have a vertical extent of only a meter. This type of permafrost is typically located in the boreal regions. Then there is sporadic permafrost, consisting of patches where $10 - 50\%$ of the land surface is underlain by permafrost. On the other end of the spectrum, continuous permafrost covers $90 - 100\%$ of the land surface and has a deep vertical extent ranging up to hundreds of meters (Van Everdingen et al., 1998). This type of permafrost is typically located in the Arctic regions close to the poles. Permafrost thereby crosses multiple scales both in spatial coverage and vertical extent (Figure 1.1). Depending on the type of permafrost, it has a varying sensitivity to climate warming, where thick permafrost is less sensitive compared to thin sporadic permafrost.

Permafrost is typically built-up out of a number of distinctive layers. The top layer of the soil is referred to as the active layer (Figure 1.4). The active layer can be covered with arctic vegetation, but depending on the region, the surface could be barren as well. This layers, as the name suggests, is most active as it seasonally freezes and thaws. During winter, air temperatures are usually well below 0°C. At this stage, the active layer is fully frozen all the way from the top to the base of the permafrost. During summer, air temperatures can exceed 0°C, causing the active layer to develop from the top vertically downwards. Depending on the duration of the thaw period, maximum air temperature and soil properties, the active layer thaws up to a certain depth. The thickness of the active layer typically ranges between 0.5 to 2 meters and varies per region.

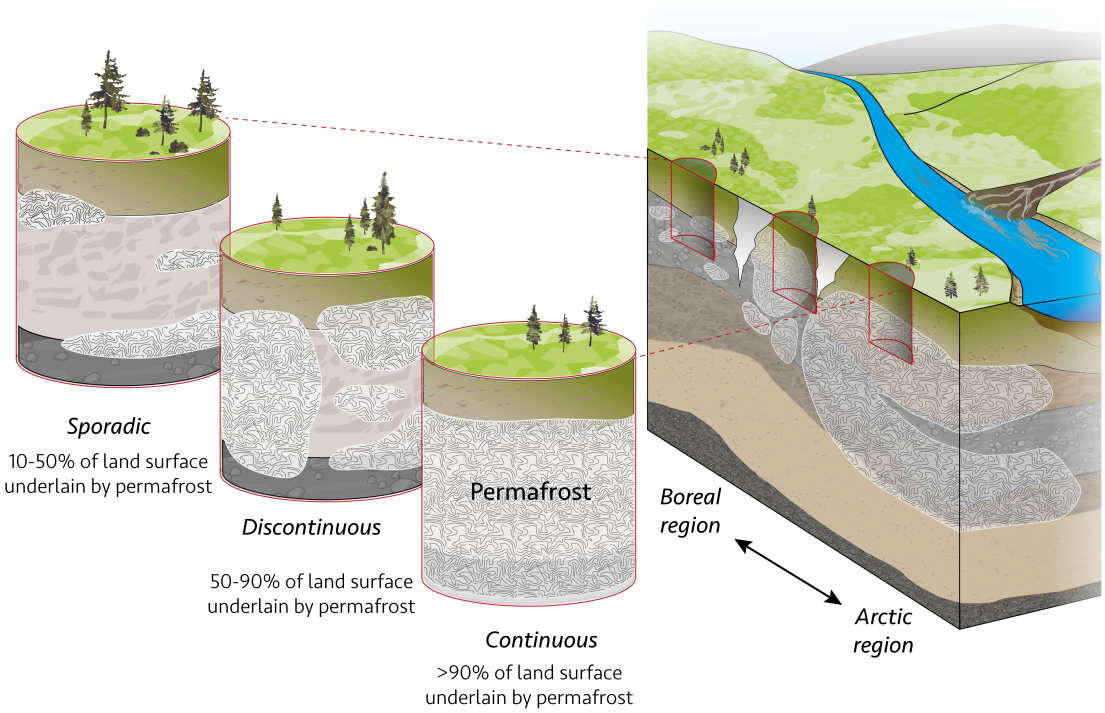

Figure 1.3 | Classification of the various types of permafrost based upon percentage of permafrost underlying a certain area.

With increasingly higher air temperatures for prolonged periods of time, active layer thaw can exceed normal thawing depths. If a mild winter occurs, the entire active layer will not re-freeze, and a zone of thawed material remains embedded in between the permafrost and base of the active layer. This is referred to as a supra-permafrost talik or perennial thaw zone (Figure 1.5). Supra-permafrost taliks can exist one season and refreeze, but they can also grow over multiple seasons. Over time, these supra-permafrost taliks can start to act as conduits for local groundwater flow (Walvoord & Kurylyk, 2016; Bense et al., 2012).

A talik is a layer of unfrozen ground within a permafrost system that exists for more than one year (Van Everdingen et al., 1998). Taliks can develop through multiple processes. In essence, local surface characteristics cause a temperature anomaly at the surface where underlying temperatures slowly increase. This could be, for example, a small stream discharging water, or a small lake forming over summer in a depression in the landscape which can grow over time. Due to the change in surface characteristics, the active layer reacts and refreezes differently, as for example, a small developing pond at the surface can create a time-lag in the freezing and thawing process of the underlying permafrost. Taliks have the ability to connect multiple unfrozen layers, known as through taliks, creating an interconnected groundwater system. This ac-

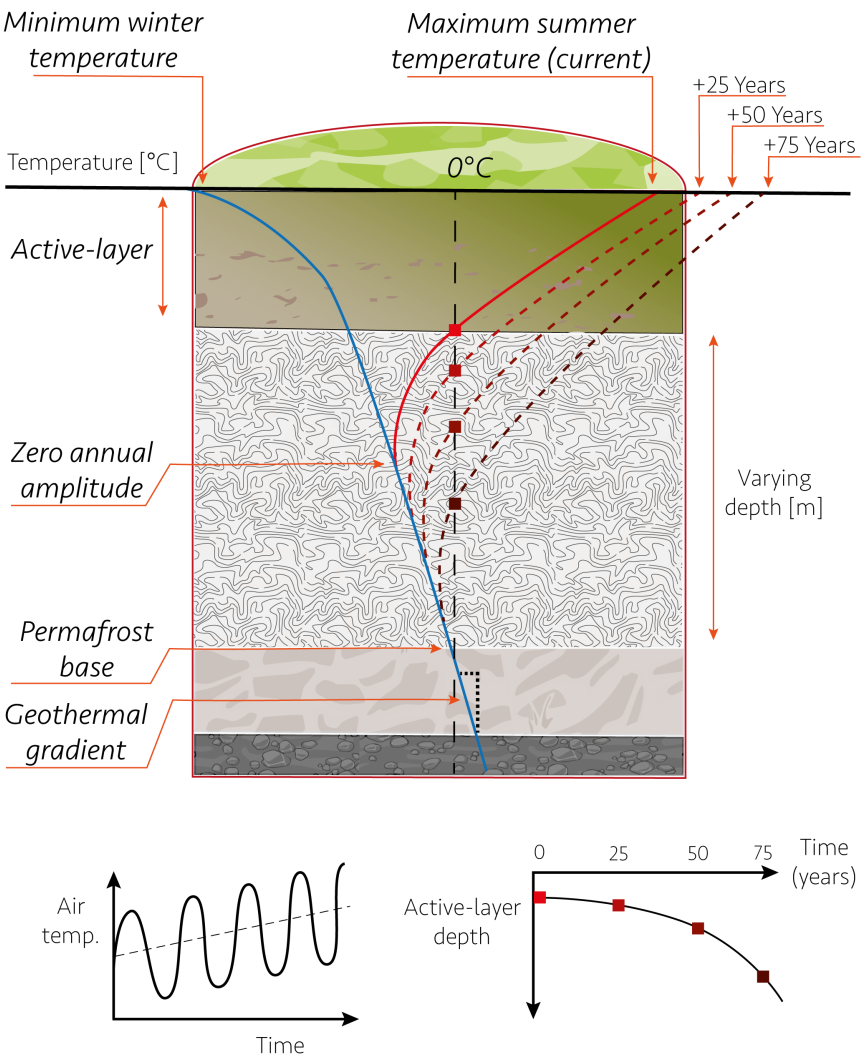

Figure 1.4 | Seasonal variations in active-layer temperatures over depth. Active layer depth increases under higher maximum summer temperatures.

commodates the transport of dissolved solids like Dissolved Organic Carbon (DOC) from deep permafrost layers, facilitating the discharge of groundwater to the surface hydrological system (Walvoord et al., 2019; Jafarov et al., 2018; Cochand et al., 2019; Frampton et al., 2013; Wang et al., 2018b). As a result of thawing conditions, the occurrence of permafrost groundwater flow will increase over time.

1.2.2 | Permafrost and groundwater

In order to describe the intricacies of permafrost groundwater fluxes, we first need to zoom out and evaluate the water cycle from a broader perspective. Water is transported to a specific area in the form of water vapour within the clouds. At a certain stage the water vapour condenses and falls to the Earth's surface as precipitation,

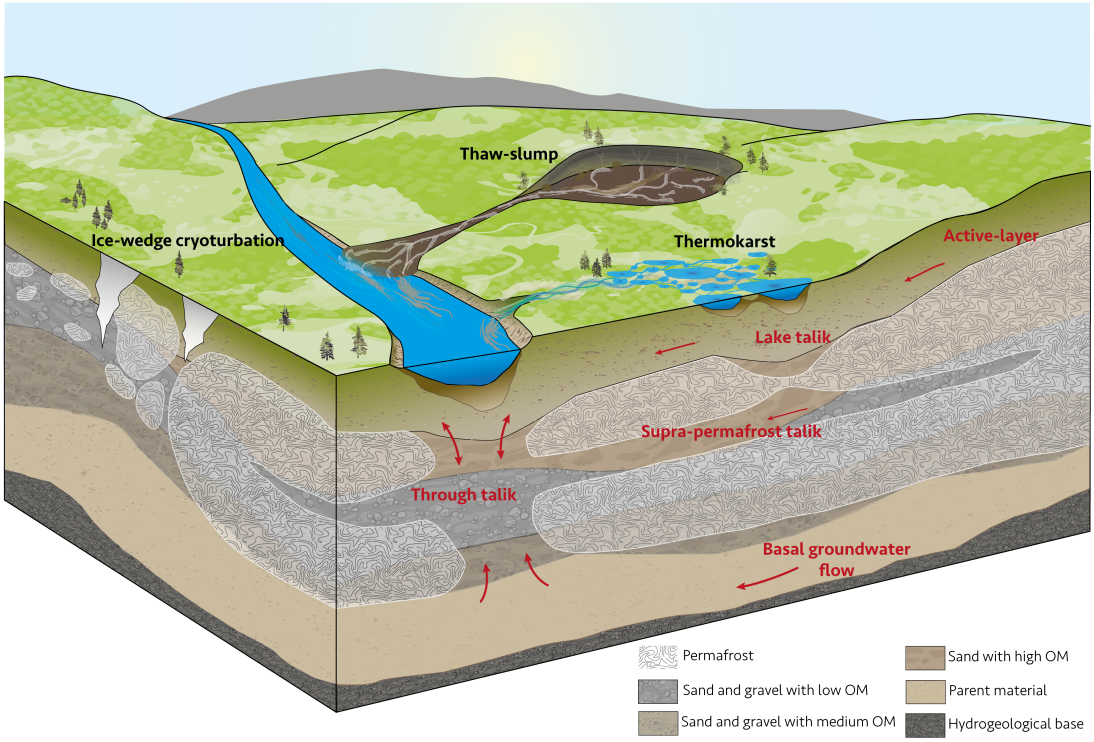

Figure 1.5 | Cross-section showing key permafrost processes occurring under a warming climate, impacting the hydrogeological functioning of the area. Arrows indicate possible groundwater flow routes.

which could be in the from of rain or snow in cold climates. As the water reaches the Earth's surface, it will partially percolate into the soil pores, and run off as surface water. As water percolates into the pores, it is referred to as porewater. The porewater slowly fills the available porespace, where the fraction of water filled pores to total porespace is known as the saturation level. Not all pores in the top layer will be filled with water, it is therefore known as the unsaturated zone. Most of the porewater will continue to percolate downwards until it reaches the water table. Groundwater flow occurs when there is a hydraulic gradient. This creates a pressure difference that forces the water to flow from high hydraulic head to the lowest hydraulic head. Each soil type has varying characteristics that determine how well groundwater can flow through the pore space, this is known as the hydraulic conductivity. Based upon the difference in hydraulic head, in combination with the hydraulic conductivity, we can calculate the groundwater flow using Darcy's Law.

The water table marks the top of the fully saturated layer, known as an aquifer. Aquifers have the ability to allow for easy transport of groundwater through porous material, such as a coarse sand. There are also soil types that act as a barrier for groundwater flow due to a lack of pore space or buildup of the material, these are

for example clay soil. Layers that act as a barrier for groundwater flows are known as aquitards. In the case of permafrost hydrogeology, a fully frozen soil layer also forms an impenetrable layer for groundwater. Frozen porewater blocks the pore matrix, thereby acting as a barrier for groundwater flow. Whereas clay remains impenetrable due to its physical properties, a frozen permafrost layer might thaw during summer. Then instead of forming a barrier, it could form an open corridor for groundwater flow to occur in the form of a talik. Once taliks have formed, it might lead to an increase in groundwater activity that contributes to further permafrost degradation (Frampton et al., 2013). Permafrost systems can therefore be part of a complex evolving groundwater flow system, comprising of perennial thaw zones and through taliks that allow deep groundwater to flow to the surface and discharge to permafrost streams.

1.2.2.1 | Solute transport

Permafrost groundwater flow can occur in the active layer or perennial thaw zones, but also at the base of the permafrost, from where it can seep towards the surface. The emergence of deep groundwater seepage does not only impact the water cycle, but it also impacts the carbon cycle. This is due to the ability of groundwater to transport dissolved solutes from various permafrost layers to the surface (Cochand et al., 2019). Vast stores of organic carbon in the Yedoma deposits, for example, can dissolve into the groundwater (Vonk et al., 2013a). The transport of Dissolved Organic Carbon (DOC) is of special interest. Once it reaches the surface, bacterial decomposition transforms the DOC into the greenhouse gasses CO_2 and CH_4. There are also concerns about the impact of increasing DOC transport to the surface and the subsequent release into the atmosphere of more greenhouse gasses. However, the effectiveness of the transport and release of DOC as greenhouse gasses is currently one of the important unknowns in permafrost studies (Diak et al., 2023; Mohammed et al., 2022).

1.3 | Permafrost heat transfer processes

Permafrost freezing and thawing occurs on a large scale, however the actual heat transfer process takes place on a very small scale. In order to physically describe permafrost freezing and thawing, we need to evaluate heat transfer processes that are involved.

There are four main categories of heat transfer mechanisms; conductive, advective, convective and radiative heat flow. The two primary heat transport mechanisms within permafrost are conductive and advective heat transport. Conductive heat flow

is the transfer of energy between objects in physical contact via molecular vibration and collision. Advective heat flow is the transfer of energy that is transported using a carrier fluid flowing from one position to another. Considering the latter two, convective heat flow is a process that relies on density driven fluid transport and radiative heat flow that relies on the transfer of heat via radiation. These are not relevant mechanisms for heat transport within permafrost.

The primary heat transport mechanism for frozen permafrost is conductive heat flow, since this process takes place despite the frozen nature of the material. Yet, as permafrost thaws, groundwater becomes mobile, which activates a secondary heat transport process, namely advective heat transport. Advective heat transport can exceed conductive heat transport, depending on the groundwater flow rate and temperature gradient. Research has shown that, for example, through taliks could form conduits for conduction-advection heat transport in permafrost areas, accelerating degradation (Scheidegger & Bense, 2014).

Central to heat transport mechanisms is the law of conservation of energy. There is always a balance between energy entering or leaving the system and energy that is stored within the system. Using the principles for conductive advective heat transfer and the energy balance, we can understand how, for example, surface temperature variations propagate downward into the permafrost active layer and warm up or cool down the subsurface.

The freezing and thawing of permafrost is simulated using numerical heat transport models, relying on physical equations describing conductive and advective heat transport and the law for the conservation of energy (Lunardini, 1985; Grenier et al., 2018). All of the processes involved in permafrost freezing and thawing need to be accurately described mathematically, and parameterised. The essential parameters controlling heat transport rates are the thermal properties of the permafrost.

1.3.1 | Permafrost thermal properties

The ability of a material to conduct and store heat is determined by the thermal properties. Thermal conductivity is the ability of a material to conduct heat, related to conductive heat flow. A low thermal conductivity indicates that a material conducts heat poorly, while a high conductivity indicates that a material conducts heat very well. The heat capacity of a material describes how much energy needs to be supplied to a unit to increase the temperature by a certain amount. Each material has a specific thermal conductivity and heat capacity.

Permafrost comprises a mixture of materials, including grains, porewater, and organic

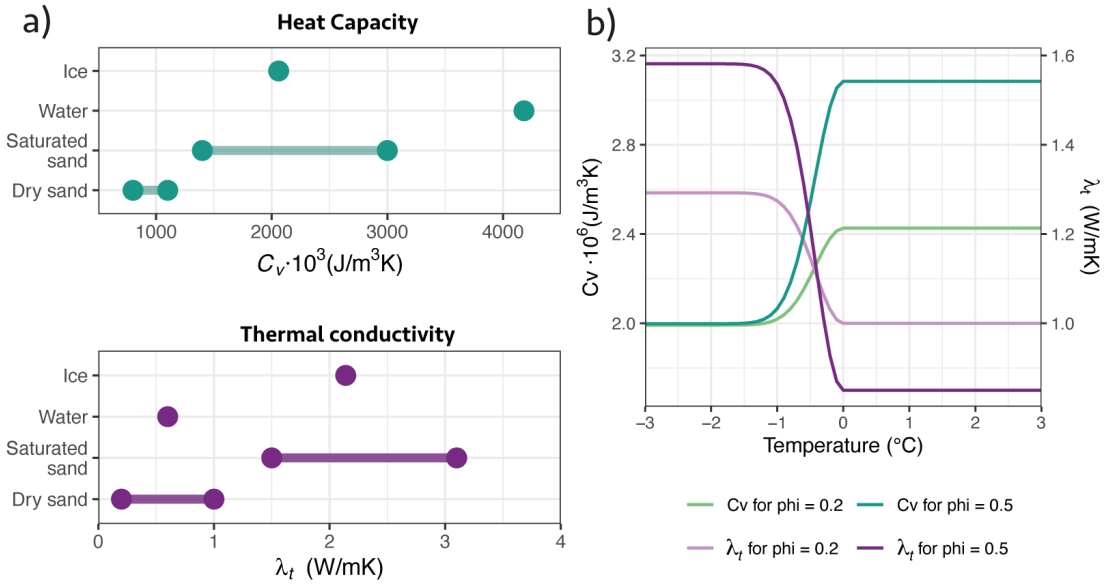

Figure 1.6 | a) Typical ranges of volumetric heat capacity (C) (Abu-Hamdeh, 2003) and thermal conductivity of soils for various saturation levels and of fresh water (λ) (Smits et al., 2010; Abu-Hamdeh & Reeder, 2000; Midttømme & Roaldset, 1998). b) Variation in bulk thermal conductivity (λ_t) and bulk heat capacity (C_v) as a function of temperature over the freezing-thawing interval for various porosity's.

matter (OM), each having unique thermal properties that vary over a specific range (Figure 1.6a). Typically, the thermal conductivity and heat capacity are effectively combined based upon the fraction into a single value for the thermal conductivity and heat capacity. These are referred to as the bulk thermal properties. The range of the bulk thermal properties can vary significantly depending on the variations in soil properties. For example OM has a lower thermal conductivity compared to sand, so a high OM content lowers the overall bulk thermal conductivity, acting as an insulator. The thermal properties of the permafrost soil materials remain stable over time, however the thermal properties of porewater vary as a result of seasonal freezing and thawing. This is due to the phase change of the porewater, during which it changes between a solid and a liquid. The phase change alters the physical structure of the material, thereby changing the thermal properties as well. A nice example can be seen in Figure 1.6b, that shows how bulk thermal conductivity and heat capacity of a saturated soil vary over the freeze thaw interval for various porosity's. The change in thermal properties over the transitional zone between frozen and thawed is governed by the freezing and thawing of the porewater. It is very difficult to determine the thermal conductivity or heat capacity of the permafrost, without considering the porosity due to coupling with the porewater. It is clear that porewater plays a crucial role during permafrost freeze-thaw transitions, as it changes the bulk thermal properties and controls if advective heat transport is possible.

1.3.2 | Porewater phase change

At the heart of permafrost thaw dynamics lies the porewater freeze-thaw transition. The freeze-thaw interface marks the transitional zone between a stationary (frozen) and an active and dynamic (liquid) system (Figure 1.7a). The transition occurs around the 0°C temperature mark and influences a multitude of permafrost processes. As porewater thaws, the viscosity decreases, allowing easier flow through the porespace as groundwater compared to porewater with a high viscosity that is nearly frozen. At the same time, the thermal properties of the permafrost change as a result of the freeze-thaw transition.

Phase change is an energy driven process during which a material, in our case water, changes between a liquid and a solid or vice versa. The actual phase change requires energy that needs to be supplied or extracted. This energy is called the *latent heat of fusion*. The phase change transition is an isothermal process until the energy demand is met. During the phase change, the porewater is partially frozen and partially liquid, this is also known as the *mushy zone* (Figure 1.7b) (McKenzie et al., 2007).

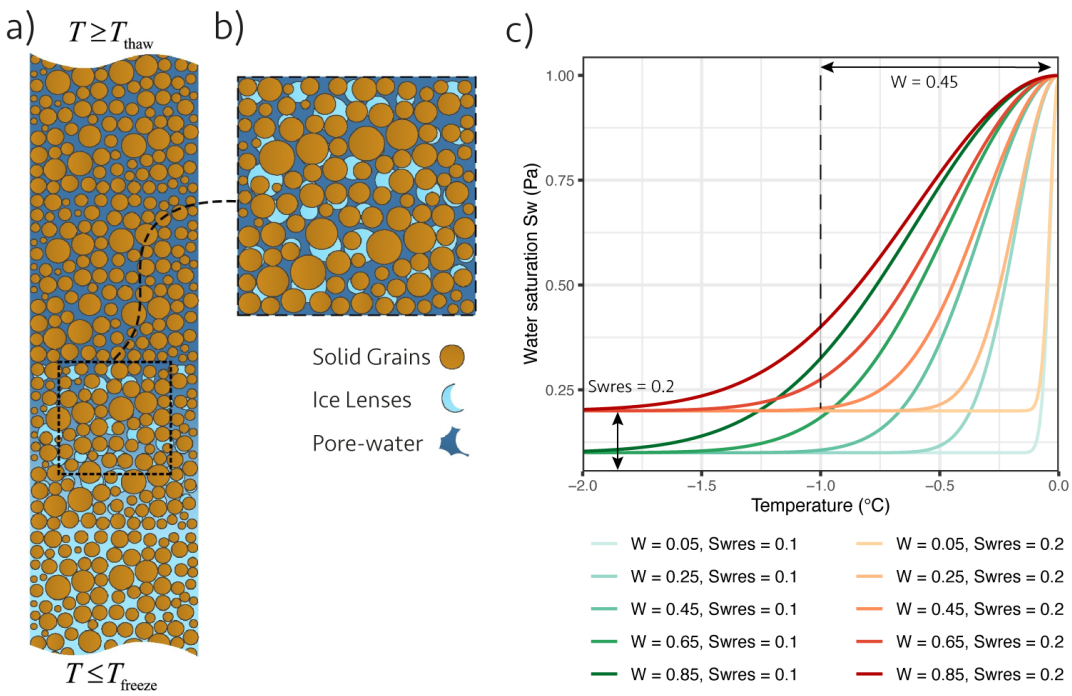

Figure 1.7 | Partly frozen soil mushy zone. a) Transitional mushy zone of partially frozen and thawed porewater, where T_{thaw} is the temperature at which soil freezes and T_{freeze} the temperature at which soil thaws. b) detailed figure of the mushy zone showing both liquid pore-water and ice lenses. c) Variations in SFCC for various parameter combinations, equation for SFCC can be found in Table 2.1. Adjusted from (Amiri et al., 2018).

The repeated freezing and thawing is not a symmetrical process, but it shows hyste-

resis. For a given amount of energy released during freezing, the liquid water content differs compared to the unfrozen water content for the same amount of energy transfer during thawing. This hysteresis is caused by two processes that occur only during freezing, these are metastable nucleation and supercooling (Zhang et al., 2020). Nucleation is the process during which liquid water clusters into crystal structures, the metastable zone is the period during freezing during which no appreciable nucleation occurs (Bhamidi et al., 2017). Supercooling is a phenomenon during which the temperature of a liquid is lowered to below the freezing point, without becoming a solid (Kozlowski, 2009). As soon as porewater nuclei crystals form, the temperature jumps to 0°C and the phase change commences. Hysteresis is observed during field conditions, but it remains very difficult to determine and to recreate the actual conditions that define the occurrence and intensity of the hysteresis.

The challenge is to incorporate freeze-thaw hysteresis into numerical modelling, despite the complexities of different soil types, saturation level, porewater salt concentration etc. Therefore, empirically derived curves are used to describe repeated freezing and thawing. One example used in this thesis is *Soil Freezing Characteristic Curves* (SFCC's). SFCC's describe the relation between temperature and liquid porewater fraction over the freezing-thawing interval for specific soils. Figure 1.7c shows a number of SFCC curves, which have various gradients, and residual unfrozen water contents that allow to simulate porewater freezing and thawing for various soil types. The SFCC thereby allows us to link the hydrology and thermodynamics together at the freeze-thaw interval (Devoie et al., 2022; Amiri et al., 2018).

1.4 | Current challenges in permafrost parameterisation

Accurate predictions on the timing of freeze-thaw events is essential, as it triggers many feedback cycles. The thermal properties are key in improving or numerical heat transport models, yet these thermal properties are dynamic over the freeze-thaw interval. Often, ranges for the thermal properties from literature are used in numerical models if no observations are available, yet the range in thermal properties is quite large for the various materials depending on the physical properties of the material (Figure 1.6a), resulting in large uncertainties in model predictions (Harp et al., 2016; Wang et al., 2018a; Ebel et al., 2019). It is further more challenging to independently determine the thermal properties due to the coupling between thermal conductivity, heat capacity and porosity. Therefore, to improve numerical heat transport models, we need to improve our understanding and capacity to determine the

thermal properties. Typically, temperature observations are available at monitoring sites. In this thesis we therefore discuss ways to delineate the thermal properties from available temperature field observations, and study how the thermal properties vary as a function of various soil properties in controlled column experiments.

Next to the efforts to improve the numerical parameterisation of field processes, this thesis also contributes to improve field observations. To observe temporal changes in the field, non-invasive geophysical observation methods can be used that do not require elaborate drilling for installation, as is the case with, for example, temperature sensors. Electrical Resistivity Tomography (ERT) is a geophysical observation method that utilises electricity and resistance measurements to observe the physical properties of different soil types (Binley & Slater, 2020). Additionally, it can also detect temporal changes such as meltwater infiltration, solute transport, saturation changes and detect the freeze-thaw front (Hilbich et al., 2011; French & Binley, 2004; Kneisel et al., 2014; Tomaškovičová & Ingeman-Nielsen, 2023). ERT measurements use a current that is injected into the soil, and at specific locations, the resistance between electrodes is measured. The resistance varies depending on the electrical conductive properties of the material, where for example a high saturation level helps to conduct electricity. These observations are processed using an inversion scheme, after which the resulting resistivity data can be related to specific soil properties.

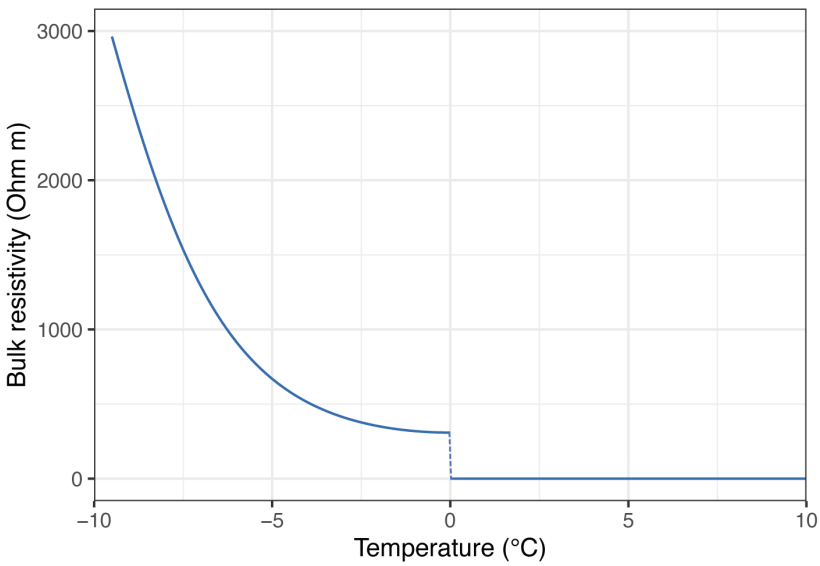

Figure 1.8 | Example of the theoretical relation between resistivity and temperature over the freeze-thaw interval, where the gradient varies for different soil types and water contents. Resistivity increases sharply at sub zero temperatures due to the initial freezing of the porewater. The theoretical temperature-resistivity relation is further elaborated in Chapter 4. Adjusted from Herring et al. (2021).

The ease of installation and sensitivity to temporal changes makes ERT ideal to be

used to monitor permafrost active layer dynamics (Herring et al., 2023). The disadvantage however is that ERT observations are influenced by temperature, where freezing and thawing of porewater affects the conductive properties, which prevents determining if resistivity changes are the result of, for example, surface infiltration or by temperature variations (Herring et al., 2019; Lyu et al., 2019). Figure 1.8 shows the theoretical relation between resistivity and temperature, where resistivity increases sharply for sub 0°C temperatures (Herring et al., 2021). This relation depends on the soil type and porewater saturation. One the one hand we can utilise the sensitivity of ERT to temperature to track the freeze-thaw front. Yet on the other hand, it would be very useful if we could remove the temperature effect to only observe subsurface geophysical changes. One way to study the relation between temperature and resistivity is by using a controlled experimental setup, such as a column experiment.

1.5 | Thesis outline

Summarising, the rate of permafrost thaw is uncertain due to global warming, resulting in an increase in thaw depth. This affects amongst others the global water and carbon cycles. Furthermore, infrastructure becomes more vulnerable as a result of the unstable surface due to thaw. Since many processes and feedbacks are a reaction to changing permafrost dynamics, it is essential that the heat propagation at the freeze-thaw interval is well understood. Any uncertainties regarding permafrost freezing and thawing will only project into larger uncertainties in consecutive reactive processes. Due to the many implications of permafrost thaw, this thesis looks at the current capabilities to simulate permafrost dynamics with a specific focus on freeze-thaw interactions, as this marks the moment that groundwater could start to flow.

The overall aim is to improve the parameterisation of current numerical models to simulate freeze-thaw dynamics, in order to increase the accuracy, and secondly to expand the observational capabilities to study permafrost dynamics in the field and lab. Three objectives have therefore been defined.

1.5.1 | Objectives and research questions

The objectives of this thesis are to:

- quantify the uncertainties of the thermal properties in current heat transport models.

- determine the effect of various soil properties on the thermal properties and subsequent propagation of heat.
- contribute to detecting the freeze-thaw front in lab experiments and reducing the uncertainty of the observation.

These objectives are translated into three specific research questions:

1. How well is a numerical 1D heat transport model capable of simulating real-world permafrost freeze-thaw observations with highly uncertain thermal properties?
2. Can numerical heat transport models be used to infer soil thermal properties of various soil types from lab experiments?
3. Can permafrost field resistivity observations be corrected for sub zero temperature variations?

The main data sources used in this study are data gathered using numerical heat transport model simulations, experimental data collected using laboratory column experiments and data from a field site at the QTP. The column experiments allow to meticulously observe the freeze-thaw transitions under various controlled conditions, varying soil properties and air temperatures. Furthermore, it enables simulating multiple freeze-thaw transitions over short periods of time, a process that would take a year to observe in the field. Numerical heat transport models are therefore a useful tool that allow us to simulate permafrost freeze-thaw dynamics under various conditions, controlling both the thermal properties as well as the porosity. This allowed us to explore a large variety of scenarios, to study, for example, warming scenarios and the effects on active layer thaw and groundwater flow development. Furthermore, many numerical simulations could be run in a short time period. The prerequisite however is that all processes must be accurately represented in the numerical models, and that the parameter values represent field conditions.

1.5.2 | Thesis chapters

In the three main research chapters, this thesis discusses and answers the three main research questions.

The first research question is addressed in **Chapter 2**. Utilising a temperature dataset collected at the Qinghai-Tibetan Plateau (QTP) comprising of 5 years of temperature observations collected at various depths in the permafrost (Luo et al., 2018b).

Making use of an existing 1D numerical heat transport model, multiyear permafrost temperatures of the QTP were simulated at various depths. We varied the thermal properties and porosity over a large parameter space, and determined the parameter combination that best simulated the observations. I demonstrate how a basic numerical model can be used in data scarce areas with limited knowledge of soil properties to determine the thermal properties and simulate multi-year permafrost dynamics.

Chapter 3 zooms in on the parameter estimation technique and evaluates a method to detect variations in thermal properties from various soil buildups. This experiments uses numerical heat transport models and data collected in laboratory column experiments. The heat transport model used in **Chapter 2** is applied here under controlled experimental conditions. Various soil properties are analysed and the associated thermal properties are determined using a fitting procedure and the heat transport model. By combining the knowledge from **Chapter 2** and **Chapter 3**, I answer research question two.

Untill this point in the thesis, temperature observations have been used to study temporal permafrost dynamics, yet temperature is not able to detect all processes involved with permafrost freezing and thawing. Especially during phase change, temperature is isothermal, yet porewater freezes or thaws. In **Chapter 4** I explore another method that could be used to detect temporal permafrost dynamics not detectable with temperature, namely using ERT observations. One of the main hypotheses is that resistivity observations could be a viable method to track the freeze and thaw front, if compensated for the increase in resistivity due to freezing. To test the hypothesis, I used the tried and tested column experimental setup as described in **Chapter 3**, and adjusted the setup to incorporate ERT timelapse observations. In **Chapter 4** I discuss how ERT observations are collected during the freezing and thawing of a column setup. This is subsequently used to analyse the development of resistivity during freezing and thawing, from which one can clearly detect the freeze and thaw front.

Finally, in **Chapter 5** I discuss the main findings of this thesis and answer the research questions. Furthermore, I reflect how this thesis contributes to the field of ongoing permafrost research and give a future outlook on opportunities for research to advance.

2

Determining thermal properties of permafrost from temperature observations

This chapter is based on:

de Bruin, J. G. H., Bense, V. F., van der Ploeg, M. J. (2021). Inferring Permafrost Active Layer Thermal Properties From Numerical Model Optimization, *Geophysical Research Letters*, 48, e2021GL093306, doi:10.1029/2021GL093306

Abstract

Permafrost has become increasingly unstable as a result of surface warming, therefore it is crucial to improve our understanding of permafrost spatiotemporal dynamics to assess the impact of active layer thickening on future hydrogeological processes. However, direct determinations of permafrost active-layer thermal properties are few, resulting in large uncertainty in forecasts of active layer thickness. To assess how to reduce the uncertainty without expanding monitoring efforts, a total of 1728 numerical 1D models were compared using three error measures against observed active layer temperature data from the Qinghai-Tibetan Plateau. Resulting optimised parameter values varied depending on the error measure used, but agree with reported ones: bulk volumetric heat capacity is 1.82-1.94 $\times 10^6 J/m^3$K, bulk thermal conductivity 1.0-1.2 W/mK and porosity 0.25-0.45 $(-)$. The active layer thickening rate varied significantly for the 3 error measures, as demonstrated by a $\sim$ 15 year thawing time-lag between the error measures over a 100 year modelling period.

2.1 | Introduction

Permafrost has become thermally unstable over the past few decades as a result of rising air temperatures (Vonk et al., 2015; Romanovsky et al., 2002; Biskaborn et al., 2019). The degradation of permafrost commences with an increasing thickness of the active layer towards the end of summer (Koven et al., 2015; Walvoord & Kurylyk, 2016; Schuur et al., 2008; Bense et al., 2012). A deepening of the active layer signals the onset of permafrost degradation, which has been widely observed using long-term observations of shallow (e.g. $< 10m$) temperature profiles (Åkerman & Johansson, 2008; Wu et al., 2015; Abramov et al., 2019; Luo et al., 2016). Increasing active layer thickness has a direct impact on many environmental processes including hydrology (Frey & McClelland, 2009; Bense et al., 2009; Kurylyk et al., 2016), water quality of aquatic ecosystems (Toohey et al., 2016) and results in fundamental landscape and vegetation change through thermokarst processes (Prowse et al., 2006; Bouchard et al., 2014; van der Kolk et al., 2016). Longer-term impacts at large spatial scales include the development of deeper groundwater flow pathways which can induce more vigorous groundwater solute transport (Bense et al., 2012; Frampton et al., 2013; Walvoord & Striegl, 2007; Walvoord et al., 2012), thereby changing regional hydrogeological systems.

The timescale on which environmental processes are affected by permafrost thaw is uncertain (Andresen et al., 2020). One of the most important rivers of China, the Yellow River, originates on the Qinghai-Tibet Plateau (QTP) (Cheng & Jin, 2013). Groundwater discharge originating from the thawing permafrost could undergo significant changes as the active layer increases in thickness (Song et al., 2020; Wang et al., 2018b; Sun et al., 2020a). The local population relies on a stable discharge because water is used for irrigation and for electricity production (Ding et al., 2017; Penghao et al., 2019). The timescale on which river discharge may change is therefore crucial in planning adaptation measures. Furthermore, active layer thickening is expected to lead to the mobilisation of organic carbon and other constituents such as Hg (Schuster et al., 2018; Turetsky et al., 2020; Schuur et al., 2009; O'Donnell et al., 2012), which can emerge from the thawing permafrost (Zimov et al., 2006; Vonk et al., 2019). Groundwater chemistry changes in turn affect microbial activity, which is responsible for organic matter decomposition and release of CO_2 and CH_4 into the atmosphere (Keller et al., 2010; Schuur et al., 2008; Mondav et al., 2017; Walz et al., 2017). The primary release mechanism of CO_2 and CH_4 from the active layer has been surface erosion and direct oxidation and release into the atmosphere (Dutta et al., 2006), yet with a deepening active layer, migration through groundwater will gain a more prominent role (Walvoord & Striegl, 2007). With over 818 Gt of organic carbon stored in the top 3 meters of the northern hemisphere active layer, a vast amount of CO_2 and CH_4

could potentially be released into the atmosphere (Dutta et al., 2006; Tarnocai et al., 2009; Schaefer et al., 2011; Wang et al., 2020). Additional release of CO_2 and CH_4 into the environment will affect current global warming predictions and may accelerate subsequent processes such as sea level rise. It is of vital importance to understand the timescale on which active layer thickening occurs and to better understand uncertainties in predictions of permafrost active layer thickness in the coming century.

Heat transfer models are used to simulate active layer freeze-thaw dynamics, and require thermal properties, including thermal conductivity λ and heat capacity C, to quantify heat transfer processes. In order to model active layer development over large areas, spatial data on subsurface thermal properties are required. Yet such data are scarce, requiring field sampling and laboratory analysis. Therefore, the subsurface thermal properties are often estimated using empirical relations with surface indicators such as soil texture, soil type and vegetation (Luo et al., 2014; Qin et al., 2017; Zhao et al., 2017). However, uncertainties are introduced when translating surface data of large areas into subsurface thermal properties because the relation between surface phenomena and subsurface thermal properties is not evident (Kitover et al., 2016; Zhao et al., 2017). Therefore, more accurate data on active layer thermal properties is required. Active layer properties λ and C can be accurately measured from field samples (Zhao et al., 2016). The thermal diffusivity, which is the ratio between λ and C can be determined using field temperature observations (Liu et al., 2019; Carson, 1963; Hinkel, 1997; Arias-Penas et al., 2015; Gao et al., 2017). For modelling purposes, individual λ and C values are often required, which depend on specific subsurface properties; e.g. parent material, organic matter content, air and (un)frozen soil moisture content Mustamo et al. (2019); Midttømme & Roaldset (1998). Reported bulk thermal conductivity (λ) of the subsurface ranges from 0.05 to 2.2 (W/mK) for active layers in Alaska, Siberia and the QTP (Brouchkov et al., 2005; Romanovsky & Osterkamp, 2000; Chen et al., 2020) and specific heat capacity (C) ranges between 580 and 690 (J/kgK) (Liu et al., 2018; Chen et al., 2020). Such data are not available for large parts of degrading permafrost areas. As a consequence, active layer thermal property variability - which is mostly unknown due to the active layer's composition and dynamic boundary condition behaviour - leads to a high degree of uncertainty when modelling active layer thawing depth and timing of thawing events (Schaefer et al., 2011).

In this study we demonstrate that permafrost temperature observations in combination with a numerical 1D heat transfer model can be used to evaluate thermal properties λ and C. We used the transient heat transfer equation (Kurylyk et al., 2014; Grenier et al., 2018) to model a batch of active-layer temperature time series. The 1D model is kept as generic as possible, and excludes stratification to demonstrate

that effective thermal property values can be obtained with very limited site-specific stratigraphic data. Thereafter, we used three types of error measurements: Root Mean Squared Error (*RMSE*), Kling-Gupta Efficiency (*KGE*) and *Russell's* error to find the best fitting models with associated thermal properties to match the temperature field observations. The resulting three optimal parameter combinations are subsequently used to model a 100 year future scenario, investigating the effect of the contrasting optimum parameter values on long-term predictions of active layer depth, thawing rate and the degradation of deeper permafrost.

The selection of a particular error measure is often determined by the error measure that is commonly used by the researcher in his/her field. However, careful consideration should be made regarding the type of data that is being used and the modelling objective (Jakeman et al., 2006). The choice for one specific error measure could create systematic bias, translating into an error that is omitted in the parameter sensitivity analysis. The *RMSE* and *KGE* error measures are common when evaluating models with observational data, where *RMSE* evaluates the residuals - the difference between observation and data - and *KGE* also takes the bias into account (Bennett et al., 2013). Since we are investigating the timescale of thawing events, we want to pay particular attention to the difference in timing (phase errors) as well. Therefore we also use the *Russell's* error, which combines a phase and magnitude error to evaluate time series that are subjected to a phase shift (Russell, 1997).

2.2 | Active layer thermal dynamics observed on the Qinghai-Tibet plateau

The QTP is an area subjected to ongoing permafrost research, where a relatively large quantity of temperature observations are being collected (Wu et al., 2010; Hu et al., 2019; Zou et al., 2017). We used field data from one site on the QTP (34° 15,3'N and 97° 51,2'E) as reported in Luo et al. (2018a,b). These consist of shallow temperature observations (at depths of 5 cm, 20 cm, down to 200 cm at a 20 cm interval) collected between November 2010 and December 2016, using a thermistor chain. The QTP is an elevated permafrost plateau region situated in China at an altitude between 4,600-4,750 meters above sea level. Mean long-term annual air temperature is -4.5°C and annual precipitation is about 460 mm, mainly occurring from May to September (Luo et al., 2018b). The mean permafrost temperatures on the QTP reach approximately -2.0°C (Cheng & Wu, 2007; Wu et al., 2010). Observations over the period 1980-2000 indicate that the mean permafrost temperatures increased by 0.2°C (Cheng & Wu, 2007; Wang et al., 2007; Jin et al., 2009). The permafrost in this area has been

degrading and decreasing in extent over the past decades, and continues to do so as a result of sensitivity to temperature increase (Wu & Zhang, 2008; Wu et al., 2010; Cheng & Jin, 2013; Luo et al., 2016; Ran et al., 2021). Regionally, the QTP contains a mixture of continuous, discontinuous and sporadic permafrost (Jin et al., 2009) and there is a strong variability in soil texture, soil moisture and peat occurrence (Li et al., 2016). The soil at the measurement location is composed of a poorly drained organic layer of 0.2-0.3 meters with a high moisture content. Beneath the organic layer, a peat layer extends 0.5 meters which is underlain by silty sands and coarse gravel (Luo et al., 2018a,b).

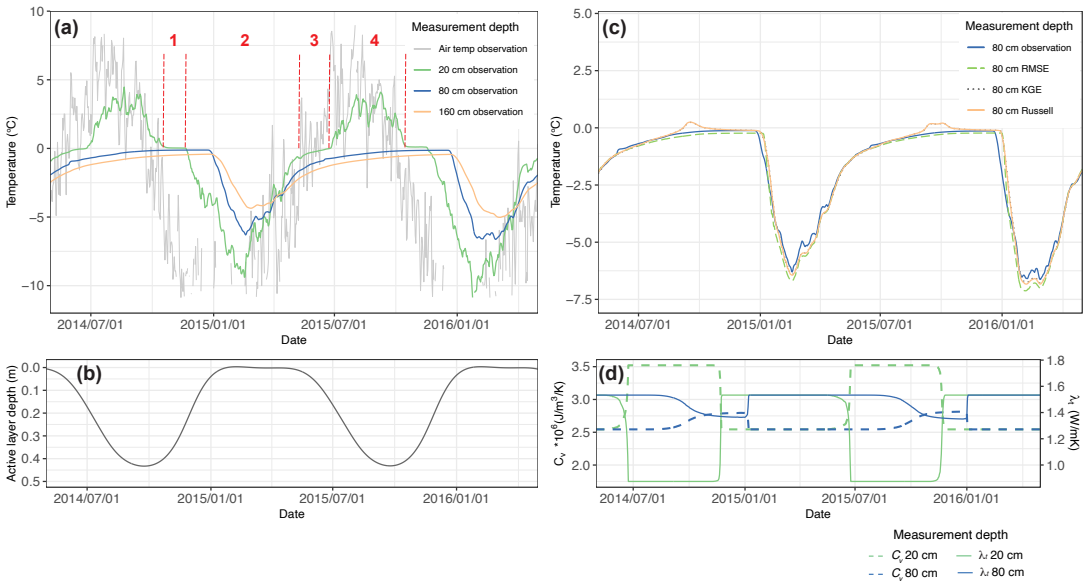

Figure 2.1 | Figure (a) shows a selection of the observed temperature data at the QTP with indications for characteristic freeze-thaw phases. Figure (b) active layer depth interpolated from the measured data set, Figure (c) comparison of observed and modelled temperature for the optimal parameter combinations of the error measures, Figure (d) modelled volumetric heat capacity and thermal conductivity.

The temperature data set includes continuous daily temperature observations. The data illustrate typical behaviour for freeze-thaw cycles where different stages can be distinguished (Figure 2.1a), namely, (1) the zero-curtain period in which pore water freezes, controlled by the release of latent heat (Putkonen, 1998; Romanovsky & Osterkamp, 2000), (2) Sub-zero temperatures, with stable thermal properties, (3) ice phase transition back to water, dynamic thermal properties, and (4) above 0°C ground temperatures, fast response to air temperature fluctuations. Figure 2.1b shows the maximum active layer depth where the temperature exceeds 0°C interpolated from the observed data.

2.3 | Methods

2.3.1 | Numerical modelling

In this study we implemented the conduction heat transfer equations (Sjöberg et al., 2016; Frampton et al., 2011; Nagare et al., 2015; Bense et al., 2009; McKenzie et al., 2007; Grenier et al., 2013), using the FlexPDE software package (Nelson, 2020) as our numerical modelling environment. A 1D model with solely vertical conductive heat transport was constructed. Lateral heat flow will be very limited in these semi-frozen saturated conditions due to the lack of topography in the area. It is further assumed that vertical heat flow is predominant in the active layer on a seasonal timescale. The permafrost model incorporates the 1D equation for conductive heat transfer written as:

$$\frac{\partial}{\partial z}\left(\lambda_t \frac{\partial T}{\partial z}\right) = C_v \frac{\partial T}{\partial t} + \phi \rho_i L \frac{\partial S_w}{\partial t} \tag{2.1}$$

We assumed fully water-saturated subsurface conditions. The transient freeze-thaw heat flow processes include consideration of pore water phase change and the required latent heat of fusion, which is governed by the water saturation curve with an exponential freezing function. Volumetric heat capacity C, thermal conductivity λ and porosity ϕ are soil-specific properties and water versus ice saturation equations are a function of soil properties and temperature. Porosity ϕ controls the pore water fraction, and thereby the bulk λ_t and C_v. Parameter values are listed in Table 2.1. The combination of ϕ (6 values), thermal conductivity of the solids λ_s (16 values) and volumetric heat capacity of the solids C_s (18 values) were varied, resulting in a total of 1728 simulations. Parameter value ranges represent a parameter space covering minimum to maximum values common for permafrost areas as presented in the introduction.

The 1D model represents a vertical domain of 30 meters, in which the top 2 meters is of particular interest as this is where we have validation data available. The top boundary (T_{top}) was forced by a data set composed of the observed temperature at 5 cm depth. We smoothed this forcing data set to mitigate large jumps in temperature forcing, which avoids numerical instability at the boundary. By utilising the observations at a depth of 5 cm, instead of air temperature, surface-atmosphere boundary effects and the effects of potential snow or vegetation insulation did not have to be taken into account in our model description, which would have been difficult to constrain (Liu et al., 2018; Fisher et al., 2016). The bottom boundary (T_{bottom}) had a fixed temperature of -1.12°C, which was found by linearly extrapolating the depth

profiles at all given timesteps to attain a realistic average temperature gradient of 0.02°C/m to a depth of 30 meters. The fixed value for T_{bottom} is realistic since little change in temperature at that depth over the model period of 6 years is expected. See Appendix A.1 for the conceptual model, applied boundary conditions and observed temperatures. There is an organic-rich layer in the top 0.5 meters underlain by sand and gravel. Due to the relatively thin organic-rich layer and lack of geological information for larger depths, we assumed homogeneous thermal and physical properties throughout the 30 meter column disregarding any heterogeneity. The model was run for a total of 6 years of data, of which the first 3 years until October 2013 are used as spin-up and the last 3 years until December 2016 were used for our analysis. Figure 2.1c shows 3 optimised model runs and the observed data at a depth of 80 cm, illustrating the match between model and observation. Figure 2.1d shows the modelled temperature-dependent behaviour of the bulk volumetric heat capacity (C_v) and bulk thermal conductivity (λ_t) (Jafarov et al., 2012) based upon the equations in Table 2.1.

Table 2.1 | Numerical model parameters (Zhao et al., 2018)[a](Dissanayaka et al., 2012)[b], (Abu-Hamdeh & Reeder, 2000)[c], (Mustamo et al., 2019)[d], (Romanovsky & Osterkamp, 2000)[e], (Putkonen, 1998)[f]

Parameter	Description	Parameter value
ϕ	Porosity, $(-)$	variable 0.05 to 0.55[a]
λ_w	Thermal conductivity water, (W/mK)	0.6
λ_i	Thermal conductivity ice, (W/mK)	2.14
λ_s	Thermal conductivity solid, (W/mK)	variable 0.05 to 1.175[b,c,d]
λ_t	Bulk thermal conductivity, (W/mK)	$\lambda_t = \phi(S_w\lambda_w + (1-S_w)\lambda_i) + (1-\phi)\lambda_s$
C_w	Specific heat water, $(J/kg/K)$	4182
C_i	Specific heat ice, $(J/kg/K)$	2060
C_s	Specific heat solid grains, $(J/kg/K)$	variable 525 to 1375[b,e,f]
C_v	Bulk volumetric heat capacity, (J/m^3K)	$C_v = \phi(S_w(C_w * \rho_w) + (1-S_w)C_i * \rho_i) + (1-\phi)C_s * \rho_s$
ρ_w	Density water, (kg/m^3)	1000
ρ_i	Density ice, (kg/m^3)	920
ρ_s	Density solid grains, (kg/m^3)	2650
L_i	Latent heat of fusion, (J/kgK)	334×10^3
S_w	Water saturation curve, (T)	$S_w(T) = (1-S_{wres})exp(-((T-273.15)/W)^2) + S_{wres}$
S_w	For T> 0 °C, (T) = 1	
S_w	For T< 0 °C, function of (T)	
S_{wres}	Residual saturation,	0.05
W	Fitting parameter for freezing function	0.15

2.3.2 | Error measures

The error measures *RMSE*, *KGE* and *Russell's* error are used to evaluate the model performance. *RMSE* is defined in Equation 2.2 and is calculated using the observed temperature (T_{obs}) and modelled temperature (T_{sim}), where an *RMSE* closest to 0 indicates the best performing model:

$$RMSE = \sqrt{\frac{\sum_{i=1}^{n}\left(T_{sim(i)} - T_{obs(i)}\right)^2}{n}} \tag{2.2}$$

KGE is calculated using Equation 2.3 (Knoben et al., 2019), which is a combination of correlation between observation and simulation (r), standard deviation (σ) and bias calculated with the mean of the simulation and observation (μ). A *KGE* <0 indicates that the mean of the observed temperature (T_{obs}) better represents the observation than the modelled temperature (T_{sim}), a *KGE* of 1 indicates the best performance (Gupta et al., 2009):

$$KGE = 1 - \sqrt{(r-1)^2 + \left(\frac{\sigma T_{sim}}{\sigma T_{obs}} - 1\right)^2 + \left(\frac{\mu T_{sim}}{\mu T_{obs}} - 1\right)^2} \tag{2.3}$$

The *Russell* error is unique in the way that it evaluates two different properties, the phase error between two signals and the magnitude error, which are synonymous for the correlation and standard deviation (Russell, 1997; Rokaya & Kim, 2018). The *Russell's magnitude* error (ε_m) is calculated using Equation 2.4 and the *Russell's phase* error (ε_p) using Equation 2.5:

$$\varepsilon_m = sin(m) log_{10}(1 + |m|) \tag{2.4}$$

$$\varepsilon_p = \frac{cos^{-1}(p)}{\pi} \tag{2.5}$$

where p and m are calculated using Equation 2.6 and Equation 2.7, respectively:

$$p = \left(\frac{\sum_{n=1}^{N} T_{obs(i)} T_{sim(i)}}{\sqrt{\sum_{n=1}^{N} T_{obs(i)}{}^2 \sum_{n=1}^{N} T_{sim(i)}{}^2}}\right) \tag{2.6}$$

$$m = \left(\sum_{n=1}^{N} T_{obs(i)}{}^2 - \sum_{n=1}^{N} T_{sim(i)}{}^2\right) / \sqrt{\sum_{n=1}^{N} T_{obs(i)}{}^2 \sum_{n=1}^{N} T_{sim(i)}{}^2} \tag{2.7}$$

The *Russell's comprehensive* (combined) error (ε_c) is a combination of the phase and magnitude error (Equation 2.8). The *Russell's phase* is bound by a scale from 0 to 1 and the magnitude error is scaled so that an order of magnitude difference is approximately equal to 1, and is therefore equal to the worst phase error. The combined

comprehensive error ε_c thus has roughly the same scale, with a value of 1 being considered as the worst performance (Russell, 1997):

$$\varepsilon_c = \sqrt{\frac{\pi}{4}\left(\varepsilon_m^2 + \varepsilon_p^2\right)} \tag{2.8}$$

In this thesis, reference to the *Russell's* error refers to the comprehensive error.

2.3.3 | Future scenario

To investigate the effect of the optimal *RMSE*, *KGE* and *Russell* errors on 100 year predictions of active layer depth, we used a second 1D model and impose a hypothetical scenario of QTP surface warming at the surface boundary. This second 1D model was adjusted to have a domain depth of 100 meters and a bottom boundary flux of 0.065 W/m^2, which is in the range of geothermal heat fluxes inferred for the QTP (Wu et al., 2010). A shallow fixed temperature bottom boundary condition could lead to an excess of heat storage in the subsurface, therefore a heat flux for T_{bottom} ensures that the development of the permafrost thaw depth over a 100 year period is not limited by a fixed bottom value (Stevens et al., 2007). The time series of imposed surface temperature, T_{top}, is based upon the observed 5 cm ground temperature as used in the first model, but extended to cover a period of 100 years. The observed data set was used since it contains seasonal variability, mimicking real world conditions. The IPCC scenarios project an average temperature increase in the Arctic between 2 to 9 °C in 2100 (Anisimov et al., 2007). The T_{top} boundary has a gradual linear temperature increase of 0.05 °C/*year* (Nan et al., 2005). The model initial conditions were created using a steady-state model and are identical for all of the models, subsequently a transient model ran over the 100 years for the 3 parameter combinations.

2.4 | Results

Figure 2.2a shows the variability of fit considering the three parameters (C, λ and ϕ) for the *RMSE* error. The parameter space shows a complex interplay in performance determined by the sensitivity of the model fit for each parameter. *KGE* and *Russell* parameter spaces show similar behaviour. Figure 2.2b shows the sensitivity of the model for each parameter, keeping the other two parameters fixed at their optimal value. The final column in Figure 2.2b summarises the optimal parameter combinations. The optimum RMSE parameter space has high volumetric heat capacity and porosity, whereas the optimal *KGE* and *Russell* errors have more comparable optimum parameter values. *KGE* and *Russell* both have comparable values for volumetric heat capacity, and the same optimum values for thermal conductivity and porosity. For

both the *RMSE*, *KGE* and *Russell's* error, a change in volumetric heat capacity results in only a very small change in error (Figure 2.2b). However, variations in thermal conductivity and soil porosity have a much stronger impact on the error between observation and model, indicating a higher sensitivity. The optimal values indicated with the dots all have a local minimum or maximum, indicating that the applied parameter space covers the required range.

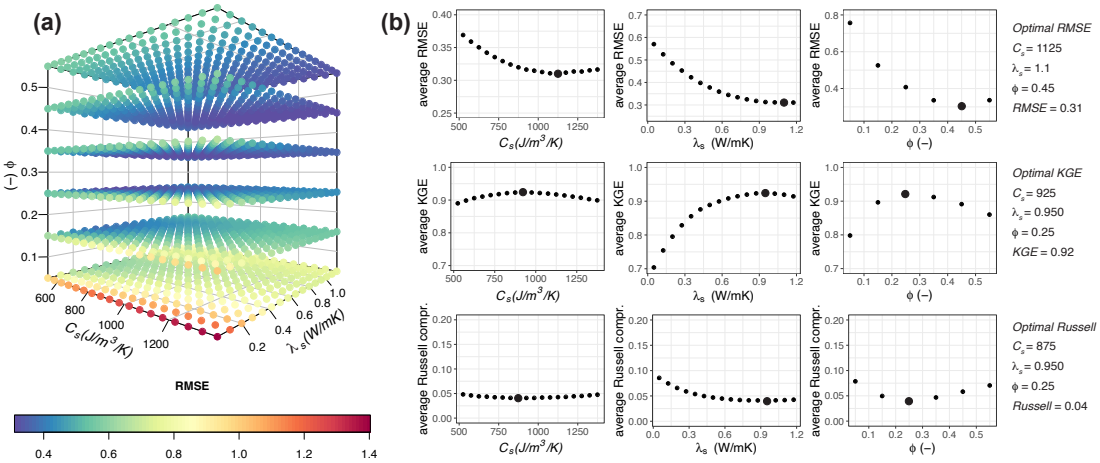

Figure 2.2 | Figure (a) shows the average RMSE between the observations and model results for the investigated parameter space. Figure (b) shows the sensitivity of the parameter space for the various error measures where the optimal parameter values with the lowest error are indicated by the enlarged dots.

The fit varies between observed temperatures and simulated temperatures for the optimised parameter values for each error analysis. Each model accurately simulates the observed temperature data up to 80 cm (Figure 2.1c). Yet gradually towards 200 cm depth, a mismatch up to 0.5 °C occurs between observed and simulated temperatures for certain time periods. When reviewing the small-scale dynamics (Figure 2.1c), observed temperatures show more variability in temperature over a greater range compared to the simulated data. At depths of 80 to 200 cm, the observed temperature variations are smaller compared to large near-surface temperature fluctuations, and the model more accurately captures these dynamics. When investigating the timing of the onset of thawing and associated water-ice phase transition, a short time-lag appeared between the observations and the model. At 80 to 200 cm, observed freezing occurs slightly before the simulated freezing.

Figure 2.3a shows the simulated temperatures of the hypothetical 100-year future prediction for the models with the lowest *RMSE*, *KGE* and *Russell's* error. There are clear differences in timing when temperatures switch from sub-zero freezing conditions to positive temperatures. The total period of the phase transition, when temperatures

are in the zero curtain period (mushy-zone) and show little change, varies between the optimised models. Figure 2.3b shows the 100 year model forecast of the active layer depth based upon 3 optimal parameter combinations from Figure 2.3a. The seasonal active layer signal is presented as a smoothed yearly (maximum) active layer depth. The initial 40 years (1) show a slowly deepening active layer for all three models. After 40 years (2), the active layer appears to drastically increase in depth for all models and the once stable permafrost appears to collapse with steep thawing rates. The active layer depth for the *Russell* and *KGE* error starts to increase first and shows an average thawing rate of 0.11 and 0.09 *m/year* when the slope is stable (2). The *RMSE* error active layer depth lags about 15 years behind *Russell* and *KGE* with a comparable increase in active layer depth of 0.10 *m/year* after 60 years. This time-lag is the time before the two models achieve the same thawing depth. The active layer has developed into a suprapermafrost system, with a perennially thawed aquifer below the active layer which will not refreeze completely in winter. Overall there appears to be a period with a stable active layer, followed by a gradual increase in active layer depth, succeeded by a period of strong active layer development.

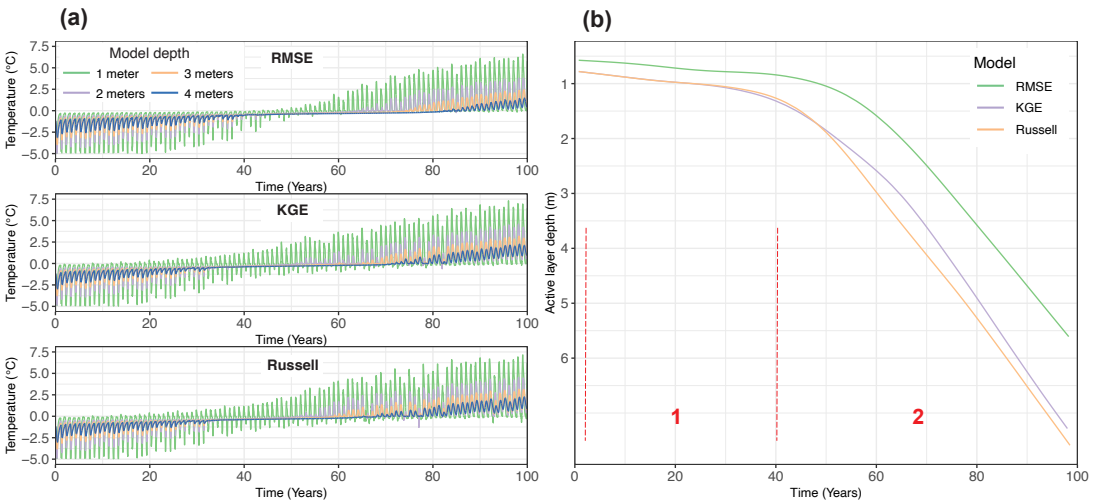

Figure 2.3 | Figure (a) shows the temperature development at 4 depths for the optimal parameter combinations determined with the *RMSE*, *KGE* and *Russell* error measures for the 100-year scenario. Figure (b) shows the interpolated active layer depth based upon the optimal parameter combinations.

2.5 | Discussion and Conclusion

Satisfactory agreement between modelled and observed temperatures was found close to the surface, but a temperature mismatch developed for increasing depth. Clearly, in reality there is heterogeneity in subsurface thermal properties, as a result of stratification in the active layer. Organic matter content and porosity vary

with depth, with higher organic matter contents in the upper 50 cm which could act as an insulator, and lower content at depth (Zhao et al., 2018). Influence from the surface-atmosphere boundary such as snow cover can be excluded as a reason for the mismatch since the models were forced with the observations at 5 cm depth, where complex surface boundary interactions are implicitly part of the model. The mismatch between data and model is mainly visible during phase 4 (Figure 2.1), when temperatures increase during summer, not during freezing. Similarly, Albers et al. (2020) observed that the thermal parameters of their numerical permafrost model are more sensitive close to the surface and during summer time, as this is the time when the active layer is most developed. The temperature mismatch between 100 and 200 cm depth is likely caused by active layer stratification and the statistical method by which the optimal parameter set was determined. By averaging the calculated errors over depth, the model porosity is also averaged over the entire profile, whereas in the field the porosity is variable with depth. The optimal porosity value better represents the top of the profile, given the sensitivity of the porosity, a small change in porosity at depth impacts the modelled temperature substantially. Future modelling efforts could improve model performance by including more layers into the system, at the cost of overall uncertainty due to the doubling of parameters.

The optimal parameter values found in our study agree with ranges reported in the literature. Zhao et al. (2018) found average ϕ values of 0.25 (-) at a depth of 50 cm for the same region at the QTP. Luo et al. (2018b) observed a thawed summer soil moisture content of 35% at 80 cm depth, which is what would be expected in a fully saturated soil with a ϕ of 0.35 $(-)$ and is in the same range as the optimal ϕ from the *RMSE* and *KGE / Russell* parameter combination. A measurement campaign by Chen et al. (2020) used an empirical relation based upon the volumetric moisture content to calculate the bulk thermal conductivity (λ_t) and different soil fractions to calculate the bulk heat capacity (C_v) at two locations around the measurement site at the QTP. The bulk heat capacity (C_v) during the cold and warm season varied between 1.4-2.4 $\times 10^6 J/m^3$K and the bulk thermal conductivity (λ_t) between 0.8-1.3 W/mK. When recalculating the optimal parameter space from our study to bulk values using the equations in table 2.1, C_v varies between 1.82-1.94 $\times 10^6 J/m^3$K and λ_t between 1.0-1.2 W/mK for temperatures above 0 °C, which is in the same range. The thaw rates between 0.09 and 0.11 $m/year$ that developed over the second half the 100 year model period are of similar order with a QTP averaged thaw rate of 0.07 $m/year$ observed by Wu et al. (2012).

The three parameters varied during the study, C_s, λ_s and ϕ have different effects on model sensitivity. Model sensitivity for a change in C_s is low and λ_s and ϕ have higher model sensitivities. ϕ controls the amount of liquid water and ice in the pore space,

and thereby the required latent heat of fusion during phase transition. When temperature gradients during freeze-thaw transitions are limited or of a short time period, there can be a deficit in the energy supply to complete the phase transition. Consequently, the pore water will remain in the 'mushy zone', and will not completely thaw. The sensitive nature of ϕ and λ_s affects the accuracy of long-term predictions, as is demonstrated with the hypothetical 100 year scenarios. Over the 100 year model period (Figure 2.3), the differences between the optimal parameter combinations are visible. There are small differences in thawing rate and a 15 year time-lag developed that is likely the result of the larger/lower ϕ for the latter models. Due to a higher ϕ, the water content increases, subsequently requiring more energy to complete the phase transition. Over the first period (1), the active layer depth is deeper for *KGE* and *Russell*, because they have a lower ϕ and thus lower water content. As a result, the active layer thaws to a deeper depth during the summer period compared to the *RMSE* parameter combination. The time-lag of 15 years can be considered as very significant because it impacts timing of active layer thaw and activation of solute transport from thawing permafrost. This highlights that model error uncertainty has a high impact on the overall uncertainty of active layer development models.

The QTP is an area of interest subjected to ongoing research related to active layer thaw and permafrost degradation. Permafrost thaw modelling is frequently used to study the evolution of the active layer (Qin et al., 2017; Sun et al., 2020b). This research demonstrates a method to analyse observed data to determine the porosity and thermal properties of the active layer. This helps to improve model parameterisation and increases our understanding of the timescale of active layer thaw and the uncertainties involved. Our method is capable of acquiring satisfactory thermal properties from direct subsurface temperature observations. The presented method is well suited to be applied to other permafrost sites with predominantly conductive heat flow, due to the straightforward 1D nature of the model setup. However, careful consideration should be taken with respect to snow melt or precipitation infiltration, as this can cause advective heat flow. Our approach reduces the need for intensive laboratory research by using temperature observations to determine the soil specific thermal properties, which could be applied to other permafrost temperature observations on the QTP and across other permafrost areas. This also avoids the need for thermal property estimation based upon surface data and empirical relations. The analysis showed that next to the model parameters, the error measures also have a sensitivity range, which are usually not considered in permafrost modelling studies, but do have a large impact on long-term active layer predictions. Sensitivity analysis of the error measure should therefore become an integral part of the overall system sensitivity analysis. As shown in this study, over longer periods, substantial differ-

ences in active layer thawing rate and depth prediction arise, due to the use of the various error measures. The QTP active layer is a tipping point system, as once a certain threshold is exceeded, the system changes state and cannot return easily to the old state. Once the QTP active layer thickness exceeds the threshold, the active layer system collapses and livelihoods will be affected due to potentially irreversible environmental changes. A well founded understanding of permafrost thaw, timing and uncertainty are therefore of vital importance to understand the sensitivities of the system and inform communities about the implications for their livelihoods.

3

Relating thermal properties to soil characteristics

This chapter is based on:

de Bruin, J. G. H., Bense, V. F., van der Ploeg, M. J. (2023). Soil thermal properties during freeze–thaw dynamics as function of variable organic carbon and grain size distribution, *Vadose Zone Journal*, 22(3), e20252, doi:10.1002/vzj2.20252

Abstract

Permafrost regions are experiencing increasing air temperatures, accelerating the thawing process and thickening the active layer in summer. This can accelerate the release of greenhouse gasses into the atmosphere from the organic carbon stored in the permafrost. The long-term thawing rates of permafrost below the active layer are governed by the soil thermal properties, the heat capacity and thermal conductivity, which vary due to differences in grain sizes and distribution and organic matter content. Using nine column experiments comprised of fully saturated synthetic permafrost samples exposed to freeze-thaw cycles, the relative contributions of a range of soil grain sizes and organic matter contents on the soil thermal properties was investigated. The columns were subjected to a freeze and thaw cycle while soil temperatures were recorded in profiles. To infer the thermal properties from these experimental data, a numerical heat transfer model was used. The best fit between the observations and a batch of 5544 numerical models was used to find optimum values for permafrost thermal properties. The optimised heat capacity varied between 500 to 650 (J/m^3K) and thermal conductivity between 2.45 to 3.55 (W/mK). These optimised parameters were subsequently used to model a 100 year permafrost active layer thaw scenario under warming air temperatures. Variations in the optimised thermal properties resulted in a time difference in thawing depth of 10 to 15 years and thawing depths varied between 9 to 10 meters between the different optimised thermal properties at the end of the 100 year scenario.

3.1 | Introduction

3.1.1 | Permafrost thaw

Approximately 24% of the Northern hemisphere is underlain by permafrost (Dobinski, 2011; Hugelius & Kuhry, 2009; Strauss et al., 2017). It contains an estimated 1035 Pg of organic carbon in the top 3 meters of the subsurface opposed to an estimated 2050 Pg in the rest of the Earth's top 3 meters below the ground surface (Tarnocai et al., 2009; Vardy et al., 2000; Schuur et al., 2008; Jobbágy & Jackson, 2000). As a result of increased annual air temperatures, the active layer thickens and permafrost thaws (Biskaborn et al., 2019). Microbial activity within the permafrost increases as temperatures rise above 0 °C (Patzner et al., 2020). This accelerates microbial decomposition of organic matter and the release of the organic carbon as greenhouse gasses CO_2 and CH_4 into the atmosphere and dissolution into groundwater (Mu et al., 2016; Schuur et al., 2008, 2009; Vonk et al., 2013a). As a result of the thawing processes, the vast store of permafrost organic carbon is becoming part of the active global carbon cycle. Models used to investigate permafrost dynamics under different climatological conditions help to gain insight into thaw rates, thawing depths and the reactivation of groundwater flows and associated carbon transport (Bense et al., 2009; Mohammed et al., 2021, 2022). However, parameterisation of the thawing processes is challenging and requires judicious modelling choices (Lamontagne-Hallé et al., 2020). Few data are available on the actual key soil thermal properties, namely the thermal conductivity and heat capacity. Parameterisation schemes have been developed to calculate the thermal properties, but their performance is low due to limited data of soil thermal properties during the transition from frozen to thawed conditions, which is a subject that has received little attention (He et al., 2020)

3.1.2 | Thermal properties

The thermal properties govern two heat transfer processes; heat transfer by conduction and advection. Conductive heat transfer is often the primary heat transport process in the permafrost subsurface, advective heat transfer is not activated as long as the groundwater is in a frozen state (Hayashi et al., 2007). Thermal properties consist of the thermal conductivity λ (W/mK) and heat capacity C (J/m^3K). All constituents found in a permafrost soil; organic material, grain particles with a grain size distribution and pore space partially or fully filled with soil moisture, have individual thermal properties, which can be averaged together in various ways to form the bulk or effective thermal conductivity λ_v and heat capacity C_v (Midttømme & Roaldset, 1998; Grenier et al., 2018; Yang et al., 2021).

Effective thermal properties across the freeze-thaw interval are difficult to model, as the thermal properties are altered during phase change (Zhang et al., 2018). During this crucial phase pore water becomes partially liquid, a process that is described using a Soil Freezing Characteristic Curve (SFCC) and varies for different soil types, saturation levels and grain size (Kurylyk & Watanabe, 2013). The liquid porewater could activate groundwater movement and transport dissolved CO_2 and CH_4. Heat transport processes during this phase are highly nonlinear and are strongly controlled by water saturation levels. There is still uncertainties on the link between soil properties such as grain size, organic matter content and the resulting thermal properties during the phase change transition (He et al., 2020).

Research has been performed into the relation between the thermal properties and grain size, organic matter content and moisture content using the heating probe method in laboratory setups, resulting in models for the prediction of the thermal properties from such parameters (Abu-Hamdeh & Reeder, 2000; Hamdhan & Clarke, 2010; Dissanayaka et al., 2012; Zhang et al., 2018). Furthermore, Midttømme & Roaldset (1998) have investigated the effect of a range of various particle fractions on thermal conductivity and the thermal properties of mineral quartz fractions where they found a relation between grain size and thermal conductivity, and Mustamo et al. (2019) investigated thermal properties of peaty soils at the freeze-thaw interval.

Although much research has focused on permafrost thermal properties, these studies so far have not include the freeze-thaw transitions of fully saturated sandy soils. Here we investigate permafrost built up out of sedimentary sand with a variability in grain size and organic matter contents over the freeze-thaw interval. To investigate these nonlinear heat transport processes, we used column experiments in a laboratory environment to collect data, and use a numerical heat transfer model to determine effective thermal properties.

3.1.3 | Column experiments

Column experiments are typically used to recreate field conditions, where a soil column is radially insulated from its surroundings (Nagare et al., 2012b). The primary heat transport direction will be thereby vertical, creating a 1D heat transport system (Hayashi et al., 2007; Mohammed et al., 2014). Zhou et al. (2006); Nagare et al. (2012b) stressed the importance of creating as best as possible 1D heat transfer conditions, and minimise radial ambient temperature interference.

Previous column experiments by Nagare et al. (2012b) and Nagare et al. (2012a) collected a large active layer sample of Arctic peat and brought it to the lab to measure soil moisture and temperature profiles within a 1D soil column as it thawed. Simil-

arly, Mohammed et al. (2014) used synthetically made peat samples to simulate active layer thaw using a 1D soil column experiment. The experiment by Watanabe et al. (2011) used unsaturated sandy, loam and silt loam soils during the freeze-thaw experiments. In our research we will focus on silty and sandy soils with variable organic matter contents under fully saturated conditions.

3.1.4 | Research aim

The main aim of our study is to quantify the combined effects of various organic matter contents and soil particle size distributions on the bulk thermal conductivity and heat capacity at the freeze-thaw transition around 0°C. This was achieved by creating a comprehensive representative data set for freeze-thaw characteristics in permafrost soils that highlights the differences in temperature propagation between samples consisting of contrasting grain sizes and organic matter contents. It is hypothesised that the thermal conductivity of the solid fraction would decrease with a higher organic matter content, due to the relative lower thermal conductivity of organic matter compared to sand, thereby changing the propagation speed of the freezing and thawing front. The samples were housed within soil columns and placed in a climate chamber, where temperature observations were gathered during simulated freezing and thawing events. This data set was then used to study the influence of the these soil physical parameters on the thawing behaviour and thus thermal properties of sandy permafrost with varying organic matter contents.

This chapter is a continuation of Chapter 2, where the thermal properties of the active layer were determined using numerical models based upon solely temperature observations recorded at various depths over a 6 year period at the Qinghai-Tibetan Plateau. In this chapter we use the same approach to determine the thermal conductivity and heat capacity using a modified version of the numerical heat transfer model from Chapter 2. However, the temperature observations are collected using the 1D soil column experiments, instead of in the field. We aim to reconstruct the same temperature dynamics in the soil column experiments as observed in the field, but at a faster evolving timescale.

3.2 | Materials and Methods

3.2.1 | Experimental setup and instrumentation

A total of nine freeze-thaw experiments with synthetic soil columns were conducted within a temperature controlled climate chamber (Figure 3.1). The experiments were performed in two batches of five and four simultaneous soil column experiments.

We use High Density Poly Ethylene (HDPE) tubes to house the soils, with an inner diameter of 0.315 m, a wall thickness of 0.028 m and total height of 1.2 m. Figure 3.2 (a) shows the HDPE tube which is on the sides and on the top insulated with 0.12 m thick shell rockwool insulation. The passive insulation reduces steep radial temperature gradients, resulting in a small radial heat flux which is monitored using temperature sensors in between the column and the insulation and accounted for during the analysis as it is part of the numerical model. At the bottom of the soil column, an detachable aluminium plate with a width and length of 0.4x0.4 m with a thickness of 0.02 m acts as a base; fixed with 12 heavy duty bolts and a rubber o-ring, sealing off the bottom. Simultaneously, the aluminium plate serves as a conductor to transfer heat to and from the base of the soil column to the surrounding air. In the climate chamber, the air temperature could be controlled from a range of -4°C to 20°C.

All soil columns were equipped with calibrated temperature sensors (Campbell Scientific T107). The sensors had a measurement range from -35 to 50°C and accuracy of 0.01°C. The sensors were positioned at heights of 0.05, 0.2, 0.35, 0.5, 0.65, 0.8 and 0.95 m above the column base in the middle of the sample. Sensors wires were fed through the HDPE column wall using watertight wirelock nuts. Temperature values were logged at 300 second intervals using a Campbell Sci. CR1000X logger. Two temperature sensors were placed in the climate chamber to measure the climate chamber air temperature.

3.2.2 | Soil Physical Properties

Two freezing and thawing experiments were run with varying soil grain sizes and organic matter contents. The sedimentary grain sizes ranged from silty (D_{50} of 175 µm) to medium sand (D_{50} of 730 µm). To obtain these ranges, we used well sorted quartz sand which was sieved in calibrated sieves to achieve the three grain size ranges as reported in Table 3.1. Based upon the carbon contents reported in the studies by Siegert et al. (2002); Zimov et al. (2006); Strauss et al. (2013); Dutta et al. (2006) we selected three average carbon contents for sedimentary deposits. We have added 1 %, 5 % and 10 % of the total dry sand weight in organic matter to the mixture. Table 3.1 gives an overview of the used soil grain size range and organic matter contents. Organic potting soil was selected as representative organic matter, composed from Swedish and Baltic peat with added perlite. The organic matter composition of these peat soils is considered representative for northern latitude peat permafrost soils. The non-organic perlite is a part of the organic potting soil and has a low bulk density and high water capacity holding properties and was present in concentrations varying from 19 to 26 wgt% in five of the nine of the samples, and will contribute to

Figure 3.1 | Photo of two out of nine columns during the freeze/thaw experiment. Each column of 1.2 m high and 0.315 m diameter is wrapped in 0.12 m thick insulation material held in place with duct tape and placed on a plastic pallet to isolate it from the ground. Also visible are the temperature sensor cables that come out of the insulation.

the bulk thermal properties of the soil material. All samples were mixed in an industrial mixer for 1 hour to create homogeneous samples, thereby preventing any measurements being affected by layering of the material. The columns were filled up to 1 m with soil material using the slurry packing technique with manual compaction (Lewis & Sjöstrom, 2010), which should result in an uniform packing and fully saturated samples, mimicking water saturated sedimentary deposits. Then a layer of 0.1 m of water was added on top of the soil material. This provided a buffer medium on top of the sample that created a stable temperature boundary during the experiment. Furthermore, it had known thermal properties which was required during subsequent modelling.

After the freeze-thaw experiment, to determine the porosity and organic matter content, all nine soil columns were sampled at different depths using 100 *cc* sample rings. The porosity measurements helped to check the uniform packing of the samples and establish the water content within the samples. Each soil column was sampled with four sample rings, where two samples were collected at 0.8 m height and two at 0.5 m height within the column. Porosity was determined by measuring the mass differ-

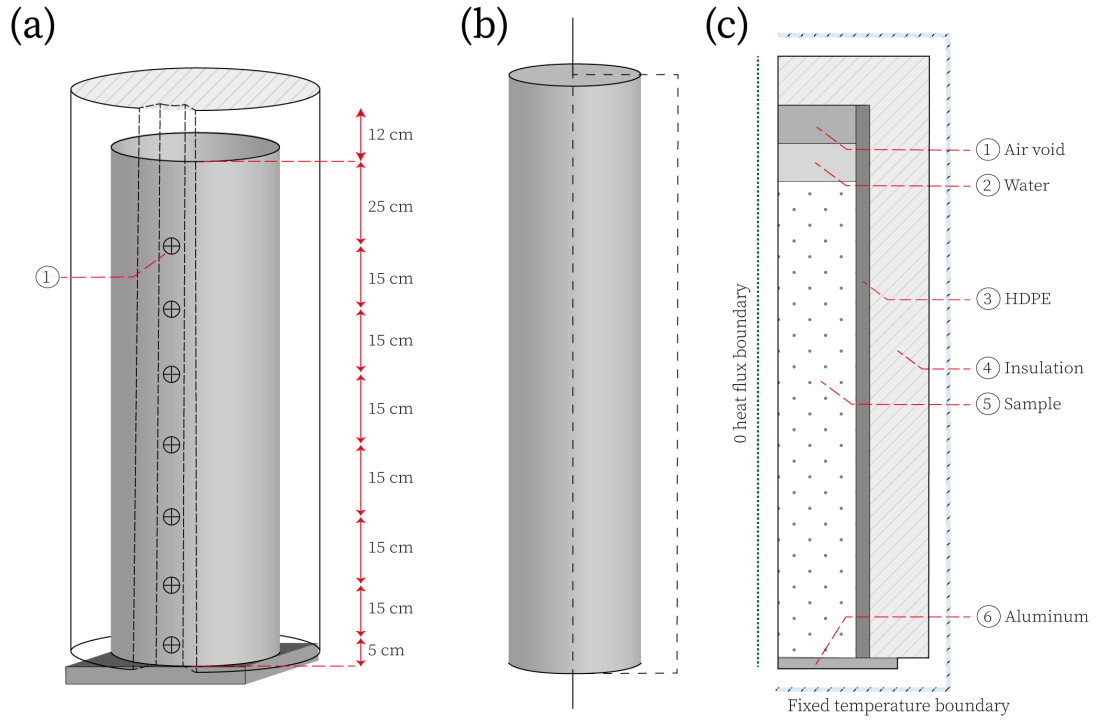

Figure 3.2 | (a) Cross-section of experimental setup with an inner HDPE column equipped with (1) T107 temperature sensors, insulated by 0.12 m thick shell insulation. (b) Translation of 3D soil column to the radial 2D heat transfer model domain. (c) Model domain and applied boundary conditions. Thermal properties assigned to materials can be found in Table 3.1.

ence between a fully saturated and fully dried sample divided by the volume of the ring. Drying of the sample took place in an oven at 105°C for a duration of at least 24 hours, evaporating the porewater but preserving the organic matter (Wilke, 2005). Organic matter content was determined using the Loss on Ignition (LOI) technique (Heiri et al., 2001; Wilke, 2005). Organic matter of a total of five samples are corrected for the perlite concentration, which was determined using the LOI technique.

Table 3.1 | Soil physical properties used in this study

No.	Particle grain size range (µm)	D_{50} (µm)	Soil volume (kg)	Organic matter (kg)
1	100-300	175	75	0.75
2	200-500	350	75	0.75
3	500-800	730	75	0.75
4	100-300	175	75	3.65
5	200-500	350	75	3.65
6	500-800	730	75	3.65
7	100-300	175	75	7.5
8	200-500	350	75	7.5
9	500-800	730	75	7.5

3.2.3 | Experimental temperature conditions

The temperature in the climate chamber followed an pre-determined trajectory, mimicking temperature transitions at the freeze-thaw interval. At the start of the experiment, the climate chamber and samples had a uniform temperature of 3°C. The temperature of the climate chamber was instantly lowered to -3°C, starting the freezing process of the samples from the bottom-up with a vertically upward propagating freezing front. The climate chamber temperature was held stable at -3°C until the samples were fully frozen and had obtained a uniform temperature distribution. After a stabilisation period, the temperature in the climate chamber was instantly increased to 3°C, starting the thawing process. This was a single step increase which created a sharp temperature gradient, causing a quick melting process. The steep temperature gradient highlights any effects that the soil thermal properties have on the propagation of the freezing and thawing front as the processes occurs over a shorter timescale. The freezer unit responsible for temperature management in the climate chamber periodically thawed itself to remove ice buildup on the freezer unit. This caused some temperature fluctuations in the air surrounding the soil column during freezing.

3.2.4 | Permafrost heat transfer model

We use the software FlexPDE to solve the energy transfer equation considering heat conduction and phase change (Nelson, 2020) which is successfully applied in previous research (Bense et al., 2009; de Bruin et al., 2021).

$$\frac{\partial}{\partial z}\left(\lambda_t \frac{\partial T}{\partial z}\right) = C_v \frac{\partial T}{\partial t} + \phi \rho_i L \frac{\partial S_w}{\partial t} \tag{3.1}$$

The energy transport equation (Equation 3.1) uses the bulk thermal heat capacity of the various materials C_v (J/m^3K), and bulk thermal conductivity λ_v (W/mK) to calculate the energy balance over the model domain. All material specific and model parameters can be found in Table 3.2. The model relies both on physical parameters that are coupled to material specific properties such as the thermal conductivity and heat capacity of solid grains and water, and equations that describe system properties and behaviour based upon empirically determined relations. In our study, bulk thermal conductivity (λ_v) and bulk heat capacity (C_v) were calculated by a volumetric average approximation of which the equations are listed in Table 3.2 (McKenzie et al., 2007), yet there are other methods as well to determine the bulk thermal properties. Here the individual thermal properties of water, ice and solids form fractions of the

total bulk thermal properties. This is based upon the porosity, saturation level, liquid water and ice-fraction within the pores.

The Soil Freezing Characteristic Curve (SFCC) is the curve that describes the fraction of pore water that partly freezes or thaws at sub-zero temperatures as a function of temperature, also known as the mushy zone (McKenzie et al., 2007; Kurylyk & Watanabe, 2013). In this model, SFCC is represented by the water saturation (S_w) which is an exponential temperature dependent function which is controlled by the dimensionless parameter W that determines the shape of the curve (Table 3.2). A small part of the pore water remains liquid at sub-zero temperatures, because of an increase in concentration of dissolved solids that are excluded from ice formation, and adsorbtive and capillary forces that depress the freezing temperature of the unfrozen water (McKenzie et al., 2007; Romanovsky & Osterkamp, 2000). This is set with the residual saturation fraction (S_{wres}). Parameter values for the SFCC are manually fitted once against the observations, and subsequently used for all the numerical models. Individual fitting of the SFCC parameter values would exponentially increase the amount of numerical models.

The model domain of the soil column was modelled as a 2D cylindrical half space (Figure 3.2b), thereby capturing heat transport in both the vertical and radial direction. This allowed us to better represent the actual heat transfer gradients in the column than would be possible with a 1D model, but limiting the computational load involved in a full 3D model environment. Figure 3.2c shows the model domain and applied boundary conditions. The left boundary condition represents the centre rotation axis of the cylindrical domain with a zero flux boundary. All other sides of the model domain were forced by the smoothed observed air temperature. Temperature observation were recorded every 300 seconds and were smoothed to 2 hour average temperatures. This was to dampen strong temperature fluctuations at the model boundaries and to reduce the computational load of the model. Not the entire freeze-thaw cycle was modelled, but only the thawing interval starting at the moment that the air temperature was increased to 3°C. This was because for the modelling and determination of the thermal properties, we use the undisturbed observed temperature signal as there are small temperature fluctuations in the climate chamber that occur only during the freezing process as the freezer unit periodically thaws.

3.2.5 | Heat transfer model analysis

By varying the solid grain heat capacity (C_s), solid grain thermal conductivity (λ_s) and porosity (ϕ) a parameter space was created of a batch of 5544 unique combinations. Each model was forced with the 2 hour averaged temperature observation.

Table 3.2 | Numerical model parameters (McKenzie et al., 2007)[a], (Grenier et al., 2018)

Parameter	Description	Parameter value
ϕ	Porosity	0.1 to 0.6
λ_a	Thermal conductivity aluminium (W/mK)	190
λ_h	Thermal conductivity HDPE (W/mK)	0.38
λ_{ins}	Thermal conductivity insulation (W/mK)	0.033
λ_w	Thermal conductivity water (W/mK)	0.6
λ_i	Thermal conductivity ice (W/mK)	2.14
λ_s	Thermal conductivity solid grains(W/mK)	0.05 to 3.55
λ_v	Bulk thermal conductivity (W/mK) [a]	$\lambda_v = \phi(S_w\lambda_w + (1-S_w)\lambda_i) + (1-\phi)\lambda_b$
C_a	Volumetric heat capacity aluminium (J/m^3K)	910
C_h	Volumetric heat capacity HDPE (J/m^3K)	1900
C_{ins}	Volumetric heat capacity insulation (J/m^3K)	840
C_w	Volumetric heat capacity water (J/m^3K)	4182
C_i	Volumetric heat capacity ice (J/m^3K)	2060
C_s	Volumetric heat capacity solid grains (J/m^3K)	500 to 1150
C_v	Bulk Volumetric heat capacity (J/m^3K) [a]	$C_v = \phi(S_wC_w + (1-S_w)C_i) + (1-\phi)C_s$
ρ_w	Density water (kg/m^3)	1000
ρ_i	Density ice (kg/m^3)	920
ρ_s	Density solid grains, (kg/m^3)	2650
L_i	Latent heat of fusion J/kgK	334×10^3
S_w	Water saturation curve, (T)	$S_w(T) = (1-S_{wres})exp(-((T-273.15)/W)^2) + S_{wres}$
S_w	For T> 0 °C, (T) = 1	
S_w	For T< 0 °C, function of Temperature	
S_{wres}	Residual saturation,	0.05
W	Fitting parameter for freezing function	0.15

Subsequently, the model results were compared against the observed temperatures from the nine experiments. For each of the nine experiments a subset of the total parameter space was made, selecting only the models with a porosity identical to the observed porosity. Thereby optimising the thermal conductivity and heat capacity, but constraining the total parameter space of the optimisation based upon the observed porosity. Using the Kling-Gupta Efficiency (KGE) error measure (Equation 3.2), the best fit between the model and observed data was determined. This resulted in nine optimised parameter combinations for all nine experiments. The KGE error measure comprises out of a bias (μ) between model (T_{sim}) and observation (T_{obs}), a scale misfit (σ) and the correlation (r) between model and observation (Knoben et al., 2019) and was successfully applied in previous numerical model optimisation studies (de Bruin et al., 2021).

$$KGE = 1 - \sqrt{(r-1)^2 + \left(\frac{\sigma T_{sim}}{\sigma T_{obs}} - 1\right)^2 + \left(\frac{\mu T_{sim}}{\mu T_{obs}} - 1\right)^2} \tag{3.2}$$

3.2.6 | Optimum parameter scenario

To investigate the sensitivity of the thaw-depth rate to model uncertainty, we performed an analysis of the long-term effect of the parameter space on temperature propagation. The nine optimised parameter combinations based upon all parameter values were used to model a hypothetical 1D permafrost active layer thaw scenario over a 100 year period. The top boundary consisted of daily averaged air temperature observations observed over a 6 year period at the Qinghai-Tibetan Plateau (QTP), which were repeated over a 100 year period to create seasonal fluctuations. A linear temperature increase of $0.05°C/yr$ was added, which is representative for IPCC arctic climate warming scenario SSP5-8.5 (Constable et al., 2022; de Bruin et al., 2021). Initial temperature conditions were created using a steady state model, which were subsequently used in the transient model as the initial conditions. The transient 1D model had a domain depth of 100 meters where the bottom boundary consists of a fixed flux boundary of $0.065\ W/m^2$ which was in range for geothermal heat fluxes at the (QTP) (Wu et al., 2010). The optimised thermal properties were applied over the entire depth domain, and optimised porosity over the top 20 meters of the domain, a fixed porosity of 0.25 $(-)$ was applied over the remainder of the domain as the optimised porosity was not representative for depths larger than 20 meters. The resulting temperature models were analysed to illustrate the development of the active layer depth and overall thaw depth over time.

3.3 | Results

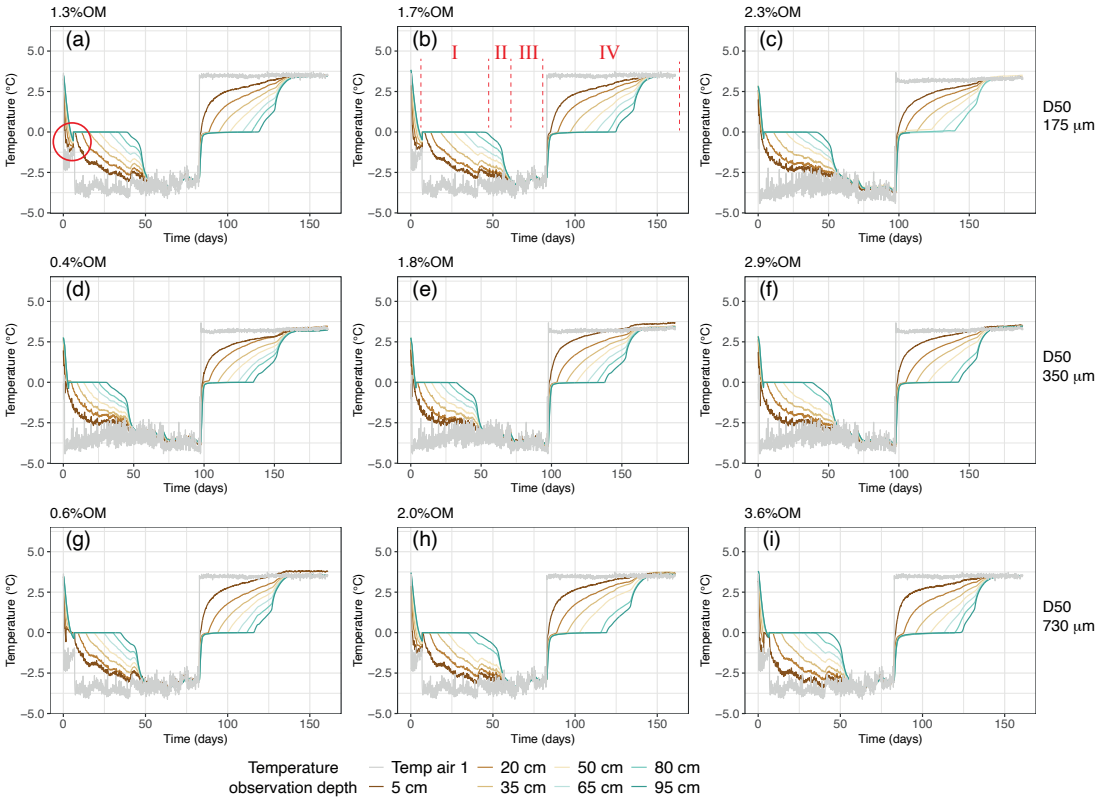

Figure 3.3 | Temperature time series of all nine experiments showing distinct freezing and thawing curves and a propagation of the thawing front as a function of organic matter content and grain size distribution. Depths are measured starting at the base of the columns.

3.3.1 | Temperature observations

The temperature observations collected from the nine experiments in Figure 3.3 shows the temperature development at different depths within the soil columns during the freezing and thawing cycles over the two batches of five and four simultaneous soil columns. The observations in the figure were smoothed from 5 min observations to 2 hour average temperatures. All observations within the soil columns show a similar temperature pattern. During the first phase (I) Figure 3.3b, the air temperature drops from +3°C to −3°C. The temperature in the soil column decreases to 0°C and enters a phase change state. A number of temperature observations show during initial freezing supercooling of the porewater for a short period of time indicated by the red circle in Figure 3.3a, where after temperatures increase to 0°C (Akyurt et al., 2002; Ren & K.Vanapalli, 2019). During the propagation of the freezing front, temperatures remain stable at around 0°C. During the phase change period, the soil column is partly frozen, and the mixture remains at a stable temperature until the pore water is crystallised. After crystallisation of the porewater within the entire column (phase two (II))

the temperature decreases to the set temperature applied at the bottom boundary. During phase (III), temperatures within the column stabilise and respond quickly to external temperature fluctuations. During phase IV, the temperature in the climate chamber is increased to +3°C and a thaw propagates upward through the soil column. During the thawing process, the observed temperature gradients are initially steep, and gradually decreases towards the end temperature of +3°C. The observed air temperature shows significantly higher temperature fluctuations compared to the observation within the soil column, which are more buffered. When the thawing phase starts, the observed temperatures develop in a similar manner as during freezing. As the air temperature is increased to +3°C, temperature within the column responds "quickly" and stabilises at 0°C within ∼ 40 days. Pore ice starts to melt until all pore ice is melted. Thereafter, the 0°C front propagates vertically through the column, with an initial steep temperature gradient followed by a more gradual temperature increase. During the freezing phase (I), the observations at 0.05 and 0.20 m depth show more fluctuations compared to the thawing phase (III), as a result of the periodic defrosting of the freezer unit. In Figure 3.3c, the temperature observation at 0.95 m depth suffered a malfunctioning sensor after 105 days.

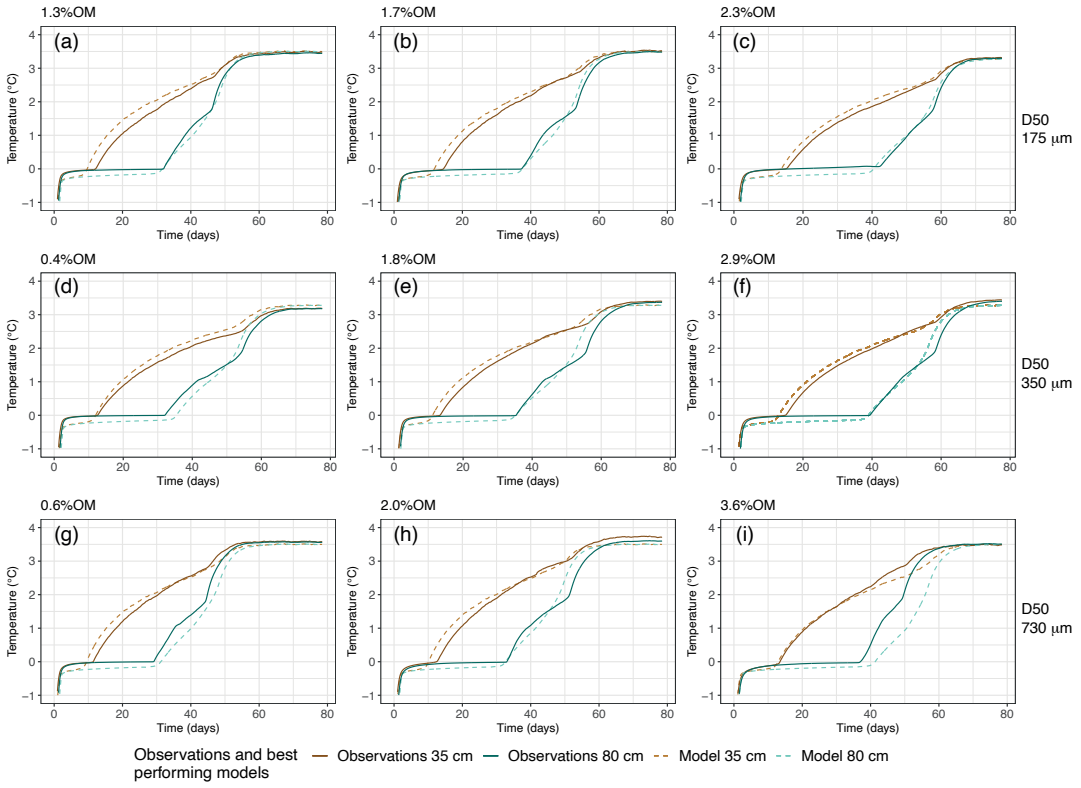

Figure 3.4 | Best KGE fit between observed and modelled data for the two sets of experiments during the thawing phase (III)

3.3.2 | Thermal properties

A numerical heat transfer model was run in two batches of 5544 models each. Resulting model temperature outputs have been analysed using the *KGE* error measure to determine the best fit with the 2 hours smoothed observed temperature data from the column experiments. Figure 3.4 shows the best fit between the observations and the optimized KGE model at a height of 0.35 and 0.80 m over the modelled thaw-cycle. Furthermore it shows how the thawing front propagates varying between the different experiments through the columns. The best fits represented by the dashed lines matches well with the observations in terms of temperature gradient over time, only panel (i) shows a lesser fit for the temperature recorded at a height of 0.8 m where the timing and gradient do not match. Panels (e, f and h) show that there are small misfits in terms of the timing of the thaw front that a certain temperature is reached between day 50 to 60.

Figure 3.5 shows the optimised values for the thermal conductivity, heat capacity and observed porosity determined by the numerical model and the organic matter content and grain size used during the experiments. There appears to be a decreasing trend in thermal conductivity with an increasing organic matter content. However, the thermal conductivity values with a D_{50} of 730 µm show an increase in thermal conductivity. There is no clear relation visible between the thermal conductivity and grain size. The optimised values for the heat capacity fluctuate over a small range of values at the lower end of the modelled parameter space, with one value peaking at a higher heat capacity of 650 (J/m^3K). There is no clear in- or decreasing trend visible for the heat capacity in relation to either organic matter content or grain size. The observed porosity clearly shows an increasing trend in porosity with an increasing organic matter content. The highest porosity values are observed in the experiments with the largest grain size with a D_{50} of 730 µm. The large grain size of D_{730} µm has the highest thermal conductivity and porosity, but does not appear to have an effect on the heat capacity.

3.3.3 | Porosity and Organic matter

Each soil column experiment has been sampled at four locations to determine the average porosity and organic matter content. Table 3.3 shows the averaged porosity and organic matter content for each experiment alongside the numerically derived optimised thermal properties. The measured porosity values are all in the same order of magnitude and range expected under experimental conditions. There appears to be a relation between the measured porosity and particle grain size as can be seen in Fig 3.5. The porosity increases parallel for the different grain sizes.

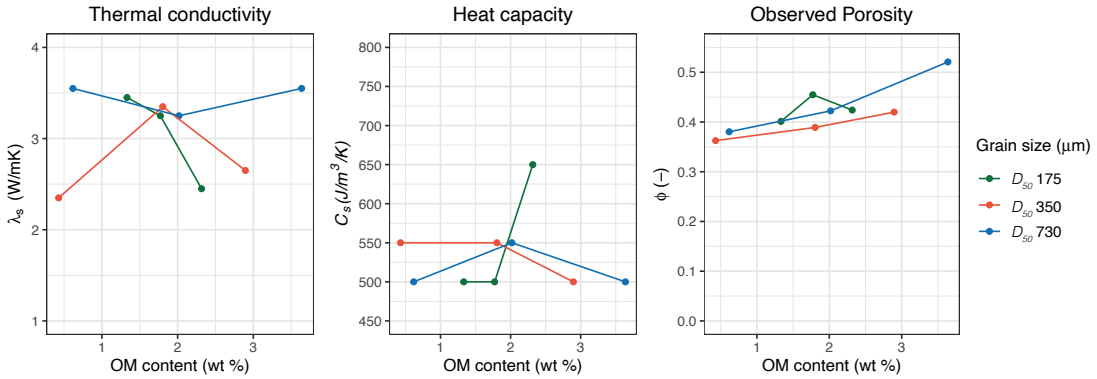

Figure 3.5 | Numerically determined optimised thermal property parameter values with the lowest *KGE* error set out against the measured organic matter content and porosity.

Table 3.3 | Numerically determined optimised thermal property parameter values with the lowest *KGE* error set out against the measured organic matter content and porosity

No.	Particle grain size D50 (µm)	Optimised thermal conductivity (λ_s) (W/mK)	Optimised heat capacity (C_s) (J/m^3K)	KGE	Organic matter content (wt %)	Observed porosity (ϕ) ($-$)
1	175	3.45	500	0.87	1.3	0.40
2	350	2.35	550	0.87	0.4	0.36
3	730	3.55	500	0.84	0.6	0.38
4	175	3.25	500	0.86	1.7	0.45
5	350	3.35	550	0.90	1.8	0.39
6	730	3.25	550	0.87	2.0	0.42
7	175	2.45	650	0.89	2.3	0.42
8	350	2.65	500	0.90	2.9	0.42
9	730	3.55	500	0.80	3.6	0.52

3.3.4 | Long-term model sensitivity

The nine optimised parameter combinations that best fit the observed data were used to model a hypothetical 100 year permafrost active layer thaw scenario. The results of the 100 year scenario highlights the long-term effect that different parameters have on permafrost thaw predictions. Figure 3.6 shows the interpolated active layer depths for the nine parameter combinations. During the initial 40 years, the active layer depth appears stable for all parameter combinations. However after 40 years, the active layer depth increases at different rates for the various parameter combinations. A time-lag appears for thaw depth for the different parameter combinations of 10 years at model year 70, and the timelag increases the following years. There is a spread in overall thawing depth after 100 years, ranging between 9 to 10 m. The parameter combinations with the largest timelag have the same value for the heat capacity (500 (J/m^3K)) and identical values for thermal conductivity (3.35 (W/mK)), but differ

for the porosity which ranges between 0.4 and 0.5 (-), indicating that the model is very sensitive to variations in porosity.

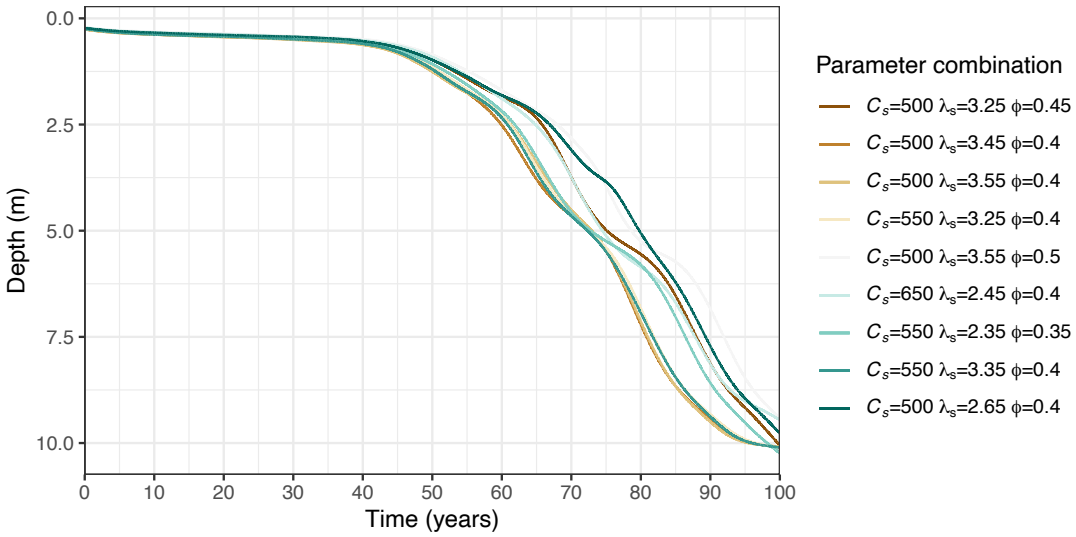

Figure 3.6 | Development of the active layer depth over a hypothetical 100 year model scenario for all nine optimised parameter combinations varying heat capacity C_s (J/m^3K), thermal conductivity λ_s (W/mK) and porosity (ϕ) $(-)$

3.4 | Discussion

3.4.1 | Temperature observations

The temperature observations collected during the nine experiments (Figure 3.3) illustrate clearly different freeze and thaw rates. This indicates that under near identical temperature and other experimental conditions, freeze and thaw rates are only influenced by the soil material and its thermal properties. Because the data is collected during two separate batches, small fluctuations in the air temperature make the temperature observations of both batches not directly comparable. Despite this fact, the usage of numerical modelling in both the vertical and radial direction allows us to use the observed air temperature as boundary condition and model the temperature development using a range of thermal properties.

A crucial aspect of this research is the timing of the thaw events of all nine experiments. The delay in timing is a primary result of the difference in thermal properties. Figure 3.4 shows the difference in timing of the various temperature observations, which only differs a few days between the nine experiments. This is, considering the timescale of thawing processes ($\sim$ 70 days), a negligible difference. However, this difference in timing took place under a step temperature increase from -3 to +3°C. Under field conditions the air temperature transition will be less abrupt, which will increase

the delay in timing between the modelled temperatures at the various depths. This is clearly visible in the 100 year future scenario (Figure 3.6), where the delay in timing is not in the order of days but up to 10 years.

3.4.2 | Optimised thermal properties

The numerically determined thermal properties do not all show clear trends in relation to the organic matter content or grain size (Figure 3.5). In the introduction, our hypothesis is that the thermal conductivity of the solid fraction would decrease with a higher organic matter content. This is due to the relative lower thermal conductivity of organic matter compared to plain sand. The numerically determined results show that there is indeed a decreasing trend in thermal conductivity with an increasing organic matter content. However the trend is not very clear as the optimised values are scattered over a large range. Similarly we would expect that the heat capacity increases with an increase in organic matter content due to the organic materials ability to absorb more energy per weight unit compared to quartsite sand. However the optimised model results show little variations in optimal values and no clear in- or decreasing trends. Next to that, the optimised heat capacity values are near the lower edge of the investigated parameter space with realistic values. de Bruin et al. (2021) showed that the heat capacity is a very insensitive model parameter compared to the thermal conductivity and porosity. Therefore, it is more difficult to numerically determine the optimum heat capacity, since variations in heat capacity only have a very limited effect on the temperature propagation. The observed porosity values shows that porosity increases with organic matter content. As a result, there is a higher water content within the sample which in turn increases the bulk thermal conductivity. The optimized parameter combinations determined using the KGE do somewhat coincide with the expected trends, but not convincingly. We have determined multiple factors that contribute to this. First of all, the sensitivity of the parameters varies greatly. In Chapter 2 we found that temperature is very insensitive to heat capacity variations, and thus difficult to determine accurately. The thermal conductivity and porosity are more sensitive and greatly affect temperature propagation. However, due to the dependency of thermal conductivity to porosity, there are multiple parameter combinations over a wide range that yield good model fits. Secondly, the optimisation process used in this study uses a full 3D parameter space which is evaluated using the KGE. This is based upon the concept that if there are multiple optimal parameter combinations possible, all possible combinations are explored. This is especially the case for correlated parameters. The limitation however is that multiple parameter combinations have good performing KGE fits, but the KGE only evaluates the error between model and observation for each time step, but the timing between model and observation is also crucial. Because we evaluate the average KGE, the average

KGE could be high, but there might still be a misfit in terms of timing between the model and observation at certain depths, as for example can be seen in Fig 3.4(i). The optimisation could be refined by taking a second error measure, such as the Russell's error (Russell, 1997) that evaluates the best fit between a model and observation based upon the time phase shift between the two signals (Chapter 2). Thereby evaluating the temperature values between model and observation using the KGE, and thereafter evaluate the timing of the phase shift between the model and observation.

3.4.3 | Long-term effects of parameter variation on active layer depth

The temperature observations gathered during the experiments show only relatively small differences in temperature propagation and timing of the freezing and thawing front. However, the subsequent implementation of the optimised parameter values derived from the experiments into the hypothetical 100 year active layer model reveal significant variations in thawing depth and timing over a long timescale. During the initial 40 model years, active layer depth remains similar for all parameter combinations, as is shown in Figure 3.6. After 40 years the active layer depth starts to develop at different rates. The two parameter combinations that are spaced apart furthest have heat capacity values which are very similar to each other; 500 and 550 (J/m^3K). The thermal conductivity and porosity values however vary. The spread in thermal conductivity along with porosity, are the primary contributors to the large spread in overall active layer thawing depth. This spread is clearly visible at for example model year 80, where the thawing depth between the two most outer model predictions varies between 5 and 7.5 m, which is a difference of 2.5 m.

The optimised parameter space appears to be quite 'flat' when trying to determine the best fit for the experiments. There are multiple combinations that vary only slightly in their KGE performance. Based upon the subsequent 100 year future scenario we determined that the heat capacity has a low impact and thermal conductivity in combination with the porosity has a high impact on permafrost development on the long term.

The 100 year scenario in Figure 3.6 highlights the implications of various thermal properties on the thermal development of the active layer, where especially the timing of thawing varies by over 10 years. In the 100-year scenario, the variation in timing impacts the permafrost environment on a larger scale as well (data not shown). Due to the increasing thawing depth of the active layer, a perennial thaw zone or intra-permafrost talik forms underneath the active layer (Walvoord et al., 2019). This would allow over time for advective heat transport to start next to conductive heat transport due to the activation of groundwater flow, potentially accelerating the development

of taliks and ponds (Rowland et al., 2011; Sjöberg et al., 2016; McKenzie & Voss, 2013). This in turn creates new pathways for dissolved organic carbon stored in the permafrost to be transported to the surface where it can be decomposed and emitted as CO_2 and CH_4 (Ma et al., 2019; Turetsky et al., 2020).

3.4.4 | Comparison of laboratory experiment with field observations

One of the main concerns with laboratory column experiments is the translation of laboratory scale processes to field scale processes, and the direct comparison of thermal properties found in the lab versus in the field. An important element of this translation is the SFCC, which is the curve that separates the solid and liquid ice fraction in the soil as a function of temperature (McKenzie et al., 2007; Grenier et al., 2018; Kurylyk & Watanabe, 2013). However, these curves vary for different soils and especially for experimentally packed soils in the lab (Devoie et al., 2022). To overcome this issue, we used a fixed SFCC that was adjusted to the observed lab data and subsequently applied during numerical modelling. By taking a SFCC that fits to the lab data, the modelled temperature propagation and resulting thermal properties well represent the observations.

In Chapter 2, a SFCC was used that was calibrated to the observed temperatures at the Quinghai-Tibetan Plateau (QTP). Because in both cases the SFCC are adjusted to the specific conditions, the modelled temperatures fit to the observed temperatures. The resulting thermal properties found in both studies are therefore not impacted by a discrepancy caused by a mismatch in SFCC, and can therefore be compared independently of the SFCC.

Regarding the sensitivity, we found in Chapter 2 similar results for model sensitivity to thermal properties. The optimised parameter values found in their study were based upon temperature observations from one location at the QTP. The study found optimal parameter ranges for thermal conductivity (λ_s) of 0.95 to 1.1 (W/mK), optimised heat capacity (C_s) of 875 to 1125 (J/m^3K) and optimised porosity (ϕ) of 0.25 to 0.45 $(-)$. In this study we used nine temperature datasets instead of one. The optimal values found in Chapter 2 differ with optimal values found in this study for fine grained sand with low organic matter content. This study found a higher λ_s ranging from of 2.45 to 3.55 (W/mK) and lower C_s varying between 500 and 650 (J/m^3K). The main reason for this difference is the high porosity in this study compared to Chapter 2, affecting the optimised thermal conductivity. Site information of the QTP indicates silty sand soil with organic rich topsoil (Luo et al., 2018b), which is in correspondence with the fine grained sand.

Permafrost is subjected to increasing air temperatures, where the thermal properties

highly influence the freezing and thawing rates as can be seen in the 100 year scenario (Figure 3.6). Our results indicate a relation between thermal conductivity and organic matter content, where the thermal conductivity decreases with increasing organic matter content. This could imply that permafrost areas with a high organic matter content are thermally less conductive, compared to soils with a low carbon content, which would result in lower thawing rates for soils with a high organic matter content. However, caution should be taken when experimental results are translated to possible implications in the field, as the experiments only focus on a very specific conditions. The organic matter content range investigated in this study (0 to 4 $wt\%$)is too limited to be able to extend this relationship to soils with higher organic matter contents. Despite this, large parts of mostly Yedoma permafrost areas contain low organic matter contents (Strauss et al., 2012). Future numerical permafrost modelling could focus on long-term effects of permafrost thaw in these Yedoma areas using the range in thermal properties found in this study. Especially the formation of perennial thaw zones (as was detected in the the 100-year scenario) indicates the reactivation of groundwater flows and associates dissolved carbons (Walvoord & Striegl, 2021). The variations in thermal properties affects the timing of the emergence of these groundwater flows. The timing is especially of importance since groundwater transports dissolved organic carbon that later on can be releases as greenhouse gases CO_2 and CH_4 into the atmosphere.

3.5 | Conclusion

In this study we used laboratory soil column experiments as a method to investigate freeze and thaw processes around the 0°C temperature range. Various soil grain sizes and organic matter contents produced significant differences in temperature propagation, indicating variations in effective soil thermal properties. With the help of batch numerical modelling, the temperature evolution of the column experiments was modelled and fitting parameter values were quantified. The optimised parameters all fall within the range of realistic values. The thermal conductivity and porosity were coupled parameters when evaluating the bulk thermal properties, and can not be evaluated separately. The heat capacity was on the other hand an insensitive parameter compared to the thermal conductivity, making it difficult to accurately determine the precise value. Long-term model results of active layer development showed a time-lag of over 10 years between different models. Furthermore the overall thawing depth varied over 2.5 meters at certain points during modelling. Both the time-lag and thawing depth were the result of variations in thermal conductivity and the porosity. This indicated that these thermal properties were essential for long term predictions and the associated timing of thawing events, and that it is thus

crucial to consider the porosity and thermal conductivity. To conclude on the main research question, we were able to quantify the thermal properties of column experiments with various organic matter contents and grain sizes. Thermal conductivity appears to decrease with an increase in organic matter content, however there is still a high degree of uncertainty as only small organic matter contents were evaluated. Variations in heat capacity were not directly relatable to either soil grain size or organic matter content. This research demonstrated that we can simulate permafrost freeze-thaw dynamics in a laboratory setting, but need to consider the limitations regarding a direct comparison between laboratory and field data. Numerical models simulating permafrost freeze-thaw dynamics help to bridge the gap between the laboratory and the field and allow for comparison of permafrost thermal properties. Relations between thermal properties and soil physical properties helps to increase our understanding of permafrost dynamics and future geohydrological conditions in cold climate regions. Which is especially needed in a warming climate, where the size and timing of new emerging carbon fluxes from permafrost areas provides useful insights as it impacts the ecology and society.

4

Tracking a freeze-thaw front using Electrical Resistivity Tomography

This chapter is based on work submitted to:

de Bruin, J. G. H., Bense, V. F., van der Ploeg, M. J., Binley, A., (2024). Large scale column experiment using 3D time-lapse electrical resistivity tomography (ERT) to investigate the permafrost freeze-thaw front, *Submitted to Geophysical Research Letters*

Abstract

Permafrost freeze-thaw transitions mark the critical zone between frozen stable and thawed unstable permafrost, affecting the hydrogeological functioning by (re)activating groundwater flows and decreasing the stability for infrastructure. There are still uncertainties in the transitional zone regarding liquid porewater fraction and the thermal properties. We used a column experiment resembling field conditions to study the freeze-thaw transitions, using 3D time-lapse Electrical Resistivity Tomography (ERT) and temperature observations. A clear transitional freeze-thaw front was detected by temperature and 3D resistivity observations. Resistivity and its distribution increased under ≤ 0°C temperatures. The setup allowed us to detect the transition in the liquid porewater fraction during freezing and thawing. Additionally, a hysteresis pattern was observed in the liquid water content during freezing and thawing. Applying the temperature-resistivity correction to time-lapse observations enables tracking variations in soil moisture or liquid water content, however it is ineffective for singe observations due to increased resistivity uncertainty.

4.1 | Introduction

Permafrost regions are subject to increasingly higher air temperatures, causing a deepening of the permafrost active layer (Biskaborn et al., 2019). Consequently, the cold regions hydrological system will become activated from the dormant state it is in during full permafrost conditions, and new and deeper groundwater circulation will likely ensue (Walvoord & Kurylyk, 2016; Sun et al., 2020a; Bense et al., 2009). This impacts not only the local hydrogeological conditions, but also destabilises human-made infrastructures (Ran et al., 2021).

In order to accurately predict permafrost thaw and ultimately hydrological and ecological responses to warming, the freeze-thaw processes need to be well understood. Central to the dynamics of thawing permafrost in a warming climate is the phase change transition of water, where pore water freezes and thaws, as it is the transitional zone between a frozen stable and thawed dynamic state. Conventional permafrost monitoring methods such as temperature observations are point observations, and require great effort to install. Electrical Resistivity Tomography (ERT) observations are increasingly being used as a flexible and non-invasive method to study these transient subsurface processes (Oldenborger & LeBlanc, 2018; French et al., 2002; Bloem et al., 2020; Krautblatter et al., 2010).

ERT is a widely applied geophysical method that uses electrical resistance observations to delineate subsurface characteristics which are used to construct subsurface cross-sections over large transects (Binley & Slater, 2020; Herring et al., 2023). Subsurface features such as layering of soil/rock types, pore space, pore fluid ionic content, water content and temperature influence the electrical resistivity. Cold regions ERT is used to monitor various environmental processes related to hydrogeology, with a special emphasis on freeze and thaw transitions. For example, time-lapse ERT measurements have been used to monitor the frozen ground evolution during surface snow melt (Hauck, 2002; Hilbich et al., 2011; French & Binley, 2004; Bloem et al., 2020; Scherler et al., 2010). Likewise, they have been used to investigate permafrost active-layer dynamics and degradation over time (Kneisel et al., 2014; Buckel et al., 2023; Tomaškovičová & Ingeman-Nielsen, 2023; Farzamian et al., 2020).

The relation between temperature and water resistivity is well understood at $\geq$0°C temperatures (Frohlich & Parke, 1989). As temperature increases, water viscosity decreases, which increases the mobility of water ions, thereby decreasing the electrical resistivity (Hauck, 2002; Herring et al., 2019). Methods have been developed to remove the effect of temperature variations at above 0°C temperatures from electrical resistivity observations (Hayashi, 2004; Hayley et al., 2007, 2010). However, temper-

ature correction in freezing soils is difficult due to the non-linear freezing process of porewater, which varies with dissolved solutes, fluid properties such as viscosity and soil characteristics such as texture and pore structure. (Hauck, 2002; Herring et al., 2019; Oldenborger, 2021; Lyu et al., 2019). During freezing, the unfrozen porewater fraction decreases, thereby reducing the ionic mobility and thus the conduction pathways. As a result of the decrease in conduction pathways, the fluid electrical resistivity increases sharply during freezing (Herring et al., 2021; Kang & Lee, 2015; Tang et al., 2020; Hayley et al., 2010).

Additionally, porewater freezing and thawing shows hysteresis, complicating temperature-correcting resistivity observations (Tian et al., 2014; Saberi & Meschke, 2021; Pardo Lara et al., 2021; Tomaškovičová & Ingeman-Nielsen, 2023). The hysteresis is caused by a difference in the liquid pore water fraction between the freezing and thawing interval at a specific temperature. There are multiple processes causing the difference in liquid pore water. One key process is the nucleation of ice during initial freezing, which is a metastable process that depresses the porewater freezing point and thereby causes a delay in freezing. Additionally, supercooling during freezing is also contributing to hysteresis effects, by temporarily decreasing the temperature whilst maintaining liquid pore water (Tian et al., 2014; Zhang et al., 2020; Wu et al., 2017; Kozlowski, 2009).

Small-scale laboratory setups have been used to study the influence of freeze-thaw transitions on soil electrical resistivity. These typically consist of a small sample equipped, with four electrodes, which is subjected to freezing and thawing conditions (Tang et al., 2020; Liu et al., 2022). A limitation of these small-scale experiments is the non-representativeness compared to field observations. This is because the small-scale experiments rely on single point resistivity observations, in essence 0D, assuming homogeneous conditions, thereby lacking spatial variation in the data that would be observe in the field. Large scale column or tank experiments are potentially better able to represent field scale dynamics as they include heterogeneous conditions and are therefore often used in combination with 3D ERT observations (Koestel et al., 2009). They allow the collection of detailed 3D cross-sections of the soil column without invasive sampling (Binley et al., 1996; Koestel et al., 2009). Due to the heterogeneous nature and large sample volume of large-scale column experiments, the distribution of the resistivity observations better reflects distributions you would observe in the field. Therefore, ERT column and tank experiments have been widely applied to study solute transport, track tracer fluids and preferential flows (Slater et al., 2002; Koestel et al., 2008; Fernandez et al., 2019; Bechtold et al., 2012; Garré et al., 2010, 2011). So far, large-scale column experiments using 3D ERT observations have not been combined with freeze-thaw experiments.

In order to track the development of permafrost active-layer freeze-thaw fronts using ERT observations, it is thus essential that the effect of temperature on the resistivity and link between resistivity and the boundary of the freeze-thaw front are clearly defined at realistic scales representing field conditions. Additionally, the total resistivity range due to spatial variability during ≤0°C temperatures is still unknown, as this is not observed in single laboratory observations.

In this chapter we use 3D time-lapse ERT observations collected in a column experiment which was subjected to a freeze-thaw cycle. The aim of this chapter was to (i) track the thawing front through the soil column using time-lapse ERT and temperature observations; (ii) determine bulk resistivity at various stages during freezing and thawing; (iii) validate current temperature–resistivity relations for partly frozen soils; (iv) determine the resistivity distribution during freezing and thawing. This would allow to fill the current knowledge gap on the relation between temperature and resistivity and uncertainty in resistivity distribution around the freeze-thaw transition (Tomaškovičová & Ingeman-Nielsen, 2023).

4.2 | Methods

4.2.1 | Experimental data collection

4.2.1.1 | Soil column setup

The laboratory experiment was conducted using a column that contained the sample, made out of a 1.2 m tall High Density Poly Ethylene (HDPE) material with an inner diameter of 0.328 m and wall thickness of 36 mm (Figure 4.1a). The column was closed of at the bottom using a detachable 20 mm thick aluminum plate and rubber ring to create a watertight seal. The aluminum plate was covered with a thin rubber membrane, which allows for heat conduction into the sample, but electrically isolates the sample from the aluminum plate (Figure 4.1c,d).

A tried and tested vertical 1D heat transfer setup was created mimicking field conditions (Chapter 3). In the field, the primary heat exchange interaction takes place at the soil surface, propagating vertically downward. In order to recreate these one directional heat flow conditions, the column was fully insulated around the sides and the top with 0.12 m thick rockwool shell insulation, thereby limiting lateral heat flow, with only the bottom of the column exposed to the air temperature.

The temperature inside the column was monitored using seven T107 (Campbell Sci.) temperature sensors, and two further temperature sensors were placed in the climate chamber to measure the air temperature. The sensors have an operating range from

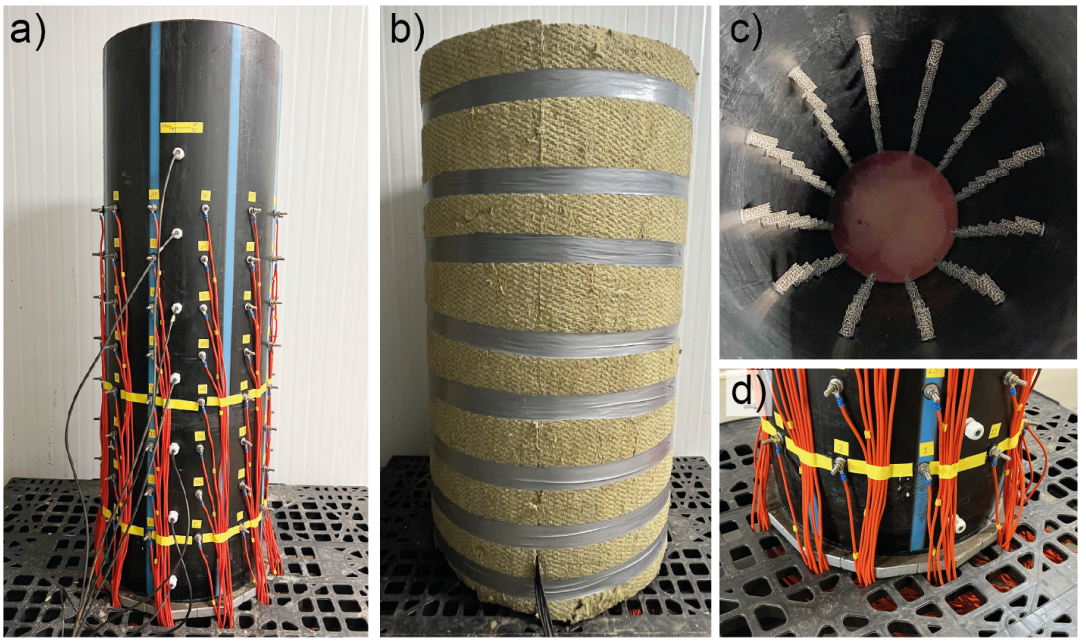

Figure 4.1 | (a) 1.2 meter high HDPE column equipped with 96 stainless steel electrodes connected with orange cables to the ERT switch box and black cables to the temperature sensors. (b) HDPE column fitted with 0.12 meter thick shell insulation on the sides and top. (c) Inside of HDPE column with wire-mesh stainless steel electrodes. (d) Bottom aluminum base plate.

-35 to 50°C and are calibrated to an accuracy of 0.01°C. The temperature sensors were placed at different heights in the sample both within the same horizontal plane as the ERT electrodes, as well as in between the ERT electrode planes (for details see Appendix C.1). In order to prevent creating paths of least resistance for currents during the ERT measurements, the temperature sensors were encapsulated in a thin heat-shrunk plastic sleeve.

For the ERT measurements, the HDPE column was equipped with 96 stainless steel electrodes. The electrodes were placed in eight horizontal rings of twelve electrodes each around the circumference of the column at heights starting with 0.15 m to 0.85 m at a 0.1 m spacing from the bottom. The electrodes were embedded 25 mm deep into the sample and consisted out of a 5 mm thick stainless steel rod of which the tip was wound with a metal wire mesh to maintain good electrical contact with the soil material during soil expansion and shrinkage to prevent high contact resistances (Tomaškovičová et al., 2016; Clement & Moreau, 2016).

The sample consisted of quartsite sand with grain size distribution between 200-500 μm with a D_{50} of 350 μm and peat organic matter content of 5 wt%. The sample was fully saturated with tap water, which had an electrical conductivity of 84 μS cm^{-1}, in order to create homogeneous saturation conditions throughout the sample.

The column was filled up to 1 m using the slurry packing method including manual compaction (Lewis & Sjöstrom, 2010). On top of the sample, a 0.1 m layer of water was added that created a top boundary with known thermal properties. Porosity of the sample was determined at the end of the experiment by collecting six 100 cc sample ring at heights of 0.5 and 0.8 m within the column, organic matter content was determined using the loss on ignition (LOI) technique (Heiri et al., 2001).

4.2.1.2 | Boundary conditions

The experimental setup was placed within a climate chamber, where the temperature can be controlled between 20 to -5°C. Initial air temperature was set to 3°C and the soil column was not insulated. Once the stabilisation period was complete and a homogeneous temperature distribution was reached within the column, the column was encapsulated in the insulation shell. Thereafter, the temperature was lowered in one step to -4°C. The freezing process continued for a period of 8 weeks, after which the column was fully frozen. During the freezing process, temperatures in the climate chamber jumped periodically to above zero temperatures for a very short period. This was to ensure that the freezer unit remains clear of any ice buildup. Once the column was fully homogeneously frozen, the temperature in the climate chamber was increased in one step to 5.5°C, and a thawing front formed that propagated vertically upward through the column.

4.2.1.3 | Data Acquisition

Temperature observations were logged on a data logger (Campbell Sci.) at a five minute interval, which were on separate electrical circuits from the ERT logger to prevent short circuits currents from interfering Koestel et al. (2008).

ERT observations were collected using a Iris Instruments Syscal Pro and 96 electrodes (Truffert, 2022). A custom sequence was made that allowed tracking off the freeze and thaw front with a high accuracy in the horizontal and vertical plane. In order to ensure a high spatial distribution in the sample with good signal-to-noise ratio, we used a circulating scheme consisting of horizontal dipole-dipole, skip 1, skip 2, vertical dipole-dipole and diagonal dipole-dipole, resulting in 2367 quadrupoles (Slater et al., 2000, 2002; Binley, 2015). For data inversion, only all horizontal quadrupoles (1919) were used in order to avoid asymmetrical sensitivity of the ERT measurements. To improve the quality of the observations, each quadrupole combination was stacked up to 10 times to obtain a quality factor lower than 3% (standard deviation of measurement) For all quadrupoles, the reciprocals were also observed. Reciprocal errors were used to evaluate the data quality during the experiment, and define the error model parameters used during the inversion process. Injection voltage was set at 25V.

Due to the dependence of soil resistivity on temperature, an interval for ERT observations was selected that covers the temporal variability of the thawing process. The thaw front propagated with an expected rate of 0.03 m/day through the column as the porewater changes state. Based upon this propagation speed, and a vertical spacing of 0.1 m between the electrodes the ERT time-lapse observations were performed on a roughly five-day interval, ensuring that the thaw front propagation was well captured as it passed the electrodes.

4.2.2 | ERT processing and inversion

For the inversion of the raw resistivity data, we used the R3t inversion code (Binley & Slater, 2020), which determines the smoothest distribution of electrical resistivity that best fit the ERT-observations.

Prior to inversion, the raw ERT observations were pre-processed to filter out all outliers. We determined the noise in the data using reciprocal measurements collected during each observation. For this we used the mean absolute transfer resistance $|R|$ [Ω] described as

$$|R| = \frac{||R_f| + |R_r||}{2} \tag{4.1}$$

and absolute error $|e|$ [Ω] as

$$|e| = ||R_f| - |R_r|| \tag{4.2}$$

We created a 3D tetrahedral elements mesh of the column and individual electrodes using Gmsh (Geuzaine & Remacle, 2009). A group of very small elements were embedded in the mesh to represent the non-point electrodes. The electrode volumes were assigned a fixed pre-defined resistivity of 0.00001 Ωm, as these are highly conductive and should not vary during the inversion (see Appendix C.8).

All datasets of the thawing phase were inverted using a time-lapse inversion scheme (Binley & Slater, 2020). To perform the time-lapse inversion we collected three ERT datasets before the freezing process at a stable temperature of 3°C, that were averaged to create a reference dataset. This reference dataset was subsequently used to create a reference resistivity model for the inversion of the remaining time-lapse datasets. During the inversion, the difference between the reference and time-lapse datasets was determined. This process highlights resistivity evolution over time.

The inversion software determined the smoothest distribution of electrical conductivity that best fit the observations using a linear error model as constraint. We used a fixed error level for all inversions, representing the error measured both during freezing and thawing conditions. The errors can be random measurement noise or

systematic, e.g. due to changes in electrode contact resistance. We describe the standard deviation of the mean transfer resistance (R) using the two parameters a_{weight} and b_{weight} as

$$\sigma(R) = \sqrt{a_{weight}^2 + b_{weight}^2 * R^2} \tag{4.3}$$

We followed the method by Koestel et al. (2008); LaBrecque et al. (1996) to process the data to determine the error model parameters (a_{weight} and b_{weight}). All transfer resistances (R) were divided over equally sized bins on a logarithmic scale. Next, the standard deviation of the mean transfer resistances of each bin was calculated ($\sigma(R)$) (Appendix C.3 to C.6). We calculated a single a_{weight} and b_{weight} that fitted the error data of all time-lapse observations (Appendix C.7). The single values for the a_{weight} and b_{weight} are set in the R3t inversion software, that subsequently used the computed errors to allow the assignment of weights for each measurement.

4.2.3 | Temperature-resistivity relation

4.2.3.1 | Temperature-resistivity relation for unfrozen water

We used a temperature-dependent resistivity function to determine the bulk resistivity while accounting for the freezing and thawing of the soil. The basic function for calculating temperature dependent bulk resistivity at ≥0°C is represented by

$$\rho_{bulk} = a\phi^{-m} S_w^{-n} \rho_f \tag{4.4}$$

which is a modified version of Archie's equation, empirically describing bulk resistivity for clay-free material (Winsauer et al., 1952; Hauck, 2002; Herring et al., 2019).

The bulk resistivity ρ_{bulk} [Ωm] is calculated using the physical properties; porosity ϕ [m^3m^{-3}], water saturation S_w [m^3m^{-3}] and fluid resistivity ρ_f [Ωm]. Additionally, m represents the cementation exponent, n is the saturation exponent and the empirical unitless fitting parameter a that represents the tortuosity factor. The inclusion of the tortuosity factor is in essence a non-unity value that helps to fit the curve to the data by compensating for systematic errors in porosity, temperature and fluid salinity. Careful consideration should be taken when using the the tortuosity factor, where a value closer to unity is most favorable (Herring et al., 2019; Binley & Slater, 2020; Glover, 2016).

Temperature dependent fluid resistivity for above 0°C is described as

$$\rho_f = \rho_{f_ref} \frac{1}{d(T - T_{ref}) + 1} \tag{4.5}$$

where ρ_f [Ωm] represents the fluid resistivity, ρ_{f_ref} [Ωm] the resistivity of a fluid at a reference temperature T_{ref} [°C], usually 25°C, and d [°C^{-1}] is a constant temperature compensation factor (Hayashi, 2004).

4.2.3.2 | Temperature-resistivity relation frozen water

In order to determine the bulk resistivity for ≤0°C temperatures, the liquid resistivity needs to be compensated for i) temperature and ii) the decrease in water saturation. To account for the decrease in saturation, the relative saturation term S_r is introduced

$$S_r = \frac{S_{wL}}{S_{w0}} \tag{4.6}$$

The relative saturation is determined using the empirical Soil Freezing Characteristics Curve (SFCC), that describes pore water saturation for various soil types during freezing (Ren et al., 2017; Devoie et al., 2022). The SFCC uses a temperature-dependent liquid saturation level S_{wl} and the initial saturation level S_{w0}.

As porewater freezes, the relative saturation decreases, causing ions to exclude into the remaining liquid porewater, increasing the solute concentration. The increase in dissolved solutes concentration decreases the resistivity of the remaining unfrozen porewater. In order to incorporate the relation between solute concentration, temperature and the effect on the electrical resistivity, we used the relation for NaCl

$$\rho_{f_25} = (kC)^{-1} \tag{4.7}$$

under the assumption that it applies also for tap water (Herring et al., 2019).

The liquid water concentration C [gL^{-1}]

$$C = \frac{C_0}{S_r} \tag{4.8}$$

varies based upon the fraction of the initial porewater concentration C_0 [gL^{-1}] and the relative saturation level S_r. The liquid water concentration C varies with temperature and varies only during the freezing and thawing phase as it is linked to the SFCC curve.

Equations 4.7 and 4.8 are combined into

$$\rho_{f_25} = \frac{S_r}{kC_0} \tag{4.9}$$

effectively replacing ρ_{f_ref} by a function that accounts for an in-or decrease in fluid resistivity due to the variations in dissolved solid concentration during freezing.

Combining Archie's law (Equation 4.4) with temperature variable fluid resistivity (Equation 4.5), yields

$$\rho_{bulk} = \begin{cases} a\phi^{-m} S_{w0}^{-n} \dfrac{1}{kC_0(d(T - T_{ref}) + 1)} & \text{if } T > 0\ °C, \\ a\phi^{-m} (S_r S_{w0})^{-n} \dfrac{S_r}{kC_0(d(T - T_{ref}) + 1)} & \text{if } T < 0\ °C \end{cases} \tag{4.10}$$

where at above 0°C temperatures the relative saturation is equal to 1 due to the absence of ice. All parameter values can be found in the Appendix Table C.1.

4.3 | Results

4.3.1 | Temperature observations

Figure 4.2a shows the temperature timeseries for different heights within the column over the freezing and thawing interval. From day 0 to 45, temperature inside the column dropped from +4 to -3.5°C. Our observations started as the column was undergoing freezing, where unfortunately temperature data of the initial freezing phase was lost during collection as a result of a malfunctioning of the datalogger. Day 138 marked the onset of the thawing of the column, where the air temperature was increased from -3.5°C to 5.5°C and a thawing front started to propagate vertically upward through the column. As the temperature was increased, the entire column increased sharply to 0°C, and the porewater phase change started. Thawing started at the base, with a propagation speed of 0.04 m/day on average. The phase change had a total duration of 24 days, after which the entire column had a temperature ≥0°C.

4.3.2 | ERT time-lapse observations

A total of eighteen ERT observations have been collected during the freeze-thaw period. Figure 4.2b displays eight time-lapse inversions covering the thawing interval. The inversion results show the difference in resistivity compared to the fully thawed reference column. The dark blue squares mark the electrode positions that have a fixed resistivity in the inversion.

Inversion 9 (Figure 4.2b) shows the column fully frozen, as the air temperature had been increased. The resistivity spiked at $2.8 \cdot 10^4$ Ωm, and a zone of low resistivity developed at the base of the column. The resistivities for inversion 10 showed a significant decrease, and the thawing front is clearly defined by the blue-red transition in Figure 4.2b. The thawing front was at exactly the same height as the temperature sensor located at 0.2 m depth. Inversion 11 shows that the freezing front had propagated further upward. At this time, a low resistivity zone also appeared at the

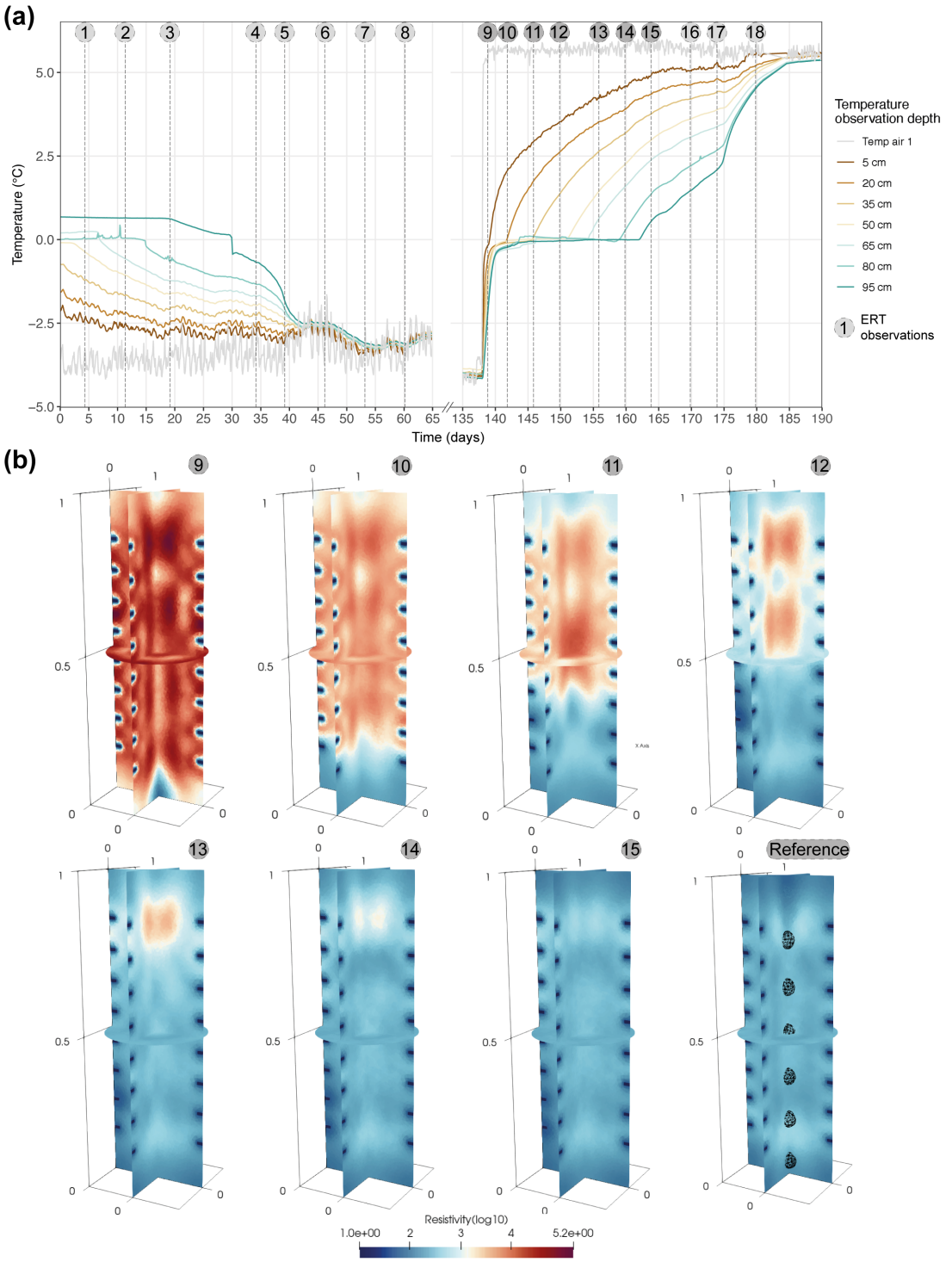

Figure 4.2 | a) Temperature observations at various depths within the ERT column, collected both during freezing (first 45 days) and thawing (starting at day 140), vertical lines indicate individual ERT observations. b) Time-lapse ERT inversions collected during the thawing interval at indicated time steps in panel a). The volume round each electrode had a fixed resistivity assigned to it to account for the non-point electrodes. The reference observation shows seven spheres, that represent the locations around the seven temperature sensors from where resistivity values are exported and used in Figure 4.3.

top of the column. This was likely the result of a small variation in resistivity at the top of the sample in combination with a low sensitivity above the top electrodes (Appendix C.8), that was subsequently over fitted in the inversion and appears as a low resistivity zone. Inversions 12 to 14 show the thaw front continued to move vertically through the column, and that the frozen high resistivity zone reduced in vertical extent and in diameter. In inversion 15, the high resistivity zone has disappeared. This matches the temperatures in the column as shown in Figure 4.2a that all exceed 0°C. Fully thawed resistivities were on average 284 Ωm.

4.3.3 | Temperature-Resistivity relation

Figure 4.3 shows resistivity values that were extracted from all twenty ERT inversions around the temperature sensors within a 0.05 m radius, plotted against the observed temperature at that sensor. The resistivities were grouped into bins of 0.5°C, of which the median resistivity was determined. The bins were split up into resistivity data gathered during the freezing process (ERT datasets 1 to 8), and during thawing (ERT datasets 9 to 18). The temperature-resistivity relation (Equation 4.10) was automatically fitted by optimizing the parameters, minimizing the root mean squared error of the temperature-resistivity relation against the group median resistivity values both during the freezing phase as well as the thawing phase (Appendix Table C.1).

The temperature-resistivity data clearly followed the expected pattern for frozen ground. Resistivity values at ≥0°C temperatures were nearly constant, whilst resistivity increased sharply during freezing. The boxplots have a wider confidence interval at ≤0°C temperatures compared to ≥0°C temperatures, indicating that the spread in observed resistivities is a lot higher. At -1.5°C the observed resistivity appeared to reach a level where it was less influenced by a further decrease in temperature. The two temperature-resistivity curves show that during freezing, resistivity increased at a lower temperature, compared to thawing when resistivities were significantly higher. At -1.5°C the median resistivity for both freezing and thawing were equal. This difference in resistivity during freezing and thawing was likely the result of hysteresis of the porewater saturation during the freeze-thaw process (Kang & Lee, 2015). The division of liquid and frozen porewater was calculated using the SFCC. In numerical models this is usually a fixed curve for both freezing and thawing, however the data show that the freezing phase follows a different curve compared to thawing (Devoie et al., 2022). The lower resitivities during freezing indicate that porewater remained liquid until temperature reached -1.5°C. During thawing, porewater remained frozen for a longer period of time.

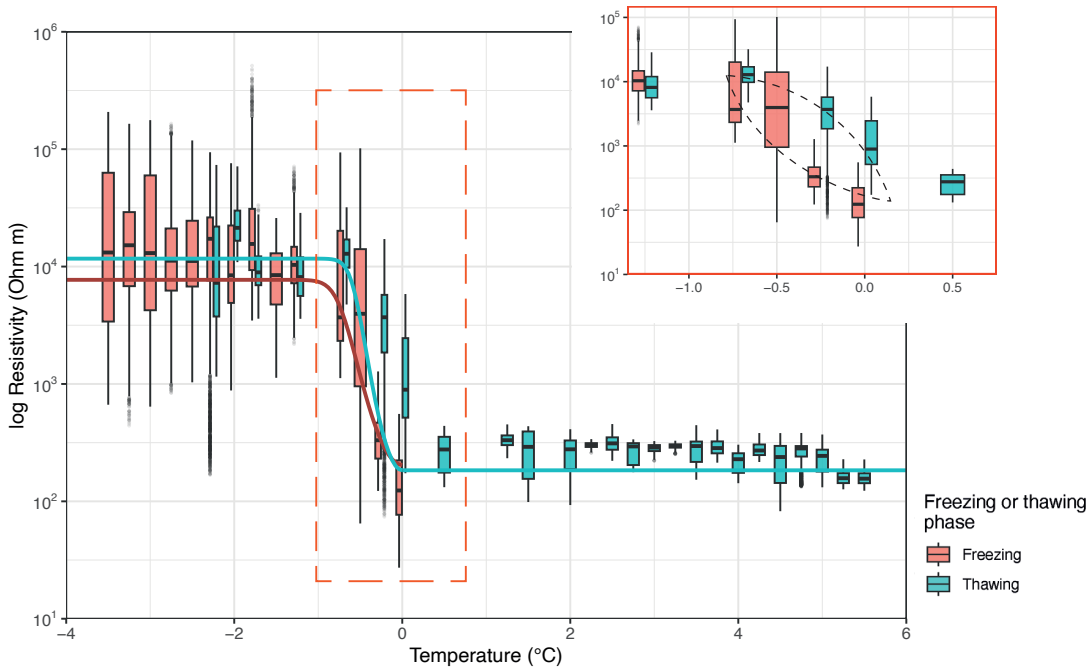

Figure 4.3 | Resistivity versus temperature binned in 0.5°C bins. Data is split between data collected during freezing and during thawing. Solid lines represent the best fit of the temperature-resistivity relation (Equation 4.10) fitted for both the freezing observations as well as the thawing observations. Highlighted is the observed resistivity hysteresis during the phase change interval.

4.4 | Discussion

The results from the experiment show that there was a strong agreement between the freeze-thaw front captured by the ERT inversions and the temperature observations. ERT observations in Figure 4.2b show the resistivity response to temperature increase, with a clear difference in resistivity between the -4 and 0°C datasets. The thaw front can be defined in multiple ways, either based upon a sharp resistivity transition or based upon a temperature threshold. The results show that the combination of both temperature and resistivity allowed us to detect two transitions related to the thaw front. First, is the decrease in saturation due to the porewater phase change, visible in the gradual decrease of resistivity. The second is the sharp decrease in resistivity coincides with the temperature exceeding 0°C, marking the end of the phase change and could be defined as the actual front. The inferred thaw front does not appear to be homogeneous in shape, but has an irregular pattern. Since the temperature thaw front propagates diffusely, we expected that the corresponding resistivity front would also be diffuse. However, the thaw front consists of a 'mushy zone' where the phase change occurs, this mushy zone might cause a less defined transition.

The inversion results in Figure 4.2b show resistivity variations in the fully frozen and

fully thawed state, despite the fact that the material consist of a well-mixed homogeneous material. The internal resistivity variations are visible at the same locations in all inversions. This suggests that it is caused by structural errors either part of the reference model, or sensitivity of the measurement scheme. We performed an analysis on the measurement scheme, and found that the diagonal and vertical quadrupoles cause sensitivity variations within the center of the column. This in turn leads to structural under and over fitting of resistivity in the inversion, causing these patterns. We subsequently removed all diagonal and vertical quadrupoles from the inversions, which reduced occurrence of these artifacts. The resistivity variations are the result of a lower sensitivity in the center of the column (Appendix C.8).

The binned resistivities in Figure 4.3 clearly show the increase in resistivity during freezing. In the bin located at 0°C, there is a clear difference in absolute and range of resistivity between the freezing and thawing observations. At -1.5°C resistivity values and spread stabilize and do not appear to increase for lower temperatures. This indicates that there are no visible variations in liquid porewater fraction that affect the resistivity below -1.5°C.

Figure 4.3 shows that there is hysteresis between freezing and thawing. The hysteresis effect has been observed during controlled small-scale experiments (Tian et al., 2014, 2018; Ren & Vanapalli, 2020; Wu et al., 2017; Kang & Lee, 2015), and is part of observed SFCC's (Saberi & Meschke, 2021; Pardo Lara et al., 2021; Devoie et al., 2022). Our results demonstrate that the hysteresis is also detectable during large-scale 3D experiments. Hysteresis complicates temperature correcting the resistivity observations, since the correction function differs for either freezing or thawing situations (Figure 4.3). We have automatically fitted two temperature-correction curves (Equation 4.10) to the resistivity observations. However, since the curves are based upon the empirical SFCC, we fitted the curves by changing the parameters that are unrelated to the physical processes that cause the hysteresis. The resulting curve fits are not ideal round the freeze-thaw interval due to the hysteresis. During fitting we varied the tortuosity factor a, starting with a ideal case where the value is closest to unity, yet this did not yield a good fit to the experimental data. Since the aim was to fit the curve to the data, we decided to go for the optimal value for the tortuosity factor, rather than the ideal unity case (Glover, 2016).

The experimental results show that resistivity can be used to detect the decrease/increase in liquid water content during freezing and thawing, even before it is detectable using temperature observations. This is because during the phase change, temperature remains 0°C while the liquid water content in or decreases (Tomaškovičová et al., 2016). The liquid water content is an important permafrost vari-

able, as it determines the bulk thermal properties during the dynamic phase change (Chapter 3)(Farouki, 1981), which in turn determines active layer freeze-thaw rates and thickness. The results show that it should be possible to detect the liquid pore-water fraction from time-lapse ERT field data gathered over the freeze-thaw cycles. This is based on the hypothesis that the $\geq$0°C resistivity values represent a fully thawed situation (100% liquid water) and the resistivity values at -1.5°C a fully frozen situation (0% liquid water), and that the increase/decrease in liquid water content follows the fitted temperature-resistivity curves for either freezing or thawing situations, however hysteresis is for now not yet numerically represented in this curve.

The 3D nature of the experimental setup shows the added value over single 0D freeze-thaw observations. Where 0D allows only to collect single observations, the 3D setup samples the whole volume better mimicking the effect of freezing and thawing on both short and long electrical flow paths. As a result, not only the increase in resistivity due to $\geq$0°C temperatures is visible, but also a significantly higher resistivity distribution is detected, as you realistically would expect from field data under freezing conditions.

Using the temperature-resistivity curve, it is possible to temperature-correct permafrost field ERT observations. However, the temperature correction would remove only the structural increase in resistivity during freezing, but it doesn't remove the increase in spread in resistivity. Due to the large spread, temperature-correcting a single $\leq$ 0°C ERT image would not provide accurate information on the resistivity and therefor soil characteristics. However, if you would temperature-correct multiple time-lapse observations, you would be able to evaluate the changes overtime between the two images independent from the increase in spread and be able to attribute variation to actual changes in soil state or for example moisture content and not to temperature variations.

4.5 | Conclusion

We have shown a laboratory large column setup to study permafrost freeze-thaw with ERT. This setup more closely resembles heterogeneous field conditions compared to small volume measurements. The results show that ERT-observations can be used to track a freeze-thaw front in a 3D experimental setup. A clearly defined resistivity front propagated through the setup as the column underwent a phase change transition and temperatures remained constant at 0°C. Analysis indicates that the temperature-resistivity relation fits well to the median of the ERT-observations collected during $\leq$0°C temperatures. The 3D nature of the experiment shows evidence

of a large distribution of resistivities at ≤0°C temperatures, whereas the distribution is smaller at ≥0°C temperatures. This large distribution is realistically what would be expected during frozen field conditions. The fitted curve shows it is possible to temperature-correct permafrost ERT observations collected in the field, however the uncertainties are significantly larger for frozen conditions, thereby decreasing the accuracy of ≤0°C ERT profiles. Therefore, temperature-correction of ≤ 0°C ERT observations would be more effective for time-lapse ERT observations compared to single observations, because it would allow to detect changes over time between images, caused by for example variations in moisture content or liquid water content, independent of the increase in resistivity uncertainty and without temperature induced resistivity variations.

The results show that ERT could also be used to determine the unfrozen water content during the freeze-thaw interval, which in turn is important for the bulk thermal properties. This information is very useful especially for numerical permafrost models, since the liquid water content has a large impact on the bulk thermal properties (Chapter 3). Most numerical models use a function to describe the liquid water fraction (SFCC), but with the help of ERT field observations, the actual values could be measured. This in turn allows numerical permafrost models to improve long-term permafrost freeze-thaw models, making more accurate and reliable predictions on permafrost stability and possible reactivation of groundwater flow.

The observed hysteresis in combination with the potential usage to detect the liquid water content would require additional investigation. This could be done using ERT lab experiment simulating multiple freeze-thaw and thus hysteresis events at lower temperature gradients, and simulate partial freeze-thaw events. These repeated freeze-thaw observations allow to determine the unfrozen water content at various stages during freezing and thawing. This would be especially relevant for vulnerable 'warm' permafrost that have relatively high temperatures, fluctuating around 0°C, thereby in a constant phase change state, switching between freezing and thawing (Zhao & Yang, 2022). Additionally, there is also hysteresis between resistivity and the unfrozen water content (Tomaškovičová & Ingeman-Nielsen, 2023), which would require further investigation. Overall, permafrost phase change dynamics encompass a large variety of feedback and hysteresis that are of vital importance to understand the dynamical behavior of future permafrost in an increasingly warming climate.

5

Synthesis

5.1 | Synthesis

Due to a changing permafrost environment, many hydrogeological processes and associated feedbacks reactivate and intensify (Figure 1.5). In order to make predictions on the scale and timing of these processes, accurate numerical heat transfer models that include intricate freeze-thaw processes, alongside with novel detection techniques are necessary. Especially the parameterisation of the thermal properties and porosity is of importance yet difficult, due to the absence of data. That is why in this thesis, we discuss how with the help of temperature observations, permafrost thermal properties can be derived. Furthermore, we demonstrate how we can improve our observational capability of permafrost with the use of temperature-corrected time-lapse ERT observations. In this chapter I provide a synthesis of the main findings of this thesis, answering the research questions posed in the introduction. Furthermore, I discuss the conclusions considering the limitations and highlight future opportunities for permafrost research.

5.1.1 | Main findings

Permafrost thermal properties at specific field sites are often unknown. This hampers our ability to numerically model and simulate temperature dynamics of these systems. In Chapter 2, I used a basic 1D numerical heat transport model in combination with solely temperature observations as model input to delineate the thermal properties of the subsurface. It was found that the parameter space comprising out of the thermal conductivity, heat capacity and porosity contained a number of varying parameter combinations that all yielded good model performance. A parameter optimisation algorithm reviewing a single parameter at the time could have resulted in finding only one single optimal parameter combination, a local minimum, ignoring the other possible parameter combinations. This highlighted the non-linear relations between the parameters. An investigation of the full parameter space therefore ensures determining the unique parameter combination representing the global minimum with the lowest error. The thermal conductivity was found to be the most sensitive parameter, thereby being the most important controlling factor on heat propagation.

Model and observation fit were evaluated using three different methods, evaluating the misfit in terms of magnitude, timing and a combination of both. Significantly different optimal parameter combinations were found, based upon the three different independent error methods. Marking the importance of the modellers choices for specific error models and the influence it has on a seemingly autonomous fitting procedure. The different optimal parameter combinations yielded significantly varying model results in active layer thaw depth over a 100-year future climate scen-

ario. Overall uncertainty of a parameter is therefore the product of the sensitivity of the parameter itself, in combination with an added sensitivity as a result of the ambiguous fitting procedure.

To determine the effect of various soil properties on the thermal properties and subsequent propagation of heat, we simulated freezing and thawing using various column experiments. In Chapter 3, temperature observations collected using nine column freeze-thaw experiments were used to determine if variations in the thermal properties could be derived using a numerical heat transport model. A unique combination of thermal properties and porosity was established to best represent the individual experiments. The derived thermal properties indicated that there was no clear relation between organic matter content and thermal conductivity. Similarly, due to the insensitive nature of the heat capacity, no clear in-or-decreasing relation with organic matter or grain size was found. Although there were clear differences in temperature propagation rates between the individual experiments, the sensitivity range of the thermal properties limited the ability to establish a combination of thermal properties following a logical in or decreasing trend based upon either grain size or organic matter content. A more gradual transition in temperature forcing of the experiments would have resulted in a wider variation in the freeze and thaw rates between the individual experiments. As a result of the wider variation in temperature observations, it would be possible to determine the optimal thermal property combination with greater accuracy. On the other hand, the overall duration of the experiments would increase up to a time span nearing field conditions.

There was however a positive relation between organic matter content and observed porosity, as was expected. The fitting procedure reconfirmed the importance of porosity in relation to the bulk thermal properties. When attempting to determine the bulk thermal properties, porosity should be included if no field observations are available, due to the controlling effect on bulk thermal properties and shape of the Soil Freezing Characteristics Curve (SFCC). The results showed that despite variations in temperature observations between the various experiments, it proved difficult to establish a clear relation between the thermal properties and various soil properties.

While the thermal properties allow to simulate permafrost dynamics, the propagation rate of the freeze-thaw front always proved to be a controlling factor on the temporal dynamics of the active layer. As long as a part of the system undergoes the phase change, temperature remains at 0°C. In Chapter 4, ERT was explored as a viable method to track the freeze-thaw front over time. The time-lapse observations allowed us to track the freeze-thaw front over time in a column experiment. The resistivity was significantly increased during frozen conditions, as was expected due to the high

resistivity of ice compared to liquid water. Additionally, the overall spread in resistivity also increased during frozen conditions. The established temperature-resistivity relation allowed to correct for resistivity variations due to the frozen conditions, yet it does not compensate for the increase in spread of resistivity. Temperature-corrected ERT observations would therefore have a higher uncertainty at $\leq 0°C$ temperatures. Still, temperature-corrected time-lapse ERT would allow to accurately track a freeze-thaw front over time. The results revealed hysteresis in liquid and frozen porewater content during freezing and thawing, a phenomena we did not expect to detect using ERT.

5.1.2 | Conclusion

The main aim of this thesis was to improve the parameterisation of current numerical models to simulate freeze-thaw dynamics, in order to increase the accuracy, and secondly to expand the observational capabilities to study permafrost dynamics in the field and lab. Three objectives had therefore been defined:

First, to quantify the uncertainties of the thermal properties in current heat transport models (Chapter 2). Second, to determine the effect of various soil properties on the thermal properties and subsequent propagation of heat (Chapter 3), and third to contribute to detecting the freeze-thaw front in lab experiments and reducing the uncertainty of the observation (Chapter 4). Each objective had a corresponding research question, which I will reflect upon here.

How well is a numerical 1D heat transport model capable of simulating real-world permafrost freeze-thaw observations with highly uncertain thermal properties?

With the help of a 1D heat transport model (Chapter 2), we were able to simulate freeze-thaw transitions of a fieldsite at the QTP. The difficulty here lay in the absence of any information on the soil thermal properties, therefore relying solely on the available temperature observations. The thermal properties and porosity were numerically optimised in order to simulate the temperature observations at the QTP. The optimised thermal properties and porosity were within the ranges expected for the type of material located at the field site, indicating that the optimised values were representative for the actual material specific properties. At the QTP, the conductive heat transport was the dominant heat transport process, allowing the use of a 1D model to simulate active-layer dynamics. The utilisation of a 1D heat transport model to determine the thermal properties proved to be a flexible method, one that could easily be applied to other sites where temperature-depth data is available as well.

Applying this method to temperature data from other sites would allow to determine the thermal properties, thereby creating an overview of the typical ranges distributed over the arctic region. This would help to expand the knowledge on permafrost characteristics at many sites, utilising existing data and without additional sampling. There are however limitations to the method that should be considered, as in its current form, it is not designed to account for more complex situations where horizontal groundwater flows could occur, or account for a multiple-layered system (Chapter 5.1.3.2).

Can numerical heat transport models be used to infer soil thermal properties of various soil types from lab experiments?

In order to answer this research question, I consider the results from Chapters 2 and 3. The main findings in Chapter 2 confirm that thermal properties can be determined with the help of solely temperature observations and a numerical heat transport model. The experiments as demonstrated in Chapter 3, covering a range of various soil properties show unique freezing and thawing rates for the individual experiments. The values for thermal conductivity, heat capacity and porosity were in the expected ranges. Yet, there appears to be no direct relation between the optimised thermal properties and the experiments consisting of various soil properties. We argue that this is however the result of a combination where the temperature observations of the experiments are not distributed far enough apart for the software to delineate optimal soil thermal properties that represent the various soil properties. This is further complicated by the uncertainty range of the thermal properties, where multiple parameter combinations show good fits with the observations. Numerical heat transport models are a viable method to delineate soil thermal properties of various soil types, yet in order to do so accurately, observed temperature variations should be large enough in order to prevent that multiple parameter combination overlap.

Can permafrost field resistivity observations be corrected for sub zero temperature variations?

Important information on soil resistivity is lost as resistivity values collected at sub zero temperatures are increased due to the frozen condition of the material. By quantifying the temperature-induced resistivity increase, the resistivity observation can be decomposed into the actual resistivity observation and the temperature-affected

resistivity. With the help of observations collected both during sub zero and above zero temperatures, the temperature-resistivity relation can be established. ERT observations collected at sub zero temperatures can thereby be compensated for temperature, however at the cost of accuracy due to a larger uncertainty in resistivity at sub zero temperatures. Current temperature-resistivity relations do however not include hysteresis at the freeze-thaw interval. Applying a temperature-resistivity correction here could therefore incorrectly correct the resistivity observation. Special attention should therefore be paid when correcting resistivity at the freeze-thaw interval.

5.1.3 | Limitations and uncertainties

5.1.3.1 | Scaling from lab to field

Column experiments are a tried and tested method to study freezing and thawing of various permafrost soils under controlled conditions (Nagare et al., 2012b; Mohammed et al., 2014). Great benefit is the ability to simulate a wide variety of conditions over shorter timescales under controlled conditions. Yet the question of scaling arises. What are the limitations when simulating real-world processes on smaller scales and translating them back to larger scales, on both spatial and temporal scales? Are the processes under investigation for example scale-dependent? Other elements to consider are the boundary conditions that are imposed on small-scale experiments. How well do the imposed boundaries on a small scale reflect boundaries in field conditions?

An important element to consider is the primary process under investigation. The column experiments discussed in this thesis are subjected to a freezing and thawing event, where conductive heat transport is the primary process. Conductive heat transport is a diffusive process, occurring similar on both small and large scales. Therefore, any trends found on a small scale do often hold on a larger scale as well, as long as the primary process, conductive heat transport, remains the same. This would for example be more difficult if advective heat transport is included. Where advective heat transport is less of a diffusive process, but rather more localised, with often a specific spatial direction. This would be more difficult to accurately reproduce on a small scale and subsequently accurately scale up to a larger spatial scale.

Boundary conditions are an important factor when scaling laboratory and field observations as well as for numerically simulating a laboratory setup. The temperature forcing used in the laboratory setup as discussed in Chapter 3 allowed to simulate freezing and thawing over relatively short timescales compared to the field. This allowed to perform multiple column experiments over a short timescale. Yet the subsequent analysis aimed to delineate optimal thermal properties proved to be impeded

by the shorter simulation timescale. Therefore, temporal scaling of freeze-thaw experiments should be considered when there is an emphasis on the thermal properties.

In terms of physical scaling of the experiment and the associated boundary conditions, we implemented a dual approach. Overall sample size was designed to be substantially large enough that any of the sensors would physically have two times its own size of sample material surrounding it, thereby limiting any influence from the boundaries on the sensor. Furthermore, large sample size contains enough thermal mass so that small temperature variations in the air temperature will have less of an impact on the setup. An alternative way of insulating the boundaries instead of the passive insulation was considered as well, namely using active heating and cooling plates to establish temperature gradients in the sample. Yet the benefits did not outweigh the added complexities.

Next to scaling of the temperature propagation, the experiment discussed in Chapter 4 involved the scaling of resistivity observations. How well do the inverted resistivity results from an experimental setup reflect resistivity you would observe in the field? Scaling is inherently part of resistivity observations, since resistivity varies with distance. Therefore, when applying ERT in a laboratory setting, special attention is required for the design and dimensions of the setup. Where on a large field scale, variations in electrode placement do not affect the results significantly, yet on a small scale, electrodes should be placed with high accuracy to prevent a mismatch in the inversion (Clement & Moreau, 2016). Likewise, electrode size should be reduced for small scale experiments, as they should represent points in the inversion mesh. If the electrodes are too large in a small-scale experiment, they would affect a whole zone when applying the inversion, thereby increasing the error. Proper scaling of all elements of an ERT experimental setup therefore reduces the uncertainty caused by the experimental design, and subsequent observed resistivities reflect the larger field scale.

Additional to the physical scaling of the setup from laboratory ERT observations to field ERT observations, the volume of material under investigation is also scaled. In the field, there can be large subsurface structures with a low electrical conductivity such as dry sand next to structures that are highly electrical conductive such as clay. These structures appear as zones in the inversion, but the boundaries between them are often smoothed due to the inversion process. It is difficult to mimic these contrasting structures with a large spatial scale, and the effect it has on resistivity in the lab due to the smaller physical scale. Therefore, the process under investigation in a laboratory setup must be scalable, as is the case with the freeze-thaw front. Another scalable process that is well observable both in the field as well as in a laboratory

setup is for example the infiltration of meltwater during summer thaw.

5.1.3.2 | Numerical modelling

In this study we used a set of tried and tested mathematical equations in combination with FlexPDE, a software environment to solve complex partial differential equations, to simulate the permafrost thermal dynamics (Grenier et al., 2018; Lunardini, 1985). There are multiple ways to describe permafrost freeze-thaw processes, as for example using the SFCC, that can be described using both linear or exponential empirical functions. Likewise, there are multiple software packages available to simulate groundwater flow including the porewater freezing and thawing (McKenzie et al., 2007; Grenier et al., 2018). Our goal is to present our results, for example the sensitivity of the thermal properties, as generically as possible, so that they could be applied independent of the software being used.

Evaluating model performance

We have presented multiple ways to evaluate the mismatch between data and observation, either by comparing individual point observations (RMSE and KGE error), evaluating the mismatch in timing (Russel's phase error) or the size/amplitude of the freeze-thaw process (Russel's magnitude error) (Chapter 2). Each method yielded different results, making it an ambiguous process. This raised the question, which element of the fitting procedure is most important and do you want to fit the data to, either review the timing aspect, or the size/amplitude of the process?

Neither of the methods are incorrect, however it should be a conscience consideration, utilising either of the methods. The choice depends on the process under investigation, whilst being aware of the uncertainties that are involved. Timing for example plays a crucial role when reviewing seasonal temporal variations. As permafrost thaw triggers an increase in summer groundwater discharge and thereby associated increase in river discharge. These are of special importance for human activities in and around the permafrost areas. On longer multiyear timescales however, the magnitude of the effects might play a more important role. For example when investigating long-term active-layer thawing depth that could trigger deep multi-year groundwater flows and associated DOC transport.

Improving SFCC

Numerical models are under constant development, aspiring to include the latest developments in process simulations. There are improvements to be made both in terms of improving the simulations as well as the approach how we use the simulations as part of the research to determine the optimal parameters. The SFCC is an important element describing the phase transition of the porewater, yet not all processes that take place during repeated freezing and thawing are included.

To improve the numerical simulations, the hysteresis of the liquid water content during freezing and thawing should be included. As permafrost warms, it will fluctuate more and more around the 0°C mark. Consequently, the system stays in a constant phase change state. Yet, while temperature remains stable around the 0°C mark, energy enters and leaves the system, affecting the liquid water content. Studies have shown that the hysteresis loops are however soil material specific (Tian et al., 2014). The inclusion of hysteresis in the numerical models would allow to more accurately simulate the liquid water fraction during various moment in time of the phase change transition. The numerical representation should allow to simulate a hysteresis loop for both a full freeze-thaw cycle as well as partial freeze-thaw cycles. The inclusion of hysteresis however adds to further model complexity and additional parameters to fit, potentially increasing the uncertainty rather than decreasing the uncertainty of the model simulations.

Multi-layer approach

The numerical model simulations used in Chapter 2 relied on a vertical 1D model to simulate the permafrost dynamics. The model contained a single layer, simplifying the field conditions, allowing it to be used to prove the concept that the thermal properties could be determined by evaluating the whole parameter range. When it comes to improving model performance, an obvious improvement would be the inclusion of a multiple-layered model approach, that allows to include an unsaturated zone and heterogeneity in thermal properties at varying depths. Additional layers would allow to assign specific thermal properties and porosity values to each soil layer. This would however increase the complexity significantly to accurately determine the thermal properties for the individual layers, since they are all connected. When adding a multiple-layer system, the question should arise what the goal is you would like to achieve. Either to generically evaluate the fit between the model and the observations to determine the thermal properties, or to make a site-specific model to accurately simulate permafrost dynamics over longer timescales?

Using a 1D numerical model to determine the thermal properties as demonstrated in Chapter 2 would not work in situations where there is an apparent lateral groundwater component that could develop over time. In that case, advective heat flow should be included additional to the conductive heat flow, requiring a more complex 2D layered model approach. Thereby consequently increasing the number of parameters, including a variable hydraulic conductivity. The addition of multiple layers and more parameters would ask for a different approach to optimise the parameter values, since the overall parameter space would increase exponentially. Automatic optimisation algorithms would reduce the total number of model runs, yet with the chance that one would find local minima, rather than the global minimum (Albers et al., 2020). A combination of both an automatic optimisation algorithm and running the full parameter space for the sensitive parameters could be the solution here. Another option would be to take advantage of emerging machine learning techniques to analyse large parameter spaces to find trends in parameter combinations with low errors, this could speed up the fitting procedure and prevent the effects of selecting local minima.

5.1.4 | Future outlook

Present day permafrost dynamics can be simulated using a various numerical models, yet parameterisation of the thermal soil specific properties proves difficult without reliable field data. As shown in this thesis, temperature-depth observations and data collected using column experiments can be used to determine the thermal properties without collecting additional field samples. Furthermore, the experiments using the ERT observations showed how additional information could be obtained form ERT observations collected during both freezing and thawing conditions. All of this contributes to deepen our understanding on the changing permafrost dynamics. There are multiple opportunities for future efforts to improve our modelling, to include more processes such as reactive transport, and expand our observational capabilities.

5.1.4.1 | Large-scale thermal property distribution

There are opportunities to apply the method described in Chapter 2 on temperature-depth data collected at fixed observation sites to derive the thermal properties. This would create a spatial overview of ranges of thermal properties at various sites. An example could be temperature observations collected by the Circumpolar Active Layer Monitoring Program (CALM) (J. Brown & Nelson, 2000), or from other perma-

frost observatories. The ranges in thermal properties would help to parameterise and increase the accuracy of local as well as larger scale numerical active layer models.

5.1.4.2 | DOC transport

So far, we have discussed how heat transport models are used to model short and long-term permafrost dynamics, that subsequently allow us to study the evolution of groundwater in thawing permafrost areas. This is however not yet linked to the release and transport of DOC, which is one of the uncertainties in the carbon cycle. Due to the importance of carbon transport and release from permafrost areas, the next step would be to couple carbon transport to the freeze-thaw models. Efforts are being made on including solute transport in the current numerical heat transport models (Mohammed et al., 2022). However, as is the case with the parameterisation of the thermal properties, likewise the release of the DOC into the groundwater, dissolvement rates and transport efficiency are yet to be parameterised.

Column experiments as demonstrated in this thesis, in combination with field data would be a logical starting point to provide the necessary data for the parametrisation. Field data could comprise of DOC values collected in surface streams and samples collected in piezometers. As part of a continuation on the static column experiments discussed in this thesis, a proof of concept column setup has been designed that could be subjected to repeated freezing and thawing, whilst simulating groundwater flow through the sample. The setup includes automatic sampling of the groundwater to measure the DOC concentration over time. Initial testing confirms the complexities involved, due to the evolving groundwater flux in combination with the reactive properties of the organic material used in the setup, this requires further testing.

5.1.4.3 | Time-lapse ERT observations

Chapter 4 has showed that ERT observations contain information on variations in liquid water content during freezing and thawing. Field observations of the temporal dynamics of the liquid water content would be useful to monitor reactivation of subsurface groundwater fluxes. Yet the relation between resistivity and liquid water content needs further investigation before it can be applied. Next to that, the proposed temperature-correction allows to monitor transient processes without interference from temperature variations.

Future work should focus on both elements. First, the variations in liquid water content and associated hysteresis are not yet fully understood, therefore we propose an additional column experiment, subjected to multiple freeze-thaw events and partial freezing and thawing. Additionally, observational methods like Nuclear Magnetic

Resonance (NMR) could be added to the experimental setup to delineate the liquid water content and be used as an independent method to confirm the relation between the liquid water content and resistivity (Tian et al., 2014).

Secondly, existing and future ERT time-lapse observations could benefit from the new analysis method to analyse the data to extract additional information. Specially long-term observation sites could yield valuable information on the spatial and temporal dynamics of variations in for example water saturation when corrected for temperature. As an example, ERT is used in permafrost areas to detect groundwater flow (Hornum et al., 2021), temperature-correcting these ERT observations will help to increase the detection capability of these groundwater flows by removing the temperature-induced temperature increase.

5.1.4.4 | Outlook

In the end, permafrost research is aimed at improving our understanding of this frozen landscape and develop simulation capabilities in order to provide the society with the necessary information on the future of permafrost. Next to the opportunities that we proposed based upon this research, a number of general opportunities in the field of permafrost research were identified.

The upcoming usage of machine learning and artificial intelligence could be useful in permafrost research. It can either be used to fully simulate permafrost dynamics, or used to analyse data misfit and determine favourable parameter combinations. So far, machine learning has not been widely used in permafrost research. Since these are data-driven processes, data scarcity could be a limiting factor to apply it.

To increase data availability, we should diversify our data collection methods and data sources. The data used in this thesis comprises solely of subsurface observations to asses permafrost dynamics. Yet, with continuous improvement of remote sensing techniques, new possibilities emerge to derive subsurface permafrost dynamics and monitor the thermal stability using remote sensing. With the help of remote sensing, dynamics observed at local field sites could be extrapolated to larger areas. One of the upcoming techniques is to observe permafrost deformation using Interferometric Synthetic Aperture Radar (InSAR). Here, temporal variations in uplift and subsidence are linked to frost heave and thaw subsidence. These are related to long term permafrost thaw and seasonal active layer thawing rates (Jiang et al., 2020). Improvements in resolution and lead-times ensure that InSAR permafrost observations become more reliable.

Ultimately, a combination of various field observations and numerical modelling is

needed to unravel permafrost dynamics across a variety of landscapes, ranging from frozen barren soils to water and vegetation rich thermokarst landscapes.

6

Appendices

Appendices

A | Additional results of Chapter 2

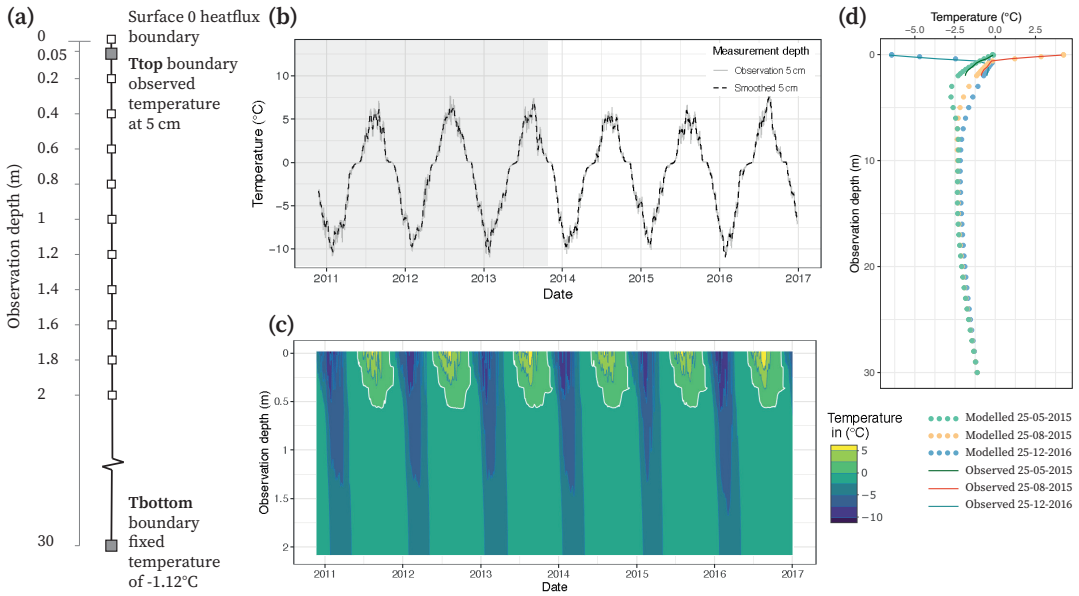

Figure A.1 | (a) Shows a conceptual representation of the 1D numerical model, including the nodes at which the temperature exported. These are at the same depths as observed in the field. (b) Observed temperature at 5 cm depth, and the smoothed temperature, used as model forcing. First grey half is used for model calibration and the second half for validation. (c) Observed temperature over time for 2 meters depth, where the white line indicates the 0 °Cboundary. (d) Three observed temperature-depth plots and the modelled temperatures for the top 2 meters that had the best RMSE fit.

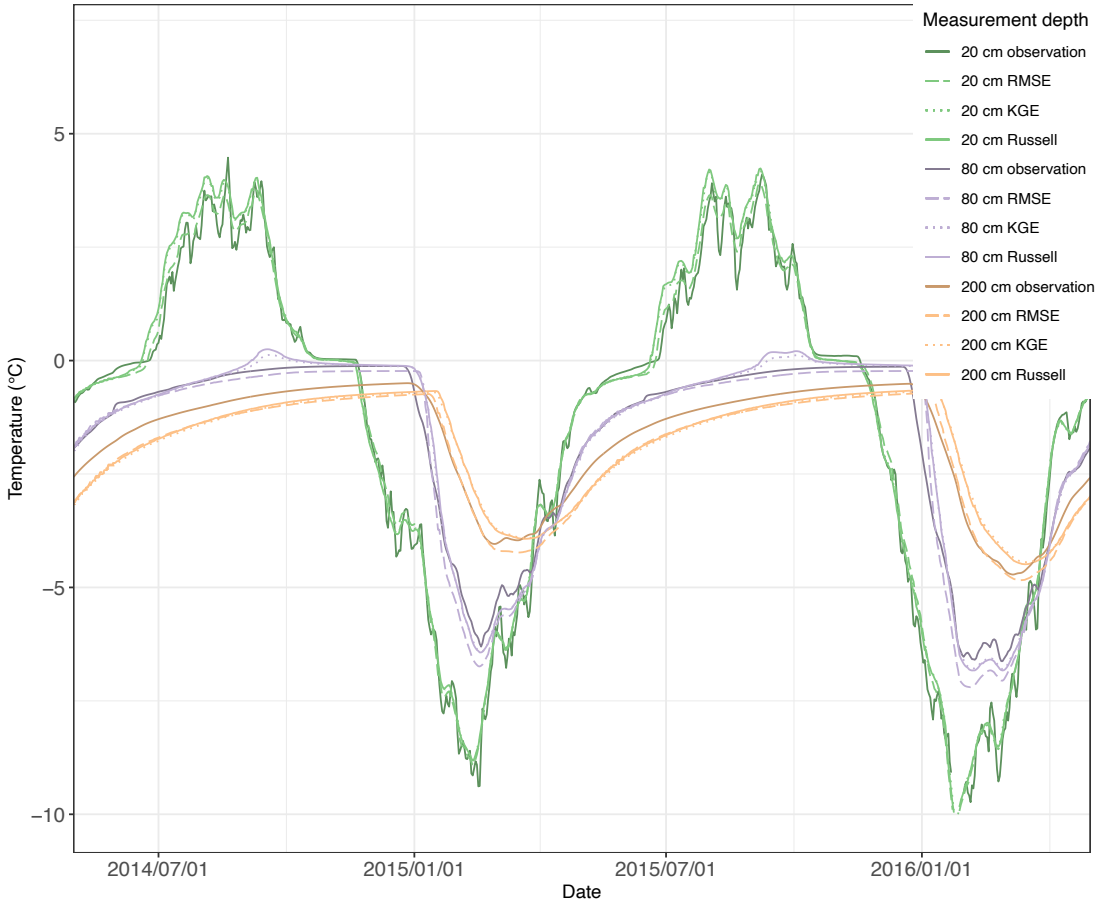

Figure A.2 | Selection of the observed data and best model fits for the RMSE, KGE and Russel's error at various depths.

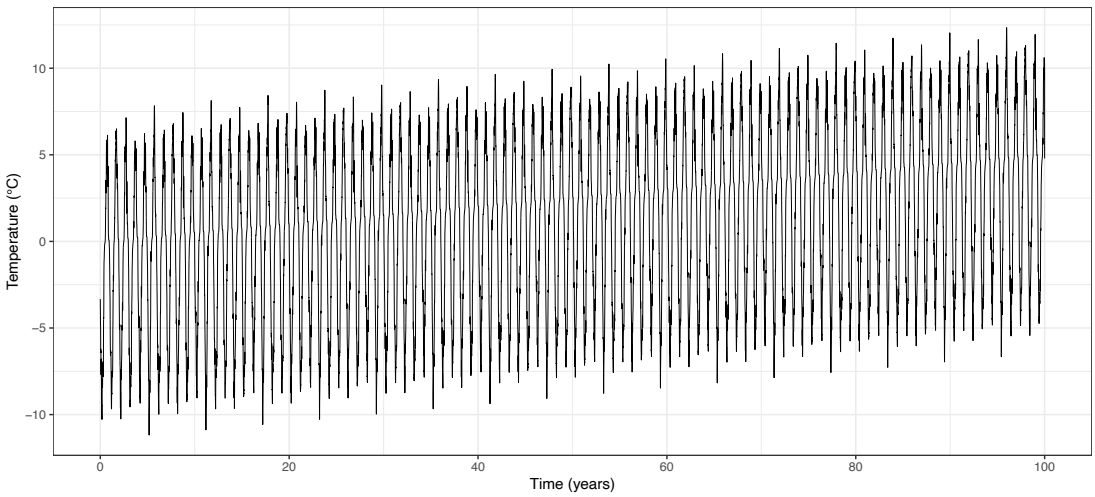

Figure A.3 | Boundary condition used for the 100 year future prediction, based upon a 5°C temperature increase and seasonal variations as observed in the 6 year timeseries over the QTP.

B | Additional results of Chapter 3

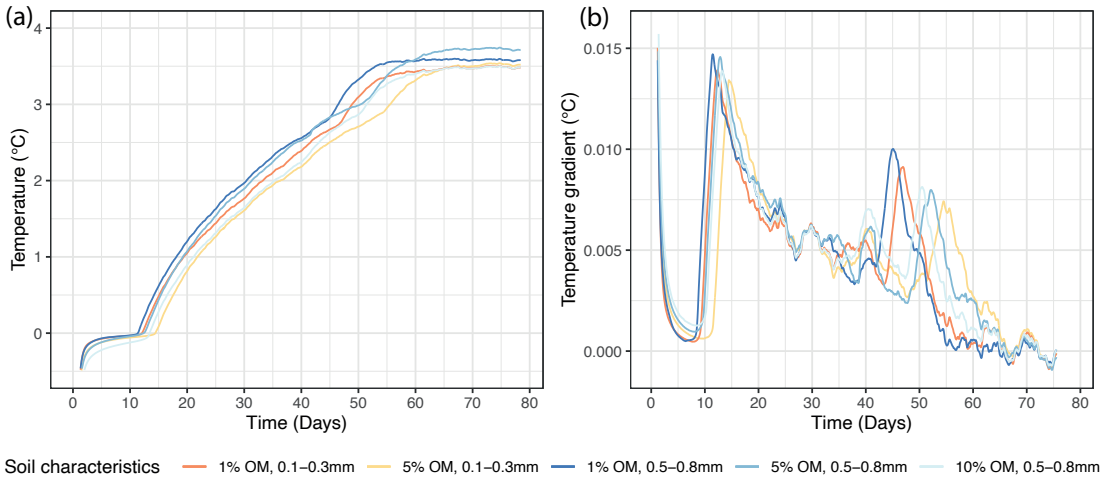

Figure B.1 | (a) Subset of recorded temperatures during thawing in five of the nine columns with varying soil properties at a depth of 35 cm. (b) Gradient plot of the temperatures from panel (a), showing the distinct difference in timing as the temperature exceeds 0 °C between the various columns.

C | Additional results of Chapter 4

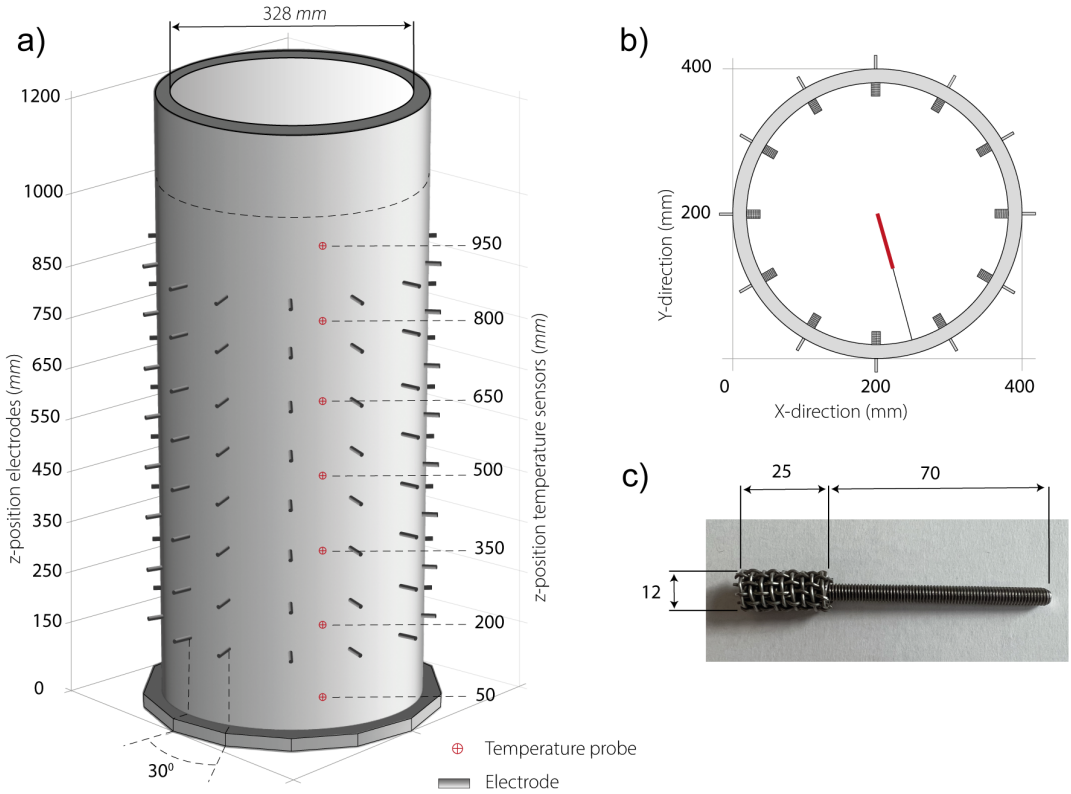

Figure C.1 | a) Technical drawing of the ERT column setup and sensor placement. b) Horizontal cross-section of the column, showing the 12 electrodes on the circumference of the column and in red the temperature sensor. c) Photo of one of the electrodes with the wire-mesh tip (dimensions in mm).

Figure C.2 | Photo of the column setup showing the HDPE column, electrodes located around the circumference, and orange wires connecting all of the 96 individual electrodes to the switch boxes, that connect to the Syscal ERT.

Table C.1 | Temperature-electrical resistivity model parameters numerically optimized, based upon Herring et al. (2019), SFCC as described in McKenzie et al. (2007).

Parameter	Description	Optimal parameters freezing	Optimal parameters thawing
ϕ	Porosity $(m^3 m^{-3})$	0.35	0.4
C_0	Porewater TDS concentration (gL^{-1})	0.5	0.5
k	Correlation factor fluid resistivity at 25 °C (ΩmgL^{-1})	0.15	0.14
a	Tortuosity factor $(-)$	0.363	0.363
m	Cementation exponent $(-)$	1.32	1.32
n	Saturation exponent $(-)$	2.29	2.29
S_{wL}	Water saturation curve SFCC $(m^3 m^{-3})$, (T in °C) $S_{wL} = (1 - S_{wres}) exp(-((T)/W)^2) + S_{wres}$		
S_{w0}	Initial water saturation $(m^3 m^{-3})$	0.3	0.5
S_{wres}	Residual saturation $(m^3 m^{-3})$	0.03	0.02
W	Fitting parameter for SFCC $(-)$	0.5	0.3

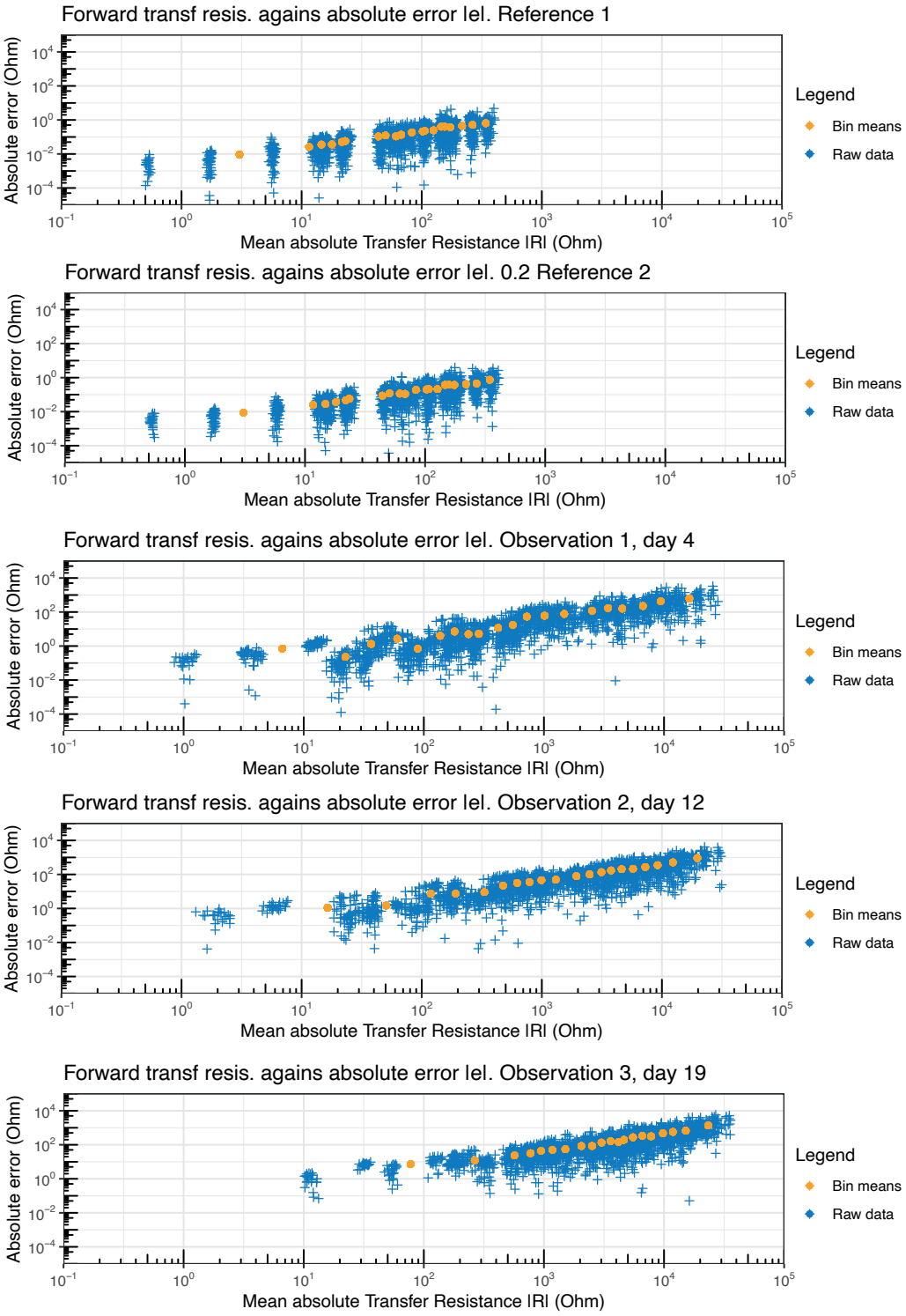

Figure C.3 | Mean absolute transfer resistance plotted versus the absolute error calculated using the normal and reciprocal observation. Data is binned into equal sized bins, of which the mean is determined. This is used to determine the error in the ERT observations. Shown are two reference observations, and the first three observations as indicated in Figure 4.2 collected during the freezing stage.

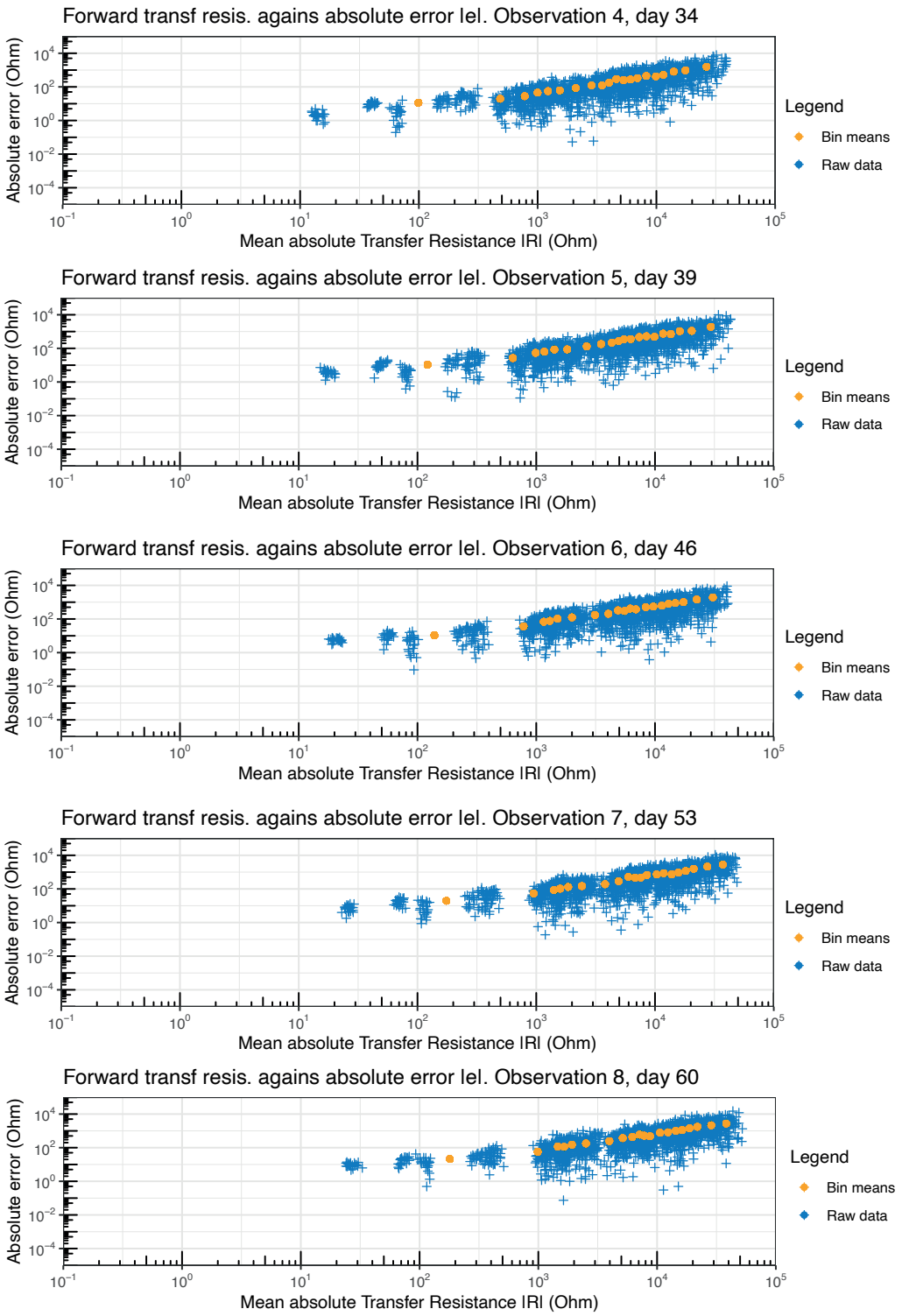

Figure C.4 | Mean absolute transfer resistance plotted versus the absolute error calculated using the normal and reciprocal observation. Data is binned into equal sized bins, of which the mean is determined. This is used to determine the error in the ERT observations. Shown are observations 4 to 8 as indicated in Figure 4.2 collected during the freezing stage.

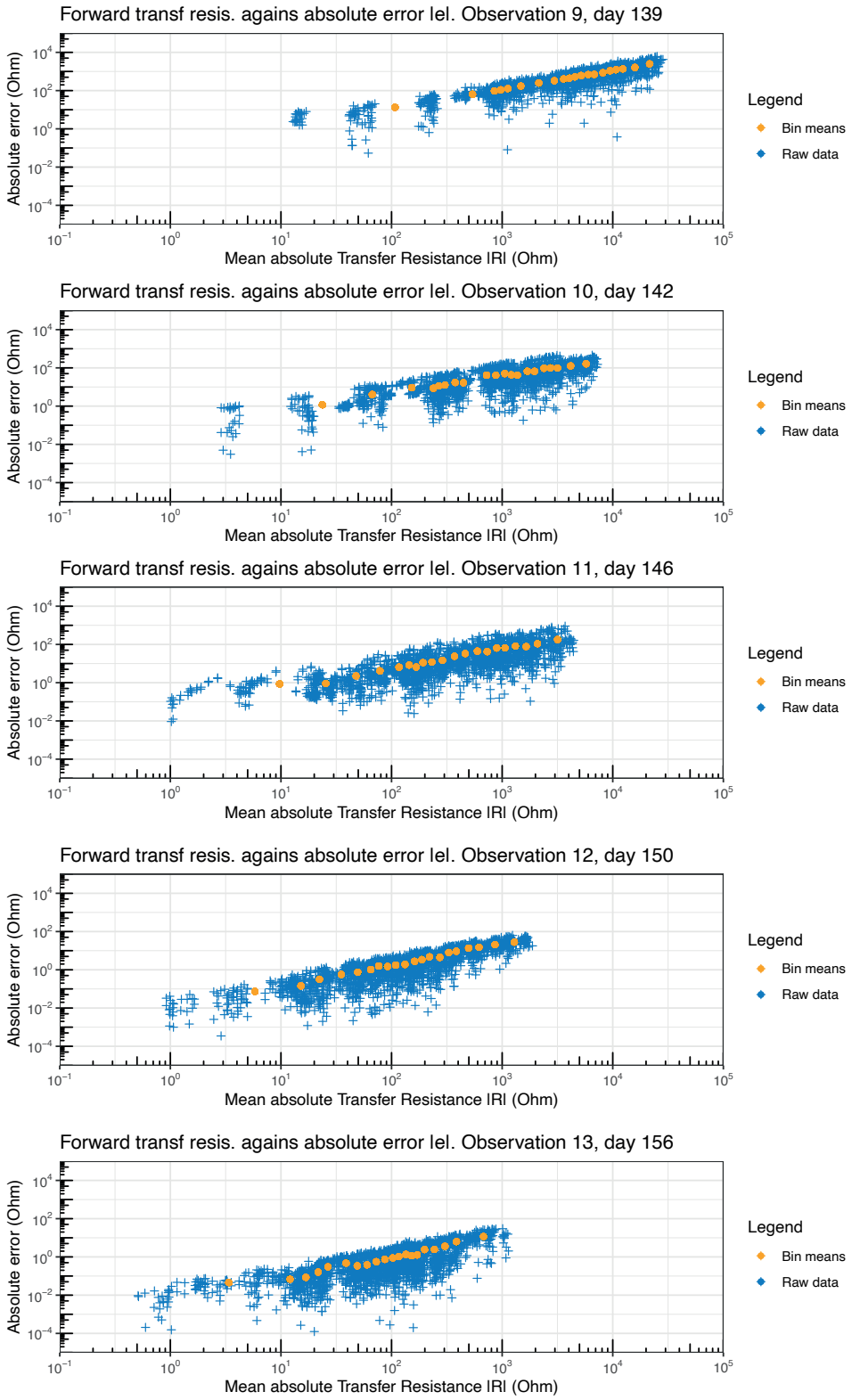

Figure C.5 | Mean absolute transfer resistance plotted versus the absolute error calculated using the normal and reciprocal observation. Data is binned into equal sized bins, of which the mean is determined. This is used to determine the error in the ERT observations. Shown are observations 9 to 13 as indicated in Figure 4.2 collected during the freezing stage.

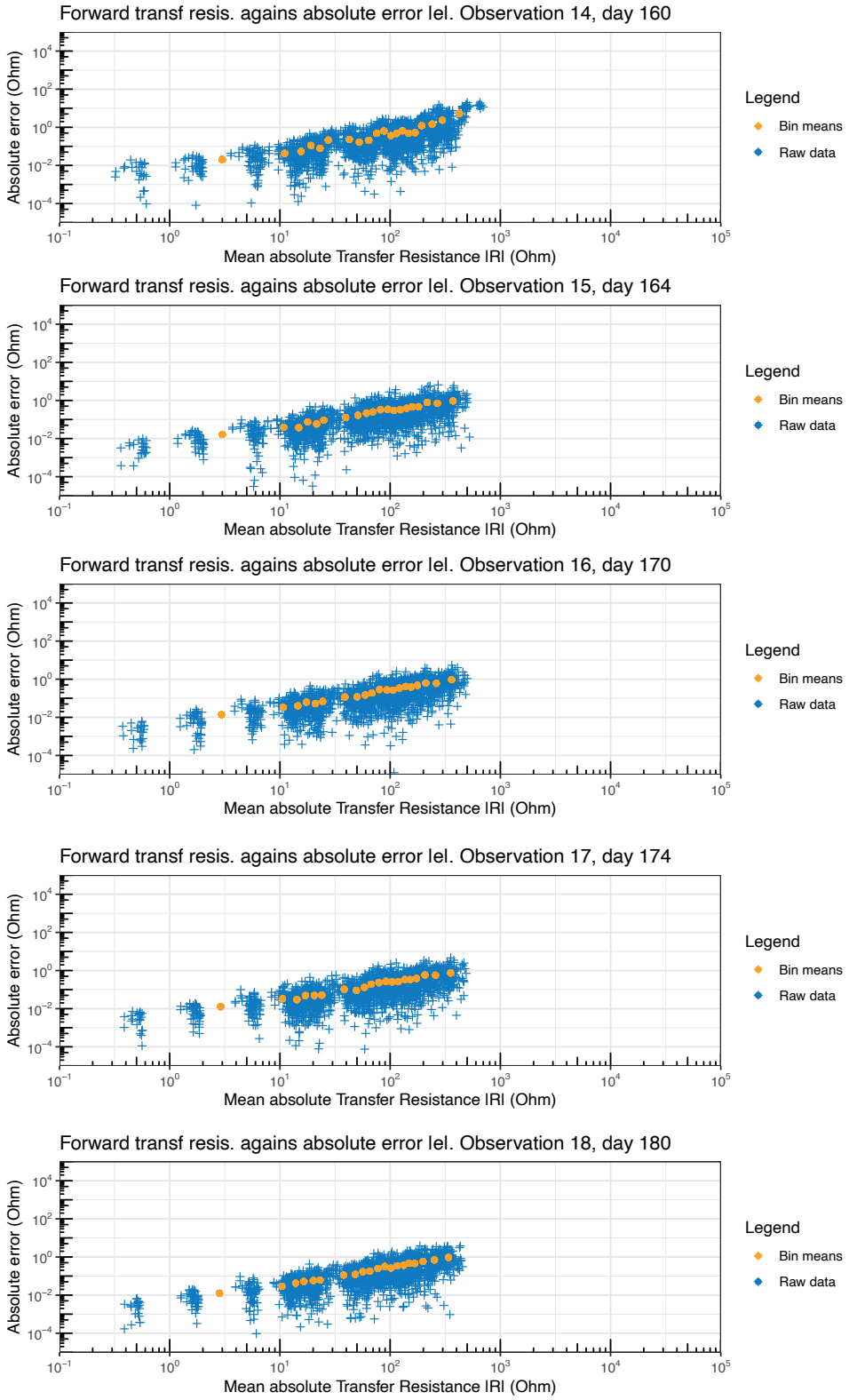

Figure C.6 | Mean absolute transfer resistance plotted versus the absolute error calculated using the normal and reciprocal observation. Data is binned into equal sized bins, of which the mean is determined. This is used to determine the error in the ERT observations. Shown are observations 14 to 18 as indicated in Figure 4.2 collected during the freezing stage.

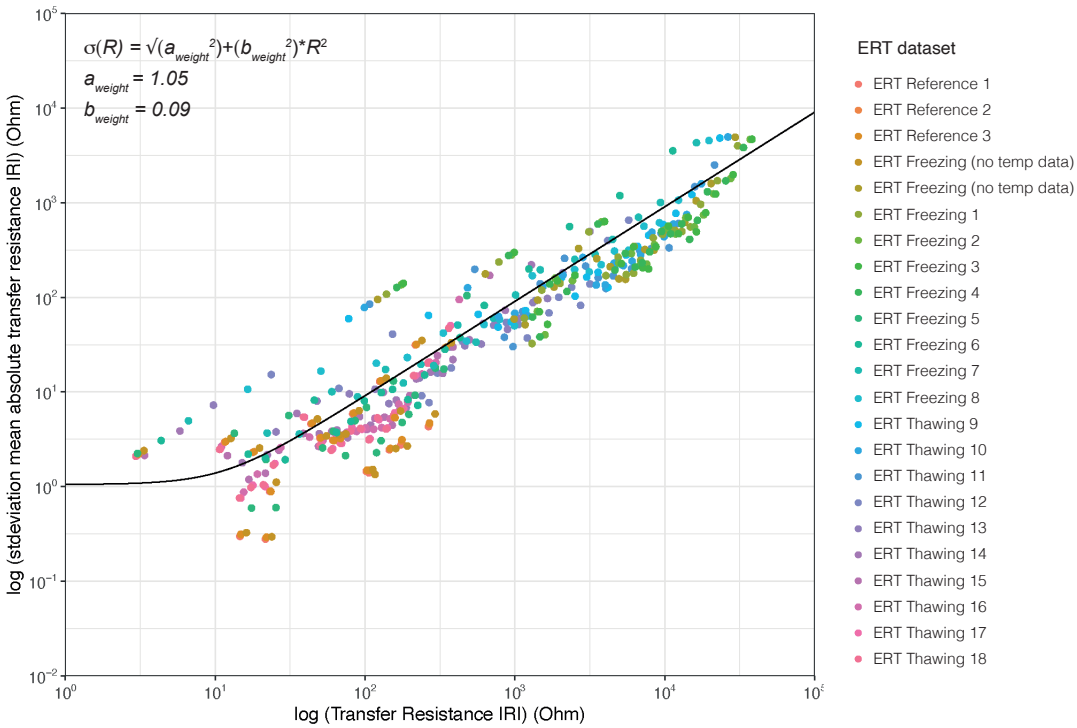

Figure C.7 | Error model fitted to the binned transfer resistances of all gathered ERT datasets both during freezing and thawing as shown in Figures C.3, C.4, C.5 and C.6.

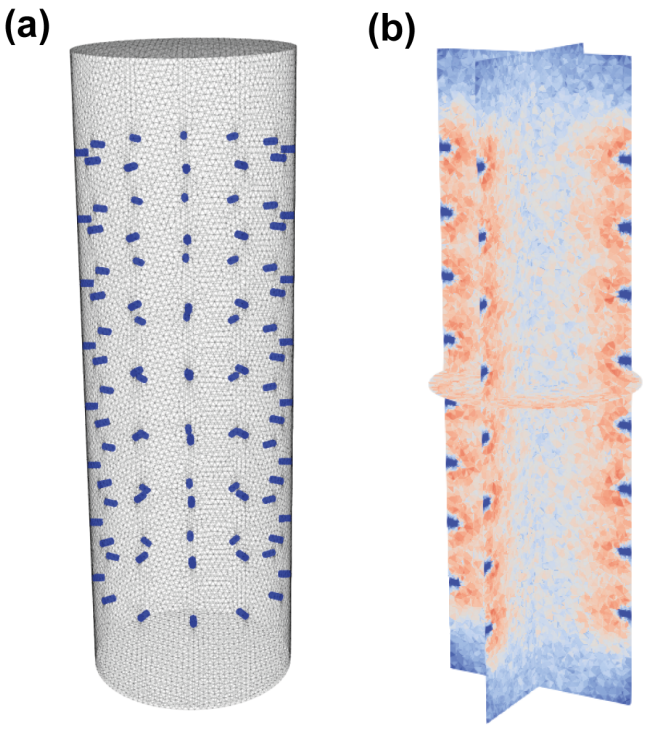

Figure C.8 | a) 3D mesh of the column, where the blue zones indicate the locations of the electrodes that have a fixed resistivity. b) Sensitivity distribution of the reference ERT observation, where blue indicate zones of low sensitivity, and red indicate a high sensitivity.

Bibliography

Abramov, A., S. Davydov, A. Ivashchenko, D. Karelin, A. Kholodov, G. Kraev, A. Lupachev, A. Maslakov, V. Ostroumov, E. Rivkina, D. Shmelev, V. Sorokovikov, O. Tregubov, A. Veremeeva, D. Zamolodchikov & S. Zimov (2019). Two decades of active layer thickness monitoring in northeastern Asia. *Polar Geography*, 0(0), 1–17. doi: 10.1080/1088937X.2019.1648581.

Abu-Hamdeh, N. H. (2003). Thermal properties of soils as affected by density and water content. *Biosystems Engineering*, 86(1), 97–102.

Abu-Hamdeh, N. H. & R. C. Reeder (2000). Soil thermal conductivity effects of density, moisture, salt concentration, and organic matter. *Soil Science Society of America Journal*, 64(4), 1285–1290. doi: 10.2136/sssaj2000.6441285x.

Åkerman, H. J. & M. Johansson (2008). Thawing permafrost and thicker active layers in sub-arctic Sweden. *Permafrost and Periglacial Processes*, 19(3), 279–292. doi: 10.1002/ppp.626.

Akyurt, M., G. Zaki & B. Habeebullah (2002). Freezing phenomena in ice–water systems. *Energy Conversion and Management*, 43(14), 1773–1789. doi: https://doi.org/10.1016/S0196-8904(01)00129-7.

Albers, B. M. C., J. W. Molson & V. F. Bense (2020). Parameter sensitivity analysis of a two-dimensional cryo-hydrogeological numerical model of degrading permafrost near Umiujaq (Nunavik, Canada). *Hydrogeology Journal*, 28(3), 905–919.

Altshuler, I., J. Goordial & L. G. Whyte (2017). *Microbial Life in Permafrost*, pages 153–179. Springer International Publishing.

Amiri, E. A., J. R. Craig & B. L. Kurylyk (2018). A theoretical extension of the soil freezing curve paradigm. *Advances in Water Resources*, 111, 319–328.

Andresen, C. G., D. M. Lawrence, C. J. Wilson, A. D. McGuire, C. Koven, K. Schaefer, E. Jafarov, S. Peng, X. Chen, I. Gouttevin, E. Burke, S. Chadburn, D. Ji, G. Chen, D. Hayes & W. Zhang (2020). Soil moisture and hydrology projections of the permafrost region – a model intercomparison. *The Cryosphere*, 14(2), 445–459.

Anisimov, O., D. Vaughan, T. Callaghan, C. Furgal, H. Marchant, T. Prowse, H. Vilhjálmsson & J. Walsh (2007). Climate change 2007: Impacts, adaptation and vulnerability. contribution of working group ii to the fourth assessment report of the Intergovernmental Panel on Climate Change. *M.L. Parry, O.F. Canziani, J.P. Palutikof, P.J. van der Linden and C.E. Hanson, Eds., Cambridge University Press, Cambridge*, pages 653–685.

Arias-Penas, D., M. Castro-García, M. Rey-Ronco & T. Alonso-Sánchez (2015). Determining the thermal diffusivity of the ground based on subsoil temperatures. Preliminary results of an experimental geothermal borehole study Q-THERMIE-UNIOVI. *Geothermics*, 54, 35 – 42.

Bechtold, M., J. Vanderborght, L. Weihermüller, M. Herbst, T. Günther, O. Ippisch, R. Kasteel & H. Vereecken (2012). Upward transport in a three-dimensional heterogeneous laboratory soil under evaporation conditions. *Vadose Zone Journal*, 12.

Bennett, N. D., B. F. Croke, G. Guariso, J. H. Guillaume, S. H. Hamilton, A. J. Jakeman, S. Marsili-Libelli, L. T. Newham, J. P. Norton, C. Perrin, S. A. Pierce, B. Robson, R. Seppelt, A. A. Voinov, B. D. Fath & V. Andreassian (2013). Characterising performance of environmental models. *Environmental Modelling & Software*, 40, 1 – 20.

Bense, V. F., G. Ferguson & H. Kooi (2009). Evolution of shallow groundwater flow systems in areas of degrading permafrost. *Geophysical Research Letters*. doi: 10.1029/2009GL039225.

Bense, V. F., H. Kooi, G. Ferguson & T. Read (2012). Permafrost degradation as a control on hydrogeological regime shifts in a warming climate. *Journal of Geophysical Research: Earth Surface*, 117(F3). doi: 10.1029/2011JF002143.

Bhamidi, V., P. J. A. Kenis & C. F. Zukoski (2017). Probability of nucleation in a metastable zone: Induction supersaturation and implications. *Crystal Growth & Design*, 17(3), 1132–1145. doi: 10.1021/acs.cgd.6b01529.

Binley, A. (2015). *DC electrical methods*, volume 11, pages 233–259. Elsevier, 2nd edition. doi: 10.1016/B978-0-444-53802-4.00192-5.

Binley, A., S. Henry-Poulter & B. Shaw (1996). Examination of solute transport in an undisturbed soil column using electrical resistance tomography. *Water Resources Research*, 32, 763–769. doi: 10.1029/95WR02995.

Binley, A. & L. Slater (2020). *Resistivity and Induced Polarization*. Cambridge University Press.

Biskaborn, B. K., S. L. Smith, J. Noetzli, H. Matthes, G. Vieira, D. A. Streletskiy, P. Schoeneich, V. E. Romanovsky, A. G. Lewkowicz, A. Abramov, M. Allard, J. Boike, W. L. Cable, H. H. Christiansen, R. Delaloye, B. Diekmann, D. Drozdov, B. Etzelmüller, G. Grosse, M. Guglielmin, T. Ingeman-Nielsen, K. Isaksen, M. Ishikawa, M. Johansson, H. Johannsson, A. Joo, D. Kaverin, A. Kholodov, P. Konstantinov, T. Kröger, C. Lambiel, J. P. Lanckman, D. Luo, G. Malkova, I. Meiklejohn, N. Moskalenko, M. Oliva, M. Phillips, M. Ramos, A. B. K. Sannel, D. Sergeev, C. Seybold, P. Skryabin, A. Vasiliev, Q. Wu, K. Yoshikawa, M. Zheleznyak & H. Lantuit (2019). Permafrost is warming at a global scale. *Nature Communications*, 10.

Bloem, E., N. Forquet, A. Søiland, A. Binley & H. K. French (2020). Towards understanding time-lapse electrical resistivity signals measured during contaminated snowmelt infiltration. *Near Surface Geophysics*, 18(Geoelectrical Monitoring), 399–412. doi: https://doi.org/10.1002/nsg.12112.

Bockheim, J. G. & K. M. Hinkel (2007). The importance of "deep" organic carbon in permafrost-affected soils of Arctic Alaska. *Soil Science Society of America Journal*, 71(6), 1889–1892.

Bouchard, F., P. Francus, R. Pienitz, I. Laurion & S. Feyte (2014). Subarctic thermokarst ponds: Investigating recent landscape evolution and sediment dynamics in thawed permafrost of northern Québec (Canada). *Arctic, Antarctic, and Alpine Research*, 46(1), 251–271. doi: 10.1657/1938-4246-46.1.251.

Box, J. E., W. T. Colgan, T. R. Christensen, N. M. Schmidt, M. Lund, F. J. W. Parmentier, R. Brown, U. S. Bhatt, E. S. Euskirchen, V. E. Romanovsky, J. E. Walsh, J. E. Overland, M. Wang, R. W. Corell, W. N. Meier, B. Wouters, S. Mernild, J. Mård, J. Pawlak & M. S. Olsen (2019). Key indicators of Arctic climate change: 1971–2017. *Environmental Research Letters*, 14(4).

Brouchkov, A., M. Fukuda, G. Iwahana, Y. Kobayashi & P. Konstantinov (2005). Thermal conductivity of soils in the active layer of eastern Siberia. *Permafrost and Periglacial Processes*, 16(2), 217–222. doi: 10.1002/ppp.502.

Brown, J., O. J. Ferrians, Jr, J. A. Heginbottom & E. S. Melnikov (1997). *Circum-Arctic map of permafrost and ground-ice conditions*. Technical Report 45.

Bruhwiler, L., F. J. W. Parmentier, P. Crill, M. Leonard & P. I. Palmer (2021). The arctic carbon cycle and its response to changing climate. *Current Climate Change Reports*, 7(1), 14–34.

de Bruin, J. G. H., V. F. Bense & M. J. van der Ploeg (2021). Inferring permafrost active layer thermal properties from numerical model optimization. *Geophysical Research Letters*, 48(16), e2021GL093306. doi: https://doi.org/10.1029/2021GL093306.

Buckel, J., J. Mudler, R. Gardeweg, C. Hauck, C. Hilbich, R. Frauenfelder, C. Kneisel, S. Buchelt,

J. H. Blöthe, A. Hördt & M. Bücker (2023). Identifying mountain permafrost degradation by repeating historical electrical resistivity tomography (ert) measurements. *The Cryosphere*, 17(7), 2919–2940. doi: 10.5194/tc-17-2919-2023.

Carson, J. E. (1963). Analysis of soil and air temperatures by fourier techniques. *Journal of Geophysical Research (1896-1977)*, 68(8), 2217–2232. doi: https://doi.org/10.1029/JZ068i008p02217.

Chen, S., X. Li, T. Wu, K. Xue, D. Luo, X. Wang, Q. Wu, S. Kang, H. Zhou & D. Wei (2020). Soil thermal regime alteration under experimental warming in permafrost regions of the central Tibetan Plateau. *Geoderma*, 372, 114397.

Cheng, G. & H. Jin (2013). Permafrost and groundwater on the Qinghai-Tibet Plateau and in northeast China. *Hydrogeology Journal*, 21, 5–23.

Cheng, G. & T. Wu (2007). Responses of permafrost to climate change and their environmental significance, Qinghai-Tibet Plateau. *Journal of Geophysical Research: Earth Surface*, 112.

Clement, R. & S. Moreau (2016). How should an electrical resistivity tomography laboratory test cell be designed? numerical investigation of error on electrical resistivity measurement. *Journal of Applied Geophysics*, 127, 45 – 55. doi: https://doi.org/10.1016/j.jappgeo.2016.02.008.

Cochand, M., J. Molson & J. M. Lemieux (2019). Groundwater hydrogeochemistry in permafrost regions. *Permafrost and Periglacial Processes*, 30.

Constable, A. J., S. Harper, J. Dawson, K. Holsman, T. Mustonen, D. Piepenburg, B. Rost, S. Bokhorst, J. Boike, A. Cunsolo, C. Derksen, P. Feodoroff, J. D. Ford, S. E. Howell, A. C. Katny, J. P. MacDonald, Å. Ønvik, S. A. Robinson, D. S. Dorough, V. Shadrin, M. Skern-Mauritzen, S. L. Smith, D. Streletskiy, M. Tsujimoto & B. V. Dam (2022). Cross-chapter paper 6: Polar regions.

Devoie, E. G., S. Gruber & J. M. McKenzie (2022). A repository of 100+ years of measured soil freezing characteristic curves. *Earth System Science Data Discussions*, 2022, 1–21. doi: 10.5194/essd-2022-61.

Diak, M., M. E. Böttcher, C. M. Ehlert von Ahn, W. L. Hong, M. Kędra, L. Kotwicki, K. Koziorowska-Makuch, K. Kuliński, A. Lepland, P. Makuch, A. Sen, A. Winogradow, M. J. Silberberger & B. Szymczycha (2023). Permafrost and groundwater interaction: current state and future perspective. *Frontiers in Earth Science*, 11.

Ding, Y., W. Wang, R. Song, Q. Shao, X. Jiao & W. Xing (2017). Modeling spatial and temporal variability of the impact of climate change on rice irrigation water requirements in the middle and lower reaches of the Yangtze River, China. *Agricultural Water Management*, 193, 89–101.

Dissanayaka, S. H., S. Hamamoto, K. Kawamoto, T. Komatsu & P. Moldrup (2012). Thermal properties of peaty soils: Effects of liquid-phase impedance factor and shrinkage. *Vadose Zone Journal*, 11(1). doi: 10.2136/vzj2011.0092.

Dobinski, W. (2011). Permafrost. *Earth-Science Reviews*, 108(3), 158–169. doi: https://doi.org/10.1016/j.earscirev.2011.06.007.

Dutta, K., E. A. G. Schuur, J. C. Neff & S. A. Zimov (2006). Potential carbon release from permafrost soils of Northeastern Siberia. *Global Change Biology*, 12(12), 2336–2351.

Ebel, B. A., J. C. Koch & M. A. Walvoord (2019). Soil physical, hydraulic, and thermal properties in interior alaska, usa: Implications for hydrologic response to thawing permafrost conditions. *Water Resources Research*, 55(5), 4427–4447.

Farouki, O. T. (1981). The thermal properties of soils in cold regions. *Cold Regions Science and Technology*, 5(1), 67–75. doi: https://doi.org/10.1016/0165-232X(81)90041-0.

Farzamian, M., G. Vieira, F. A. Monteiro Santos, B. Yaghoobi Tabar, C. Hauck, M. C. Paz, I. Bernardo, M. Ramos & M. A. de Pablo (2020). Detailed detection of active layer freeze–thaw dynamics

using quasi-continuous electrical resistivity tomography (deception island, antarctica). *The Cryosphere*, 14(3), 1105–1120. DOI: 10.5194/tc-14-1105-2020.

Fernandez, P. M., E. Bloem, A. Binley, R. S. Philippe & H. K. French (2019). Monitoring redox sensitive conditions at the groundwater interface using electrical resistivity and self-potential. *Journal of Contaminant Hydrology*, 226, 103517.

Fisher, J. P., C. Estop-Aragonés, A. Thierry, D. J. Charman, S. A. Wolfe, I. P. Hartley, J. B. Murton, M. Williams & G. K. Phoenix (2016). The influence of vegetation and soil characteristics on active-layer thickness of permafrost soils in boreal forest. *Global Change Biology*, 22(9), 3127–3140.

Frampton, A., S. Painter, S. W. Lyon & G. Destouni (2011). Non-isothermal, three-phase simulations of near-surface flows in a model permafrost system under seasonal variability and climate change. *Journal of Hydrology*, 403(3), 352 – 359.

Frampton, A., S. L. Painter & G. Destouni (2013). Permafrost degradation and subsurface-flow changes caused by surface warming trends. *Hydrogeology Journal*.

French, H. & A. Binley (2004). Snowmelt infiltration: monitoring temporal and spatial variability using time-lapse electrical resistivity. *Journal of Hydrology*, 297(1), 174 – 186. DOI: https://doi.org/10.1016/j.jhydrol.2004.04.005.

French, H., C. Hardbattle, A. Binley, P. Winship & L. Jakobsen (2002). Monitoring snowmelt induced unsaturated flow and transport using electrical resistivity tomography. *Journal of Hydrology*, 267(3), 273 – 284. DOI: https://doi.org/10.1016/S0022-1694(02)00156-7.

Frey, K. E. & J. W. McClelland (2009). Impacts of permafrost degradation on arctic river biogeochemistry. *Hydrological Processes*, 23(1), 169–182. DOI: https://doi.org/10.1002/hyp.7196.

Frohlich, R. K. & C. D. Parke (1989). The electrical resistivity of the vadose zone — field survey. *Groundwater*, 27(4), 524–530. DOI: https://doi.org/10.1111/j.1745-6584.1989.tb01973.x.

Gao, Z., B. Tong, R. Horton, A. Mamtimin, Y. Li & L. Wang (2017). Determination of desert soil apparent thermal diffusivity using a conduction-convection algorithm. *Journal of Geophysical Research: Atmospheres*, 122(18), 9569–9578. DOI: https://doi.org/10.1002/2017JD027290.

Garré, S., M. Javaux, J. Vanderborght, L. Pagès & H. Vereecken (2011). Three-dimensional electrical resistivity tomography to monitor root zone water dynamics. *Vadose Zone Journal*, 10(1), 412–424. DOI: https://doi.org/10.2136/vzj2010.0079.

Garré, S., J. Koestel, T. Günther, M. Javaux, J. Vanderborght & H. Vereecken (2010). Comparison of Heterogeneous Transport Processes Observed with Electrical Resistivity Tomography in Two Soils. *Vadose Zone Journal*, 9(2), 336–349. DOI: 10.2136/vzj2009.0086.

Geuzaine, C. & J. F. Remacle (2009). Gmsh: A 3-d finite element mesh generator with built-in pre-and post-processing facilities. *International journal for numerical methods in engineering*, 79(11), 1309–1331.

Gleick, P., G. F. White, Pacific Institute for Studies in Development, Environment, and Security & Stockholm Environment Institute (1993). *Water in crisis : a guide to the world's fresh water resources*. Oxford University Press New York.

Glover, P. W. J. (2016). Archie's law – a reappraisal. *Solid Earth*, 7(4), 1157–1169. DOI: 10.5194/se-7-1157-2016.

Graham, D. E., M. D. Wallenstein, T. A. Vishnivetskaya, M. P. Waldrop, T. J. Phelps, S. M. Pfiffner, T. C. Onstott, L. G. Whyte, E. M. Rivkina, D. A. Gilichinsky, D. A. Elias, R. Mackelprang, N. C. VerBerkmoes, R. L. Hettich, D. Wagner, S. D. Wullschleger & J. K. Jansson (2012). Microbes in thawing permafrost: the unknown variable in the climate change equation. *The ISME Journal*, 6(4), 709–712.

Grenier, C., H. Anbergen, V. Bense, Q. Chanzy, E. Coon, N. Collier, F. Costard, M. Ferry, A. Frampton, J. Frederick, J. Gonçalvès, J. Holmén, A. Jost, S. Kokh, B. Kurylyk, J. McKenzie, J. Molson, E. Mouche, L. Orgogozo, R. Pannetier, A. Rivière, N. Roux, W. Rühaak, J. Scheidegger, J. O. Selroos, R. Therrien, P. Vidstrand & C. Voss (2018). Groundwater flow and heat transport for systems undergoing freeze-thaw: Intercomparison of numerical simulators for 2d test cases. *Advances in Water Resources*, 114, 196 – 218.

Grenier, C., D. Régnier, E. Mouche, H. Benabderrahmane, F. Costard & P. Davy (2013). Impact of permafrost development on groundwater flow patterns: a numerical study considering freezing cycles on a two-dimensional vertical cut through a generic river-plain system. *Hydrogeology Journal*, 21(1), 257–270.

Gupta, H. V., H. Kling, K. K. Yilmaz & G. F. Martinez (2009). Decomposition of the mean squared error and nse performance criteria: Implications for improving hydrological modelling. *Journal of Hydrology*, 377(1), 80 – 91.

Hamdhan, I. N. & B. G. Clarke (2010). Determination of thermal conductivity of coarse and fine sand soils. In *Proceedings of World Geothermal Congress*, pages 1–7.

Harp, D. R., A. L. Atchley, S. L. Painter, E. T. Coon, C. J. Wilson, V. E. Romanovsky & J. C. Rowland (2016). Effect of soil property uncertainties on permafrost thaw projections: a calibration-constrained analysis. *The Cryosphere*, 10(1), 341–358.

Hauck, C. (2002). Frozen ground monitoring using dc resistivity tomography. *Geophysical Research Letters*, 29(21), 12–1–12–4. doi: 10.1029/2002GL014995.

Hayashi, M. (2004). Temperature-electrical conductivity relation of water for environmental monitoring and geophysical data inversion. *Environmental monitoring and assessment*, 96(1), 119–128.

Hayashi, M., N. Goeller, W. L. Quinton & N. Wright (2007). A simple heat-conduction method for simulating the frost-table depth in hydrological models. *Hydrological Processes*, 21(19), 2610–2622. doi: https://doi.org/10.1002/hyp.6792.

Hayley, K., L. Bentley & A. Pidlisecky (2010). Compensating for temperature variations in time-lapse electrical resistivity difference imaging. *Geophysics*, 75(4), WA51–WA59.

Hayley, K., L. R. Bentley, M. Gharibi & M. Nightingale (2007). Low temperature dependence of electrical resistivity: Implications for near surface geophysical monitoring. *Geophysical Research Letters*, 34(18). doi: 10.1029/2007GL031124.

He, H., D. He, J. Jin, K. M. Smits, M. Dyck, Q. Wu, B. Si & J. Lv (2020). Room for improvement: A review and evaluation of 24 soil thermal conductivity parameterization schemes commonly used in land-surface, hydrological, and soil-vegetation-atmosphere transfer models. *Earth-Science Reviews*, 211, 103419. doi: https://doi.org/10.1016/j.earscirev.2020.103419.

Heijmans, M. M. P. D., R. Í. Magnússon, M. J. Lara, G. V. Frost, I. H. Myers-Smith, J. van Huissteden, M. T. Jorgenson, A. N. Fedorov, H. E. Epstein, D. M. Lawrence & J. Limpens (2022). Tundra vegetation change and impacts on permafrost. *Nature Reviews Earth & Environment*, pages 68–84.

Heiri, O., A. F. Lotter & G. Lemcke (2001). Loss on ignition as a method for estimating organic and carbonate content in sediments: reproducibility and comparability of results. *Journal of Paleolimnology*, 25, 101–110. doi: https://doi.org/10.1023/A:1008119611481.

Herring, T., E. Cey & A. Pidlisecky (2019). Electrical resistivity of a partially saturated porous medium at subzero temperatures. *Vadose Zone Journal*, 18(1), 1–11.

Herring, T., A. G. Lewkowicz, C. Hauck, C. Hilbich, C. Mollaret, G. A. Oldenborger, S. Uhlemann, M. Farzamian, F. Calmels & R. Scandroglio (2023). Best practices for using electrical

resistivity tomography to investigate permafrost. *Permafrost and Periglacial Processes*, 34(4), 494–512. DOI: https://doi.org/10.1002/ppp.2207.

Herring, T., A. Pidlisecky & E. Cey (2021). Removing the effects of temperature on electrical resistivity tomography data collected in partially frozen ground: Limitations and considerations for field applications. *Vadose Zone Journal*, 20(5), e20146. DOI: https://doi.org/10.1002/vzj2.20146.

Hilbich, C., C. Fuss & C. Hauck (2011). Automated time-lapse ert for improved process analysis and monitoring of frozen ground. *Permafrost and Periglacial Processes*, 22(4), 306–319. DOI: 10.1002/ppp.732.

Hinkel, K. M. (1997). Estimating seasonal values of thermal diffusivity in thawed and frozen soils using temperature time series. *Cold Regions Science and Technology*, 26(1), 1 – 15.

Hornum, M. T., P. Betlem & A. Hodson (2021). Groundwater flow through continuous permafrost along geological boundary revealed by electrical resistivity tomography. *Geophysical Research Letters*, 48(14). DOI: https://doi.org/10.1029/2021GL092757.

Hu, G., L. Zhao, R. Li, X. Wu, T. Wu, C. Xie, X. Zhu & Y. Su (2019). Variations in soil temperature from 1980 to 2015 in permafrost regions on the Qinghai-Tibetan Plateau based on observed and reanalysis products. *Geoderma*, 337, 893–905. DOI: https://doi.org/10.1016/j.geoderma.2018.10.044.

Hugelius, G. & P. Kuhry (2009). Landscape partitioning and environmental gradient analyses of soil organic carbon in a permafrost environment. *Global Biogeochemical Cycles*, 23(3). DOI: 10.1029/2008GB003419.

Hugelius, G., C. Tarnocai, G. Broll, J. G. Canadell, P. Kuhry & D. K. Swanson (2013). The northern circumpolar soil carbon database: spatially distributed datasets of soil coverage and soil carbon storage in the northern permafrost regions. *Earth System Science Data*, pages 3–13.

IPCC (2021). *Summary for Policymakers*, page 332. Cambridge University Press. DOI: 10.1017/9781009157896.001.

J. Brown, K. M. H. & F. E. Nelson (2000). The circumpolar active layer monitoring (calm) program: Research designs and initial results. *Polar Geography*, 24(3), 166–258.

Jafarov, E., S. Marchenko & V. E. Romanovsky (2012). Numerical modeling of permafrost dynamics in Alaska using a high spatial resolution dataset. *The Cryosphere*, 6, 613–624. DOI: 10.5194/tc-6-613-2012.

Jafarov, E. E., E. T. Coon, D. R. Harp, C. J. Wilson, S. L. Painter, A. L. Atchley & V. E. Romanovsky (2018). Modeling the role of preferential snow accumulation in through talik development and hillslope groundwater flow in a transitional permafrost landscape. *Environmental Research Letters*, 13(10).

Jakeman, A., R. Letcher & J. Norton (2006). Ten iterative steps in development and evaluation of environmental models. *Environmental Modelling & Software*, 21(5), 602 – 614.

Jiang, H., G. Zheng, Y. Yi, D. Chen, W. Zhang, K. Yang & C. E. Miller (2020). Progress and challenges in studying regional permafrost in the Tibetan Plateau using satellite remote sensing and models. *Frontiers in Earth Science*, 8.

Jin, H., R. He, G. Cheng, Q. Wu, S. Wang, L. Lü & X. Chang (2009). Changes in frozen ground in the source area of the Yellow River on the Qinghai Tibet Plateau, China, and their eco-environmental impacts. *Environmental Research Letters*, 4(4), 045206. DOI: 10.1088/1748-9326/4/4/045206.

Jobbágy, E. G. & R. B. Jackson (2000). The vertical distribution of soil organic carbon and its relation to climate and vegetation. *Ecological Applications*, 10(2), 423–436.

Kang, M. & J. Lee (2015). Evaluation of the freezing–thawing effect in sand–silt mixtures using elastic waves and electrical resistivity. *Cold Regions Science and Technology*, 113, 1–11. DOI: https://doi.org/

10.1016/j.coldregions.2015.02.004.

Keller, K., J. D. Blum & G. W. Kling (2010). Stream geochemistry as an indicator of increasing permafrost thaw depth in an Arctic watershed. *Chemical Geology*, 273(1), 76 – 81.

Kitover, D. C., R. T. van Balen, J. Vandenberghe, D. M. Roche & H. Renssen (2016). LGM permafrost thickness and extent in the Northern Hemisphere derived from the Earth system model iLOVECLIM. *Permafrost and Periglacial Processes*, 27(1), 31–42. doi: https://doi.org/10.1002/ppp.1861.

Kneisel, C., T. Rödder & D. Schwindt (2014). Frozen ground dynamics resolved by multi-year and year-round electrical resistivity monitoring at three alpine sites in the swiss alps. *Near Surface Geophysics*, 12(1), 117–132.

Knoben, W. J. M., J. E. Freer & R. A. Woods (2019). Technical note: Inherent benchmark or not? comparing Nash–Sutcliffe and Kling–Gupta efficiency scores. *Hydrology and Earth System Sciences*, 23(10), 4323–4331. doi: 10.5194/hess-23-4323-2019.

Koestel, J., A. Kemna, M. Javaux, A. Binley & H. Vereecken (2008). Quantitative imaging of solute transport in an unsaturated and undisturbed soil monolith with 3-d ert and tdr. *Water Resources Research*, 44(12). doi: 10.1029/2007WR006755.

Koestel, J., J. Vanderborght, M. Javaux, A. Kemna, A. Binley & H. Vereecken (2009). Noninvasive 3-D Transport Characterization in a Sandy Soil Using ERT: 1. Investigating the Validity of ERT-derived Transport Parameters. *Vadose Zone Journal*, 8(3), 711–722.

van der Kolk, H. J., M. M. Heijmans, J. van Huissteden, J. W. Pullens & F. Berendse (2016). Potential Arctic tundra vegetation shifts in response to changing temperature, precipitation and permafrost thaw. *Biogeosciences*, 13, 6229–6245.

Koven, C. D., D. M. Lawrence & W. J. Riley (2015). Permafrost carbon-climate feedback is sensitive to deep soil carbon decomposability but not deep soil nitrogen dynamics. *Proceedings of the National Academy of Sciences*, 112(12), 3752–3757. doi: 10.1073/pnas.1415123112.

Kozlowski, T. (2009). Some factors affecting supercooling and the equilibrium freezing point in soil–water systems. *Cold Regions Science and Technology*, 59(1), 25 – 33.

Krautblatter, M., S. Verleysdonk, A. Flores-Orozco & A. Kemna (2010). Temperature-calibrated imaging of seasonal changes in permafrost rock walls by quantitative electrical resistivity tomography (zugspitze, german/austrian alps). *Journal of Geophysical Research: Earth Surface*, 115(F2). doi: https://doi.org/10.1029/2008JF001209.

Kurylyk, B. L., M. Hayashi, W. L. Quinton, J. M. McKenzie & C. I. Voss (2016). Influence of vertical and lateral heat transfer on permafrost thaw, peatland landscape transition, and groundwater flow. *Water Resources Research*, 52(2), 1286–1305. doi: 10.1002/2015WR018057.

Kurylyk, B. L., J. M. McKenzie, K. T. MacQuarrie & C. I. Voss (2014). Analytical solutions for benchmarking cold regions subsurface water flow and energy transport models: One-dimensional soil thaw with conduction and advection. *Advances in Water Resources*, 70, 172 – 184.

Kurylyk, B. L. & K. Watanabe (2013). The mathematical representation of freezing and thawing processes in variably-saturated, non-deformable soils. *Advances in Water Resources*, 60, 160 – 177. doi: https://doi.org/10.1016/j.advwatres.2013.07.016.

LaBrecque, D. J., M. Miletto, W. Daily, A. Ramirez & E. Owen (1996). The effects of noise on occam's inversion of resistivity tomography data. *Geophysics*, 61(2), 538–548.

Lamontagne-Hallé, P., J. M. McKenzie, B. L. Kurylyk, J. Molson & L. N. Lyon (2020). Guidelines for cold-regions groundwater numerical modeling. *WIREs Water*, 7(6). doi: https://doi.org/10.1002/wat2.1467.

Lewis, J. & J. Sjöstrom (2010). Optimizing the experimental design of soil columns in saturated and unsaturated transport experiments. *Journal of Contaminant Hydrology*, 115(1), 1 – 13. doi: https://doi.org/10.1016/j.jconhyd.2010.04.001.

Li, J., Y. Sheng, J. Wu, Z. Feng, Z. Ning, X. Hu & X. Zhang (2016). Landform-related permafrost characteristics in the source area of the Yellow River, eastern Qinghai-Tibet Plateau. *Geomorphology*, 269, 104 – 111.

Lindgren, A., G. Hugelius, P. Kuhry, T. R. Christensen & J. Vandenberghe (2016). Gis-based maps and area estimates of Northern Hemisphere permafrost extent during the last glacial maximum. *Permafrost and Periglacial Processes*, pages 6–16. doi: 10.1002/ppp.1851.

Liu, L., R. S. Sletten, B. Hallet & E. D. Waddington (2018). Thermal regime and properties of soils and ice-rich permafrost in Beacon Valley, Antarctica. *Journal of Geophysical Research: Earth Surface*, 123(8), 1797–1810. doi: 10.1029/2017JF004535.

Liu, Q., S. Chen, L. Jiang, D. Wang, Z. Yang & L. Chen (2019). Determining thermal diffusivity using near-surface periodic temperature variations and its implications for tracing groundwater movement at the eastern margin of the Tibetan Plateau. *Hydrological Processes*, 33(8), 1276–1286. doi: https://doi.org/10.1002/hyp.13399.

Liu, R., C. Zhu, J. Schmalzel, D. Offenbacker, Y. Mehta, B. Barrowes, D. Glaser & W. Lein (2022). Experimental and numerical analyses of soil electrical resistivity under subfreezing conditions. *Journal of Applied Geophysics*, 202, 104671. doi: https://doi.org/10.1016/j.jappgeo.2022.104671.

Lunardini, V. (1985). Freezing of soil with phase change occurring over a finite temperature difference. In *Proceedings of the 4th international offshore mechanics and arctic engineering symposium. ASM*.

Luo, D., J. HuiJun, S. Marchenko & V. E. Romanovsky (2014). Distribution and changes of active layer thickness (ALT) and soil temperature (TTOP) in the source area of the Yellow River using the GIPL model. *Science China Earth Sciences*, 57(8), 1834–1845.

Luo, D., H. Jin, Q. Wu, V. F. Bense, R. He, Q. Ma, S. Gao, X. Jin & L. Lü (2018a). Thermal regime of warm-dry permafrost in relation to ground surface temperature in the source areas of the Yangtze and Yellow rivers on the Qinghai-Tibet Plateau, sw China. *Science of The Total Environment*, 618, 1033 – 1045.

Luo, D., H. J. Jin, R. X. He, X. F. Wang, R. R. Muskett, S. S. Marchenko & V. E. Romanovsky (2018b). Characteristics of water-heat exchanges and inconsistent surface temperature changes at an elevational permafrost site on the Qinghai-Tibet Plateau. *Journal of Geophysical Research: Atmospheres*, 123(18), 10,057–10,075. doi: 10.1029/2018JD028298.

Luo, D., Q. Wu, H. Jin, S. Marchenko, L. Lü & S. Gao (2016). Recent changes in the active layer thickness across the northern hemisphere. *Environmental Earth Sciences*, 75(7), 555.

Lyu, C., Q. Sun, W. Zhang & S. Hao (2019). Effects of nacl concentration on electrical resistivity of clay with cooling. *Journal of Applied Geophysics*, 170, 103843. doi: https://doi.org/10.1016/j.jappgeo.2019.103843.

Ma, Q., H. Jin, C. Yu & V. F. Bense (2019). Dissolved organic carbon in permafrost regions: A review. *Science China Earth Sciences*, 62, 349–364.

Mascarelli, A. (2009). A sleeping giant? *Nature Climate Change*, 1(904), 46–49.

McGuire, A. D., D. M. Lawrence, C. Koven, J. S. Clein, E. Burke, G. Chen, E. Jafarov, A. H. MacDougall, S. Marchenko, D. Nicolsky, S. Peng, A. Rinke, P. Ciais, I. Gouttevin, D. J. Hayes, D. Ji, G. Krinner, J. C. Moore, V. Romanovsky, C. Schädel, K. Schaefer, E. A. G. Schuur & Q. Zhuang (2018). Dependence of the evolution of carbon dynamics in the northern permafrost region on the

trajectory of climate change. *Proceedings of the National Academy of Sciences*, 115(15), 3882–3887.

McKenzie, J. M. & C. I. Voss (2013). Permafrost thaw in a nested groundwater-flow system. *Hydrogeology Journal*, 21(1), 299–316. doi: 10.1007/s10040-012-0942-3.

McKenzie, J. M., C. I. Voss & D. I. Siegel (2007). Groundwater flow with energy transport and water–ice phase change: Numerical simulations, benchmarks, and application to freezing in peat bogs. *Advances in Water Resources*, 30(4), 966 – 983. doi: https://doi.org/10.1016/j.advwatres.2006.08.008.

Melnikov, V. P., V. I. Osipov, A. V. Brouchkov, A. A. Falaleeva, S. V. Badina, M. N. Zheleznyak, M. R. Sadurtdinov, N. A. Ostrakov, D. S. Drozdov, A. B. Osokin, D. O. Sergeev, V. A. Dubrovin & R. Y. Fedorov (2022). Climate warming and permafrost thaw in the Russian Arctic: potential economic impacts on public infrastructure by 2050. *Natural Hazards*, 112, 231–251.

Midttømme, K. & E. Roaldset (1998). The effect of grain size on thermal conductivity of quartz sands and silts. *Petroleum Geoscience*, 4, 165–172. doi: 10.1144/petgeo.4.2.165.

Miesner, F., P. P. Overduin, G. Grosse, J. Strauss, M. Langer, S. Westermann, T. Schneider von Deimling, V. Brovkin & S. Arndt (2023). Subsea permafrost organic carbon stocks are large and of dominantly low reactivity. *Scientific Reports*, 13(1), 9425.

Miner, K. R., M. R. Turetsky, E. Malina, A. Bartsch, J. Tamminen, A. D. McGuire, A. Fix, C. Sweeney, C. D. Elder & C. E. Miller (2022). Permafrost carbon emissions in a changing Arctic. *Nature Reviews Earth & Environment*, 3(1), 55–67.

Mohammed, A. A., V. F. Bense, B. L. Kurylyk, R. C. Jamieson, L. H. Johnston & A. J. Jackson (2021). Modeling reactive solute transport in permafrost-affected groundwater systems. *Water Resources Research*, 57(7), e2020WR028771. doi: https://doi.org/10.1029/2020WR028771.

Mohammed, A. A., J. A. Guimond, V. F. Bense, R. C. Jamieson, J. M. McKenzie & B. L. Kurylyk (2022). Mobilization of subsurface carbon pools driven by permafrost thaw and reactivation of groundwater flow: a virtual experiment. *Environmental Research Letters*, 17(12).

Mohammed, A. A., R. A. Schincariol, R. M. Nagare & W. L. Quinton (2014). Reproducing field-scale active layer thaw in the laboratory. *Vadose Zone Journal*, 13(8), 01–09.

Mondav, R., C. K. McCalley, S. B. Hodgkins, S. Frolking, S. R. Saleska, V. I. Rich, J. P. Chanton & P. M. Crill (2017). Microbial network, phylogenetic diversity and community membership in the active layer across a permafrost thaw gradient. *Environmental Microbiology*, 19(8), 3201–3218. doi: 10.1111/1462-2920.13809.

Mu, C., T. Zhang, X. Zhang, B. Cao & X. Peng (2016). Sensitivity of soil organic matter decomposition to temperature at different depths in permafrost regions on the northern qinghai-tibet plateau. *European Journal of Soil Science*, 67(6), 773–781. doi: 10.1111/ejss.12386.

Mustamo, P., A. K. Ronkanen, Örjan Berglund, K. Berglund & B. Kløve (2019). Thermal conductivity of unfrozen and partially frozen managed peat soils. *Soil and Tillage Research*, 191, 245 – 255.

Nagare, R. M., P. Bhattacharya, J. Khanna & R. A. Schincariol (2015). Coupled cellular automata for frozen soil processes. *SOIL*, 1(1), 103–116. doi: 10.5194/soil-1-103-2015.

Nagare, R. M., R. A. Schincariol, W. L. Quinton & M. Hayashi (2012a). Effects of freezing on soil temperature, freezing front propagation and moisture redistribution in peat: laboratory investigations. *Hydrology and Earth System Sciences*, 16(2), 501–515. doi: 10.5194/hess-16-501-2012.

Nagare, R. M., R. A. Schincariol, W. L. Quinton & M. Hayashi (2012b). Moving the field into the lab: Simulation of water and heat transport in subarctic peat. *Permafrost and Periglacial Processes*, 23(3), 237–243. doi: 10.1002/ppp.1746.

Nan, Z., S. Li & G. Cheng (2005). Prediction of permafrost distribution on the Qinghai-Tibet Plateau

in the next 50 and 100 years. *Science in China Series D: Earth Sciences*, 48, 797 – 804. DOI: 10.1360/03yd0258.

Nelson, M. (2020). Pdesolutions.

Nita, I. A., L. Sfîcă, M. Voiculescu, M. V. Birsan & M. M. Micheu (2022). Changes in the global mean air temperature over land since 1980. *Atmospheric Research*, 279.

Obu, J. (2021). How much of the Earth's surface is underlain by permafrost? *Journal of Geophysical Research: Earth Surface*, 126(5). DOI: https://doi.org/10.1029/2021JF006123.

Oldenborger, G. A. (2021). Subzero temperature dependence of electrical conductivity for permafrost geophysics. *Cold Regions Science and Technology*, 182, 103214. DOI: https://doi.org/10.1016/j.coldregions.2020.103214.

Oldenborger, G. A. & A. M. LeBlanc (2018). Monitoring changes in unfrozen water content with electrical resistivity surveys in cold continuous permafrost. *Geophysical Journal International*, 215(2), 965–977. DOI: 10.1093/gji/ggy321.

Overduin, P., D. Kane & W. van Loon (2006). Measuring thermal conductivity in freezing and thawing soil using the soil temperature response to heating. *Cold Regions Science and Technology*, 45(1), 8 – 22.

O'Donnell, J. A., M. T. Jorgenson, J. W. Harden, A. D. McGuire, M. Z. Kanevskiy & K. P. Wickland (2012). The effects of permafrost thaw on soil hydrologic, thermal, and carbon dynamics in an Alaskan peatland. *Ecosystems*, 15(2), 213–229.

Pardo Lara, R., A. A. Berg, J. Warland & G. Parkin (2021). Implications of measurement metrics on soil freezing curves: A simulation of freeze–thaw hysteresis. *Hydrological Processes*, 35(7). DOI: https://doi.org/10.1002/hyp.14269.

Patzner, M. S., C. W. Mueller, M. Malusova, M. Baur, V. Nikeleit, T. Scholten, C. Hoeschen, J. M. Byrne, T. Borch, A. Kappler et al. (2020). Iron mineral dissolution releases iron and associated organic carbon during permafrost thaw. *Nature communications*, 11(1), 1–11.

Penghao, C., L. Pingkuo & P. Hua (2019). Prospects of hydropower industry in the Yangtze River basin: China's green energy choice. *Renewable Energy*, 131, 1168–1185.

Previdi, M., K. L. Smith & L. M. Polvani (2021). Arctic amplification of climate change: a review of underlying mechanisms. *Environmental Research Letters*, 16(9).

Prowse, T. D., F. J. Wrona, J. D. Reist, J. J. Gibson, J. E. Hobbie, L. M. J. Lévesque & W. F. Vincent (2006). Climate Change Effects on Hydroecology of Arctic Freshwater Ecosystems. *AMBIO: A Journal of the Human Environment*, 35(7), 347 – 358. DOI: 10.1579/0044-7447(2006)35[347:CCEOHO]2.0.CO;2.

Putkonen, J. (1998). Soil thermal processes and heat transfer processes near Ny-Ålesund, northwestern Spitsbergen, Svalbard. *Polar Research*, 17(2), 165–179. DOI: 10.3402/polar.v17i2.6617.

Qin, Y., T. Wu, L. Zhao, X. Wu, R. Li, C. Xie, Q. Pang, G. Hu, Y. Qiao, G. Zhao, G. Liu, X. Zhu & J. Hao (2017). Numerical modeling of the active layer thickness and permafrost thermal state across Qinghai-Tibetan Plateau. *Journal of Geophysical Research: Atmospheres*, 122(21), 11,604–11,620. DOI: 10.1002/2017JD026858.

Ran, Y., X. Li, G. Cheng, Z. Nan, J. Che, Y. Sheng, Q. Wu, H. Jin, D. Luo, Z. Tang & X. Wu (2021). Mapping the permafrost stability on the Tibetan Plateau for 2005–2015. *Science China Earth Sciences*, 64, 62–79.

Rantanen, M., A. Y. Karpechko, A. Lipponen, K. Nordling, O. Hyvärinen, K. Ruosteenoja, T. Vihma & A. Laaksonen (2022). The arctic has warmed nearly four times faster than the globe since 1979. *Communications Earth & Environment*, 3(1), 168.

Ren, J. & S. K.Vanapalli (2019). Comparison of soil-freezing and soil-water characteristic curves of two canadian soils. *Vadose Zone Journal*, 18.

Ren, J., S. Vanapalli & Z. Han (2017). Soil freezing process and different expressions for the soil-freezing characteristic curve. *Sciences in Cold and Arid Regions*, 9, 221–228. doi: 10.3724/SP.J.1226.2017.00221.

Ren, J. & S. K. Vanapalli (2020). Effect of freeze–thaw cycling on the soil-freezing characteristic curve of five canadian soils. *Vadose Zone Journal*, 19(1). doi: https://doi.org/10.1002/vzj2.20039.

Rokaya, A. & J. Kim (2018). An accurate analysis for sandwich steel beams with graded corrugated core under dynamic impulse. *International Journal of Steel Structures*, 18(5), 1541–1559. doi: 10.1007/s13296-018-0062-6.

Romanovsky, V. E., M. Burgess, S. Smith, K. Yoshikawa & J. Brown (2002). Permafrost temperature records: Indicators of climate change. *Eos, Transactions American Geophysical Union*, 83(50), 589–594. doi: https://doi.org/10.1029/2002EO000402.

Romanovsky, V. E. & T. E. Osterkamp (2000). Effects of unfrozen water on heat and mass transport processes in the active layer and permafrost. *Permafrost and Periglacial Processes*, 11(3), 219–239. doi: 10.1002/1099-1530(200007/09)11:3<219::AID-PPP352>3.0.CO;2-7.

Rowland, J. C., B. J. Travis & C. J. Wilson (2011). The role of advective heat transport in talik development beneath lakes and ponds in discontinuous permafrost. *Geophysical Research Letters*, 38(17). doi: https://doi.org/10.1029/2011GL048497.

Russell, D. (1997). Error measures for comparing transient data : Part i : Development of a comprehensive error measure part ii : Error measures case study.

Saberi, P. S. & G. Meschke (2021). A hysteresis model for the unfrozen liquid content in freezing porous media. *Computers and Geotechnics*, 134, 104048.

Schaefer, K., H. Lantuit, V. E. Romanovsky, E. A. G. Schuur & R. Witt (2014). The impact of the permafrost carbon feedback on global climate. *Environmental Research Letters*, 9.

Schaefer, K., T. Zhang, L. Bruhwiler & A. P. Barrett (2011). Amount and timing of permafrost carbon release in response to climate warming. *Tellus B: Chemical and Physical Meteorology*, 63(2), 168–180. doi: 10.1111/j.1600-0889.2010.00527.x.

Schaphoff, S., U. Heyder, S. Ostberg, D. Gerten, J. Heinke & W. Lucht (2013). Contribution of permafrost soils to the global carbon budget. *Environmental Research Letters*, 8(1).

Scheidegger, J. & V. Bense (2014). Impacts of glacially recharged groundwater flow systems on talik evolution. *Journal of Geophysical Research: Earth Surface*, 119.

Scherler, M., C. Hauck, M. Hoelzle, M. Stähli & I. Völksch (2010). Meltwater infiltration into the frozen active layer at an alpine permafrost site. *Permafrost and Periglacial Processes*, 21(4), 325–334. doi: 10.1002/ppp.694.

Schuster, P. F., K. M. Schaefer, G. R. Aiken, R. C. Antweiler, J. F. Dewild, J. D. Gryziec, A. Gusmeroli, G. Hugelius, E. Jafarov, D. P. Krabbenhoft, L. Liu, N. Herman-Mercer, C. Mu, D. A. Roth, T. Schaefer, R. G. Striegl, K. P. Wickland & T. Zhang (2018). Permafrost stores a globally significant amount of mercury. *Geophysical Research Letters*, 45(3), 1463–1471. doi: https://doi.org/10.1002/2017GL075571.

Schuur, E. A. G., J. Bockheim, J. G. Canadell, E. Euskirchen, C. B. Field, S. V. Goryachkin, S. Hagemann, P. Kuhry, P. M. Lafleur, H. Lee, G. Mazhitova, F. E. Nelson, A. Rinke, V. E. Romanovsky, N. Shiklomanov, C. Tarnocai, S. Venevsky, J. G. Vogel & S. A. Zimov (2008). Vulnerability of Permafrost Carbon to Climate Change: Implications for the Global Carbon Cycle. *BioScience*, 58, 701–714.

doi: 10.1641/B580807.

Schuur, E. A. G., A. D. McGuire, C. Schädel, G. Grosse, J. W. Harden, D. J. Hayes, G. Hugelius, C. D. Koven, P. Kuhry, D. M. Lawrence, S. M. Natali, D. Olefeldt, V. E. Romanovsky, K. Schaefer, M. R. Turetsky, C. C. Treat & J. E. Vonk (2015). Climate change and the permafrost carbon feedback. *Nature*, 520, 171.

Schuur, E. A. G., J. G. Vogel, K. G. Crummer, H. Lee, J. O. Sickman & T. E. Osterkamp (2009). The effect of permafrost thaw on old carbon release and net carbon exchange from tundra. *Nature*, 459, 556–559. doi: 10.1038/nature08031.

Shijin, W., Q. Wenli & L. Qiaoxia (2023). Key pathways to achieve sustainable development goals in three polar regions. *Sustainability*, 15(2).

Siegert, C., L. Schirrmeister & O. Babiy (2002). The sedimentological, mineralogical and geochemical composition of late pleistocene deposits from the ice complex on the bykovsky peninsula, northern siberia. *Polarforschung, 70*, 2000, 3–11.

Sjöberg, Y., E. Coon, A. B. K. Sannel, R. Pannetier, D. Harp, A. Frampton, S. L. Painter & S. W. Lyon (2016). Thermal effects of groundwater flow through subarctic fens: A case study based on field observations and numerical modeling. *Water Resources Research*, 52(3), 1591–1606. doi: 10.1002/2015WR017571.

Sjöberg, Y., A. Jan, S. L. Painter, E. T. Coon, M. P. Carey, J. A. O'Donnell & J. C. Koch (2021). Permafrost promotes shallow groundwater flow and warmer headwater streams. *Water Resources Research*.

Slater, L., A. Binley, W. Daily & R. Johnson (2000). Cross-hole electrical imaging of a controlled saline tracer injection. *Journal of Applied Geophysics*, 44(2), 85–102. doi: https://doi.org/10.1016/S0926-9851(00)00002-1.

Slater, L., A. Binley, R. Versteeg, G. Cassiani, R. Birken & S. Sandberg (2002). A 3d ert study of solute transport in a large experimental tank. *Journal of Applied Geophysics*, 49(4), 211 – 229. doi: https://doi.org/10.1016/S0926-9851(02)00124-6.

Smits, K. M., T. Sakaki, A. Limsuwat & T. H. Illangasekare (2010). Thermal conductivity of sands under varying moisture and porosity in drainage–wetting cycles. *Vadose Zone Journal*, 9(1), 172–180. doi: 10.2136/vzj2009.0095.

Song, C., G. Wang, T. Mao, J. Dai & D. Yang (2020). Linkage between permafrost distribution and river runoff changes across the arctic and the tibetan plateau. *Science China Earth Sciences*, 63, 292–302.

Stevens, M. B., J. E. Smerdon, J. F. González-Rouco, M. Stieglitz & H. Beltrami (2007). Effects of bottom boundary placement on subsurface heat storage: Implications for climate model simulations. *Geophysical Research Letters*, 34(2). doi: https://doi.org/10.1029/2006GL028546.

Strauss, J., L. Schirrmeister, G. Grosse, D. Fortier, G. Hugelius, C. Knoblauch, V. Romanovsky, C. Schädel, T. S. von Deimling, E. A. Schuur, D. Shmelev, M. Ulrich & A. Veremeeva (2017). Deep yedoma permafrost: A synthesis of depositional characteristics and carbon vulnerability. *Earth-Science Reviews*, 172, 75 – 86.

Strauss, J., L. Schirrmeister, G. Grosse, S. Wetterich, M. Ulrich, U. Herzschuh & H. W. Hubberten (2013). The deep permafrost carbon pool of the yedoma region in siberia and alaska. *Geophysical Research Letters*, 40(23), 6165–6170. doi: 10.1002/2013GL058088.

Strauss, J., L. Schirrmeister, S. Wetterich, A. Borchers & S. P. Davydov (2012). Grain-size properties and organic-carbon stock of yedoma ice complex permafrost from the kolyma lowland, northeastern siberia. *Global Biogeochemical Cycles*, 26(3). doi: 10.1029/2011GB004104.

Sun, A., Z. Yu, J. Zhou, K. Acharya, Q. Ju, R. Xing, D. Huang & L. Wen (2020a). Quantified hydro-

logical responses to permafrost degradation in the headwaters of the Yellow River (HWYR) in high Asia. *Science of The Total Environment*, 712, 135632.

Sun, Z., L. Zhao, G. Hu, Y. Qiao, E. Du, D. Zou & C. Xie (2020b). Modeling permafrost changes on the Qinghai–Tibetan Plateau from 1966 to 2100: A case study from two boreholes along the Qinghai–Tibet engineering corridor. *Permafrost and Periglacial Processes*, 31(1), 156–171. doi: https://doi.org/10.1002/ppp.2022.

Tang, L., X. Wang, F. Lan, P. Qiu & L. Jin (2020). Measuring the content of unfrozen water in frozen soil based on resistivity. *Int. J. Electrochem. Sci*, 15, 9459–9472.

Tarnocai, C., J. G. Canadell, E. A. G. Schuur, P. Kuhry, G. Mazhitova & S. Zimov (2009). Soil organic carbon pools in the northern circumpolar permafrost region. *Global Biogeochemical Cycles*, 23(2).

Tian, H., C. Wei, Y. Lai & P. Chen (2018). Quantification of water content during freeze–thaw cycles: A nuclear magnetic resonance based method. *Vadose Zone Journal*, 17(1), 160124. doi: https://doi.org/10.2136/vzj2016.12.0124.

Tian, H., C. Wei, H. Wei & J. Zhou (2014). Freezing and thawing characteristics of frozen soils: Bound water content and hysteresis phenomenon. *Cold Regions Science and Technology*, 103, 74–81.

Tomaškovičová, S. & T. Ingeman-Nielsen (2023). Quantification of freeze–thaw hysteresis of unfrozen water content and electrical resistivity from time lapse measurements in the active layer and permafrost. *Permafrost and Periglacial Processes*, page 19. doi: https://doi.org/10.1002/ppp.2201.

Tomaškovičová, S., T. Ingeman-Nielsen, A. V. Christiansen, I. Brandt, T. Dahlin & B. Elberling (2016). Effect of electrode shape on grounding resistances — part 2: Experimental results and cryospheric monitoring. *Geophysics*, 81(1), WA169–WA182. doi: 10.1190/geo2015-0148.1.

Toohey, R. C., N. M. Herman-Mercer, P. F. Schuster, E. A. Mutter & J. C. Koch (2016). Multidecadal increases in the Yukon River basin of chemical fluxes as indicators of changing flowpaths, groundwater, and permafrost. *Geophysical Research Letters*, 43(23), 12,120–12,130. doi: https://doi.org/10.1002/2016GL070817.

Truffert, C. (2022). Iris instruments. http://www.iris-instruments.com.

Turetsky, M. R., B. W. Abbott, M. C. Jones, K. W. Anthony, D. Olefeldt, E. A. G. Schuur, G. Grosse, P. Kuhry, G. Hugelius, C. Koven, D. M. Lawrence, C. Gibson, A. B. K. Sannel & A. D. McGuire (2020). Carbon release through abrupt permafrost thaw. *Nature Geoscience*, 13, 138–143.

Van Everdingen, R. O., I. P. Association et al. (1998). *Multi-language glossary of permafrost and related ground-ice terms*. Arctic Inst. of North America University of Calgary.

Van Huissteden, J. (2020). *Thawing permafrost*, volume 1143. Springer.

Vardy, S. R., B. G. Warner, J. Turunen & R. Aravena (2000). Carbon accumulation in permafrost peatlands in the northwest territories and nunavut, canada. *The Holocene*, 10(2), 273–280. doi: 10.1191/095968300671749538.

Vonk, J. E., P. J. Mann, S. Davydov, A. Davydova, R. G. M. Spencer, J. Schade, W. V. Sobczak, N. Zimov, S. Zimov, E. Bulygina, T. I. Eglinton & R. M. Holmes (2013a). High biolability of ancient permafrost carbon upon thaw. *Geophysical Research Letters*, 40(11), 2689–2693. doi: 10.1002/grl.50348.

Vonk, J. E., P. J. Mann, K. L. Dowdy, A. Davydova, S. P. Davydov, N. Zimov, R. G. M. Spencer, E. B. Bulygina, T. I. Eglinton & R. M. Holmes (2013b). Dissolved organic carbon loss from Yedoma permafrost amplified by ice wedge thaw. *Environmental Research Letters*, 8(3).

Vonk, J. E., S. E. Tank, W. B. Bowden, I. Laurion, W. F. Vincent, P. Alekseychik, M. Amyot, M. F. Billet, J. Canario, R. M. Cory, B. N. Deshpande, M. Helbig, M. Jammet, J. Karlsson, J. Larouche, G. MacMillan, M. Rautio, K. M. W. Anthony & K. P. Wickland (2015). Reviews and syntheses

: Effects of permafrost thaw on Arctic aquatic ecosystems. *Biogeosciences*, 12(23), 7129–7167. DOI: 10.5194/bg-12-7129-2015.

Vonk, J. E., S. E. Tank & M. A. Walvoord (2019). Integrating hydrology and biogeochemistry across frozen landscapes. *Nature Communications*, 10. DOI: 10.1038/s41467-019-13361-5.

Väliranta, M., M. E. Marushchak, J. P. Tuovinen, A. Lohila, C. Biasi, C. Voigt, H. Zhang, S. Piilo, T. Virtanen, A. Räsänen, D. Kaverin, A. Pastukhov, A. B. K. Sannel, E. S. Tuittila, A. Korhola & P. J. Martikainen (2021). Warming climate forcing impact from a sub-arctic peatland as a result of late Holocene permafrost aggradation and initiation of bare peat surfaces. *Quaternary Science Reviews*, 264.

Walvoord, M. A. & B. L. Kurylyk (2016). Hydrologic impacts of thawing permafrost—a review. *Vadose Zone Journal*, 15(6).

Walvoord, M. A. & R. G. Striegl (2007). Increased groundwater to stream discharge from permafrost thawing in the Yukon River basin: Potential impacts on lateral export of carbon and nitrogen. *Geophysical Research Letters*, 34(12). DOI: 10.1029/2007GL030216.

Walvoord, M. A. & R. G. Striegl (2021). Complex vulnerabilities of the water and aquatic carbon cycles to permafrost thaw. *Frontiers in Climate*, 3. DOI: 10.3389/fclim.2021.730402.

Walvoord, M. A., C. I. Voss, B. A. Ebel & B. J. Minsley (2019). Development of perennial thaw zones in boreal hillslopes enhances potential mobilization of permafrost carbon. *Environmental Research Letters*, 14(1).

Walvoord, M. A., C. I. Voss & T. P. Wellman (2012). Influence of permafrost distribution on groundwater flow in the context of climate-driven permafrost thaw: Example from Yukon flats basin, Alaska, United States. *Water Resources Research*, 48(7). DOI: 10.1029/2011WR011595.

Walz, J., C. Knoblauch, L. Böhme & E. M. Pfeiffer (2017). Regulation of soil organic matter decomposition in permafrost-affected siberian tundra soils - impact of oxygen availability, freezing and thawing, temperature, and labile organic matter. *Soil Biology and Biochemistry*, 110, 34 – 43.

Wang, G., Y. Wang, Y. Li & H. Cheng (2007). Influences of alpine ecosystem responses to climatic change on soil properties on the Qinghai–Tibet Plateau, China. *CATENA*, 70(3), 506 – 514.

Wang, T., D. Yang, Y. Yang, S. Piao, X. Li, G. Cheng & B. Fu (2020). Permafrost thawing puts the frozen carbon at risk over the Tibetan Plateau. *Science Advances*, 6(19). DOI: 10.1126/sciadv.aaz3513.

Wang, T., D. Yang, Y. Yang, G. Zheng, H. Jin, X. Li, T. Yao & G. Cheng (2023). Pervasive permafrost thaw exacerbates future risk of water shortage across the Tibetan Plateau. *Earth's Future*, 11(10).

Wang, T., G. Zhou, X. Jiang & J. Wang (2018a). Assessment for the spatial variation characteristics of uncertain thermal parameters for warm frozen soil. *Applied Thermal Engineering*, 134, 484–489.

Wang, Y., Y. Xu, R. G. M. Spencer, P. Zito, A. Kellerman, D. Podgorski, W. Xiao, D. Wei, H. Rashid & Y. Yang (2018b). Selective leaching of dissolved organic matter from alpine permafrost soils on the Qinghai-Tibetan Plateau. *Journal of Geophysical Research: Biogeosciences*, 123(3), 1005–1016.

Watanabe, K., T. Kito, T. Wake & M. Sakai (2011). Freezing experiments on unsaturated sand, loam and silt loam. *Annals of Glaciology*, 52(58), 37–43.

Westerveld, L. (2023). Organic carbon in permafrost.

Wild, B., A. Andersson, L. Bröder, J. Vonk, G. Hugelius, J. W. McClelland, W. Song, P. A. Raymond & Ö. Gustafsson (2019). Rivers across the siberian arctic unearth the patterns of carbon release from thawing permafrost. *Proceedings of the National Academy of Sciences*, 116(21), 10280–10285.

Wilke, B. M. (2005). *Determination of Chemical and Physical Soil Properties*, pages 47–95. Springer Berlin

Heidelberg.

Winsauer, W. O., J. Shearin, H. M., P. H. Masson & M. Williams (1952). Resistivity of brine-saturated sands in relation to pore geometry1. *AAPG Bulletin*, 36(2), 253–277. doi: 10.1306/3D9343F4-16B1-11D7-8645000102C1865D.

Wu, Q., Y. Hou, H. Yun & Y. Liu (2015). Changes in active-layer thickness and near-surface permafrost between 2002 and 2012 in alpine ecosystems, Qinghai–Xizang (Tibet) Plateau, China. *Global and Planetary Change*, 124, 149 – 155.

Wu, Q. & T. Zhang (2008). Recent permafrost warming on the Qinghai-Tibetan Plateau. *Journal of Geophysical Research: Atmospheres*, 113(D13). doi: 10.1029/2007JD009539.

Wu, Q., T. Zhang & Y. Liu (2010). Permafrost temperatures and thickness on the Qinghai-Tibet Plateau. *Global and Planetary Change*, 72(1), 32 – 38.

Wu, Q., T. Zhang & Y. Liu (2012). Thermal state of the active layer and permafrost along the Qinghai-Xizang (Tibet) railway from 2006 to 2010. *The Cryosphere*, 6(3), 607–612.

Wu, Y., S. Nakagawa, T. J. Kneafsey, B. Dafflon & S. Hubbard (2017). Electrical and seismic response of saline permafrost soil during freeze - thaw transition. *Journal of Applied Geophysics*, 146, 16–26. doi: https://doi.org/10.1016/j.jappgeo.2017.08.008.

Yang, S., R. Li, T. Wu, X. Wu, L. Zhao, G. Hu, X. Zhu, Y. Du, Y. Xiao, Y. Zhang, J. Ma, E. Du, J. Shi & Y. Qiao (2021). Evaluation of soil thermal conductivity schemes incorporated into clm5.0 in permafrost regions on the tibetan plateau. *Geoderma*, 401, 115330. doi: https://doi.org/10.1016/j.geoderma.2021.115330.

Ye, B., D. Yang, Z. Zhang & D. L. Kane (2009). Variation of hydrological regime with permafrost coverage over lena basin in siberia. *Journal of Geophysical Research: Atmospheres*, 114.

Zhang, G., Z. Nan, N. Hu, Z. Yin, L. Zhao, G. Cheng & C. Mu (2022). Qinghai-Tibet Plateau permafrost at risk in the late 21st century. *Earth's Future*, 10(6).

Zhang, M., J. Lu, Y. Lai & X. Zhang (2018). Variation of the thermal conductivity of a silty clay during a freezing-thawing process. *International Journal of Heat and Mass Transfer*, 124, 1059–1067. doi: https://doi.org/10.1016/j.ijheatmasstransfer.2018.02.118.

Zhang, M., X. Zhang, Y. Lai, J. Lu & C. Wang (2020). Variations of the temperatures and volumetric unfrozen water contents of fine-grained soils during a freezing–thawing process. *Acta Geotechnica*, 15(3), 595–601.

Zhao, D., X. Qian, X. Gu, S. A. Jajja & R. Yang (2016). Measurement techniques for thermal conductivity and interfacial thermal conductance of bulk and thin film materials. *Journal of Electronic Packaging*, 138(4).

Zhao, H., Y. Zeng, S. Lv & Z. Su (2018). Analysis of soil hydraulic and thermal properties for land surface modeling over the Tibetan Plateau. *Earth System Science Data*, 10(2), 1031–1061. doi: 10.5194/essd-10-1031-2018.

Zhao, S., Z. T. Nan, Y. B. Huang & L. Zhao (2017). The application and evaluation of simple permafrost distribution models on the Qinghai–Tibet Plateau. *Permafrost and Periglacial Processes*, 28(2), 391–404. doi: https://doi.org/10.1002/ppp.1939.

Zhao, Y. & Z. J. Yang (2022). Historical and long-term climate trends in warm permafrost regions: A case study of bethel, ak. *Cold Regions Science and Technology*, 204, 103677. doi: https://doi.org/10.1016/j.coldregions.2022.103677.

Zhou, J., J. Heitman, R. Horton, T. Ren, T. Ochsner, L. Prunty, R. Ewing & T. Sauer (2006). Method for maintaining one-dimensional temperature gradients in unsaturated, closed soil cells. *Soil Science*

Society of America Journal, 70(4), 1303–1309.

Zimov, S. A., S. P. Davydov, G. M. Zimova, A. I. Davydova, E. A. G. Schuur, K. Dutta & F. S. Chapin III (2006). Permafrost carbon: Stock and decomposability of a globally significant carbon pool. *Geophysical Research Letters*, 33(20). doi: 10.1029/2006GL027484.

Zou, D., L. Zhao, Y. Sheng, J. Chen, G. Hu, T. Wu, J. Wu, C. Xie, X. Wu, Q. Pang, W. Wang, E. Du, W. Li, G. Liu, J. Li, Y. Qin, Y. Qiao, Z. Wang, J. Shi & G. Cheng (2017). A new map of permafrost distribution on the Tibetan Plateau. *The Cryosphere*, 11(6), 2527–2542.

Statement of authorship contribution

The general direction of the research was developed by my promotor and co-promotor, in response to a clear knowledge gap in the current understanding and modelling capability of permafrost freeze-thaw processes and associated emergence of groundwater flow. Based upon the research proposal, I created the research plan and formulated the research questions. I conceptualised the experimental designs and created functional designs in collaboration with the help of our technical department. I wrote the introduction in Chapter 1 and synthesis Chapter 5, with minor suggestions from my (co-)promotors. Chapters 2 to 4 are the result of a collaboration between the authors listed here. Each of their relative contributions are indicated per chapter below.

JB = Jelte de Bruin (WUR)

VB = Victor Bense (WUR)
MP = Martine van der Ploeg (WUR)
AB = Andrew Binley (Lancaster University)

Chapter 2

Conceptualisation of the work:	JB, MP, VB
Data collection:	JB
Modelling, data analysis and interpretation:	JB in consultation with MP, VB
Drafting of manuscript:	JB
Revision of the article and approval for publishing:	JB, MP, VB

Chapter 3

Conceptualisation of the work:	JB, MP, VB
Data collection:	JB
Modelling, data analysis and interpretation:	JB in consultation with MP, VB
Drafting of manuscript:	JB
Revision of the article and approval for publishing:	JB, MP, VB

Chapter 4

Conceptualisation of the work:	JB, MP, VB
Data collection:	JB
Modelling, data analysis and interpretation:	JB in consultation with AB, MP, VB
Drafting of manuscript:	JB
Revision of the article and approval for publishing:	AB, JB, MP, VB

Summary

Permafrost covers vast parts of the Earths surface near the poles. These permafrost areas stretch over a wide range of landscapes, from frozen tundra's and boreal forests to peat rich areas. However, due to the global increase in annual air temperatures, the thawing of permafrost changed, subsequently changing the dynamics of the area. The top layer of the permafrost, the active layer, seasonally freezes and thaws. As permafrost thaws, organic matter embedded within the soil starts to be decomposed by bacteria, releasing the greenhouse gasses carbon dioxide (CO_2) and methane (CH_4) into the atmosphere. Permafrost thaw and subsequent release of greenhouse gasses thereby amplifies the global warming effect. Considering that over one-third of the global organic matter is stored within permafrost, an enormous amount of organic matter could become part of the active global carbon cycle. On a global scale, an increase in greenhouse gasses release and subsequent air temperature increase has an enormous effect on for example predicted sea level rise. At a local scale, this has the potential to significantly impact society, as infrastructure becomes unstable due to the thawing active-layer. A profound understanding of the fundamental processes involved in permafrost dynamics is therefore crucial.

Permafrost dynamics are studied using numerical models that simulate how energy in the form of temperature freezes and thaws the soil. Using these models, we can simulate how the active layer freezes and thaws under various climate scenarios. However, we need to parameterise the numerical models accurately to simulate the dynamics at various locations with different soil types and different landscapes. The numerical models therefore rely on information of the thermal properties of the subsurface, and soil physical properties, such as the porosity, grain size and water content. Using these properties, in combination with temperature observations collected at various depths in the permafrost, we can calibrate our numerical model and perform the simulations. However, not all of these crucial data is always available, since it is difficult to collect. Typically, standard ranges of thermal properties are used that are available in literature. However, these are often not representative for the actual field location. Hence, we need alternative ways to calibrate the numerical models using the available data.

In **Chapter 2** we demonstrate a method to calibrate a numerical heat transport model relying only on temperature observations from a field site located at the Qinghai-Tibetan Plateau (QTP). Using a 1D heat transport model simulating temperature at various depths within the permafrost, three parameters affecting the heat transport characteristics of the permafrost, namely the thermal conductivity, heat capacity and porosity were varied. Using a statistical analysis, the optimal parameter combination

was determined that best simulated the observed temperature dynamics. Due to the non-linear relations between the thermal properties and porosity, multiple parameter combinations showed good fits to the data. A comparative study was conducted, comparing three different ways to evaluate data fit. First evaluate the misfit in magnitude, second the misfit in timing and thirdly a combination of both. Results showed that it was possible to determine the thermal properties from temperature observations, but that the optimal parameter combinations was dependent on the evaluation criteria. A subsequent 100-year simulation of the development of the active-layer, using the three optimal parameter combinations showed significant differences in thawing depths. Even though human decision making was not a part of the selection process for the best fitting parameters, choices regarding the evaluation criteria did have a large impact on the selection of optimal parameters.

While it was proven that the thermal properties of permafrost could be determined using solely temperature observations, the next goal was to determine if there was a clear relation between various soil properties and the thermal properties and if it could be determined using a numerical heat transport model. In **Chapter 3** we show how laboratory experiments were used to provide ranges for thermal properties for various grain sizes and organic matter contents. A total of nine soil columns with varying grain sizes and organic matter contents were gradually frozen and thawed, whilst temperature was recorded. A similar method as in Chapter 2 was used, where temperatures were numerically simulated for various thermal properties. Optimal values for the thermal properties and porosity that best simulated the experiments were determined. However we did not find a clear relation between the thermal properties and porosity and organic matter content where we expected it. The analysis showed that the thermal conductivity and porosity were the two most sensitive parameters. Furthermore, there was a positive relation between grain size, porosity and organic matter content. A long-term sensitivity analysis demonstrated how under various soil compositions, active-layer thawing depths and timing varied.

The progression of the freeze and thaw front plays a crucial role in permafrost dynamics, as it marks the interface between a frozen stationary system, and thawed dynamic system. Freezing and thawing of the liquid water within the soil pores controls the propagation rate of the freeze and thaw front within permafrost, which is a continuous phase change process. Detection and tracking of this front is however difficult using temperature observations, because temperatures remain isothermal at 0°C during the phase change. In **Chapter 4** we evaluate how Electrical Resistivity Tomography (ERT), a non-invasive geophysical observation method, could be used to gather data on the state and progression of the freeze-thaw front of permafrost. However, the ERT observations need to be corrected for variations in resistivity caused by temperature.

As the soil freezes and thaws, the liquid water content decreases, thereby increasing the resistivity of the measurement. We used a column experiment equipped with temperature sensors and electrodes to capture 3D time-lapse ERT observations as the column was frozen and thawed. The results showed that resistivity increased exponentially as expected during freezing. During thawing, the resistivity decreased along a different exponential curve, indicative for hysteresis. The experiment showed that the hysteresis was the result of a difference in the liquid water content between freezing and thawing, where during freezing the resistivity increased at a lower temperatures compared to thawing. This was likely the result of supercooling and metastable nucleation. The chapter highlights how ERT observations collected in the field could be compensated for the temperature effect using the temperature-resistivity relation, although the compensation would be more appropriate for time-lapse observations rather than single observations.

Although this research mainly involves experimental work, the results are both spatially and temporally scalable, representing processes observed in the field. The method to derive soil thermal properties from temperature observations using a 1D numerical model can be applied to other field sites. Likewise, the experimental results demonstrating how the freeze-thaw front could be tracked using ERT and compensated for temperature, prove that ERT could be applied on a larger scale in the field to detect spatial and temporal variation in the subsurface of freezing and thawing permafrost.

There are multiple areas for future work regarding permafrost research. One of which is the inclusion of DOC transport in our current numerical models, which requires additional solute transport parameters to be accurately determined. An improved experimental setup simulating thawing permafrost in combination with groundwater flow and solute transport could be used to provide the necessary information for parameterisation. Also the detection possibilities of ERT in permafrost areas are not yet fully explored, as resistivity observations collected during the experiment contained indication that it is possible to derive the liquid water content fraction over the freeze-thaw interval. To conclude, the consequences of permafrost thaw are interconnected and far reaching. Continuous efforts to monitor and model this phenomena are vital to mitigate the complex challenges posed.

Samenvatting

Verspreid over de aarde liggen grote gebieden die heel het jaar door bevroren zijn. Zulke gebieden zijn bijvoorbeeld te vinden in het Arctische gebied op het Noordelijk Halfrond waaronder in Alaska, Noord-Canada en Siberië, maar ook op het Tibetaans Plateau. Deels zijn deze poolgebieden bedekt met land en zeeijs, maar er zijn ook grote gebieden die bestaan uit permanent bevroren bodems. Als een bodem voor minimaal twee jaar achtereenvolgens bevroren is, wordt het ook wel permafrost genoemd. Permafrost kent veel verschillende vormen en samenstellingen. Het is opgebouwd uit verschillende bodemlagen met elk verschillende bodemeigenschappen, zoals porositeit, organisch stofgehalte en korrelgrootte. Er ligt een grote hoeveelheid organisch materiaal bevroren opgeslagen in permafrost, wat samen een derde van de totale hoeveelheid organische stof op de hele wereld omvat.

Het Arctisch gebied staat echter onder druk. De globale luchttemperatuur neemt sinds de jaren 90 toe door klimaatverandering; een proces waarbij de luchttemperatuur stijgt door toenemende concentraties koolstofdioxide en methaan in de atmosfeer. Boven de Arctische gebieden neemt de luchttemperatuur zelfs vier keer zo snel toe als het globale gemiddelde. Als gevolg van de opwarming van de aarde dooien permafrostgebieden. Dit heeft grote gevolgen, aangezien bacteriën in de permafrost reactiveren bij de warmere temperaturen. Deze bacteriën zetten de opgeslagen organische stof vervolgens om in de broeikasgassen koolstofdioxide en methaan. Door het vrijkomen van deze opgeslagen stoffen, wordt het proces van de opwarming van de aarde versterkt. Om zicht te krijgen op de snelheid waarmee het permafrost dooit en tot welke diepte is kennis nodig over de fundamentele processen die plaatsvinden tijdens het bevriezen en dooien van permafrost.

Numerieke modellen kunnen worden gebruikt om te simuleren hoe energie, in de vorm van temperatuur, over een periode de bodem kan bevriezen en weer opwarmen. Deze warmtetransportmodellen gebruiken we dan ook om te voorspellen hoe dikke permafrost lagen er over een periode van bijvoorbeeld 100 jaar eruit zou kunnen zien onder een bepaald opwarming scenario. Voor het berekenen van deze scenario's, maken warmtetransportmodellen gebruikt van een aantal parameters; de thermische eigenschappen en bodemfysische eigenschappen, zoals porositeit en organisch stofgehalte. De nauwkeurigheid van de simulaties van de warmtetransportmodellen hangt dan ook volledig af van de kalibratie van deze parameters. Echter is het zeer lastig om accurate gegevens van thermische en bodemfysische eigenschappen te verzamelen in permafrostgebieden. Daarom worden vaak standaardwaarden uit de literatuur gebruikt om deze parameters mee te schatten. Dit is alleen onnauwkeurig en zorgt daarmee voor een grote onzekerheid in de uiteindelijke model resultaten. Daarom

is een alternatieve manier nodig om deze thermische en bodemfysische parameters te bepalen met gebruik van bestaande data. Het doel van dit proefschrift is om *de nauwkeurigheid van de parameterisatie van huidige numerieke warmtetransportmodellen die vries-dooi dynamiek simuleren te verbeteren* en *om de observatiemogelijkheden om permafrost dynamiek te observeren zowel in het veld als in het laboratorium uit te breiden.*

In **Hoofdstuk 2** wordt een methode getest waarmee de thermische geleidbaarheid, warmtecapaciteit en porositeit van de bodem kan worden bepaald. Hiervoor wordt een simpel 1-dimensionaal warmtetransportmodel gebruikt in combinatie met temperatuur data verzameld op verschillende dieptes in de bodem van een permafrostgebied op het Tibetaans Plateau. Er is een parameterruimte opgesteld van alle mogelijke combinaties thermische geleidbaarheid, warmtecapaciteit en porositeit, resulterend in totaal 1728 combinaties. Met het warmtetransport model zijn alle parametercombinaties gesimuleerd, wat resulteerde in een unieke temperatuur tijdreeks voor iedere parameter combinatie. Vervolgens zijn alle gemodelleerde temperatuur tijdreeksen vergeleken met de observaties van het Tibetaans Plateau. Tijdens de model evaluatie zijn drie verschillende methodes gebruikt om de optimale parameter combinatie te bepalen die het beste de gemeten observaties simuleert. Afhankelijk van de evaluatiemethode kwamen verschillende parametercombinaties naar voren die het beste de data simuleerden. Om de langetermijneffecten van de verschillen in parameterwaarden te beoordelen zijn de drie optimale parametercombinaties gebruikt om een hypothetische klimaatopwarming van 100-jaar te simuleren. Hieruit bleek dat op de lange termijn er grote onderlinge verschillen ontstaan in de dooidiepte van de actieve laag van het permafrost. De methode om de thermische eigenschappen te bepalen gebaseerd op alleen gemeten temperaturen bleek dus goed te werken, maar er moet wel rekening worden gehouden met de onzekerheid die gepaard gaat met de methode die gebruikt wordt om de beste parametercombinatie te selecteren.

Nu we hadden bewezen dat het mogelijk is om de thermische eigenschappen van permafrost te bepalen met alleen temperatuurdata, was de volgende vraag hoe verschillende bodemeigenschappen zoals korrelgrootte en organisch stofgehalte de thermische eigenschappen beïnvloedde. In **Hoofdstuk 3** is getest hoe verschillende monsters met verschillende korrelgroottes en organisch stofconcentraties bevriezen en dooien in een laboratoriumomgeving. Hierbij is de hypothese dat er relaties bestaan tussen de thermische eigenschappen en de verschillende bodemeigenschappen, waarbij bijvoorbeeld organische stof een lagere thermische geleidbaarheid heeft in vergelijking tot zand. In totaal zijn negen verzadigde kolommen gevuld met verschillende combinaties van korrelgroottes en organische stofgehaltes bevroren en ontdooid, terwijl op verschillende locaties binnen de kolommen de temperatuur is gemeten. Met behulp van een vergelijkbaar warmtetransportmodel als in Hoofdstuk 2, is de tempe-

ratuur tijdens vriezen en dooien in alle kolommen gesimuleerd. Voor iedere kolom is de optimale combinatie van thermische eigenschappen bepaald. Hieruit kwam geen duidelijke trend naar voren met betrekking tot de thermische geleidbaarheid of warmtecapaciteit in relatie tot organische stofgehalte of korrelgrootte. De thermische geleidbaarheid en porositeit bleken beide gevoelige parameters te zijn terwijl variaties in warmtecapaciteit de temperatuurpropagatie minder beïnvloedden. Warmtecapaciteit is daardoor een lastige parameter om met veel zekerheid vast te stellen. Een langetermijnsimulatie van een permafrostgebied met thermische eigenschappen gebaseerd op alle optimale parameter combinaties laat zien dat na een stabiele periode van ruwweg 45 jaar de diepte van de actieve laag snel toeneemt in dikte en niet meer volledig dichtvriest tijdens de winter.

Van oudsher worden temperatuurmetingen gebruikt om permafrost te monitoren. Echter kost het veel tijd en geld om deze sensoren in het veld te plaatsen op verschillende dieptes in de bodem. Daarnaast ondergaat permafrost dat zich rond het vries/dooi punt bevindt een faseovergang. Temperaturen zijn dan stabiel 0 °C, terwijl het water in de poriën verandert van een vloeistof (water) naar vast (ijs). Een andere methode om permafrost te monitoren, is met het gebruik van elektriciteitweerstandsmetingen, in het Engels ook wel afgekort naar ERT. Het nadeel is echter dat weerstand varieert met temperatuur, wat nadelig is bij het bestuderen van permafrost vries-dooi cycli. De weerstandsmetingen moeten hiervoor dan ook gecorrigeerd worden. In **Hoofdstuk 4** wordt een experimentele kolomopstelling gedemonstreerd waarmee een bodemmonster wordt bevroren en ontdooid. Tijdens het vriezen en dooien is met ERT in een 3D-vlak de weerstand gemeten en met temperatuursensoren de temperatuur. Uit de resultaten blijkt dat het vries- en dooifront duidelijk te meten is met ERT, door de scherpe toename in weerstand als het materiaal bevroren is. Ook is er een duidelijke relatie gevonden tussen weerstand en temperatuur, wat het mogelijk maakt om in de toekomst ERT metingen te corrigeren voor variaties in temperatuur. Aanvullend blijkt ook uit de weerstandsmetingen dat er hysterese zit in het vries- en dooipatroon. Dit komt door de fenomenen supercooling en metastabiele nucleatie die plaatsvinden tijdens het vriezen, maar niet tijdens het dooien.

Het onderzoek heeft aangetoond dat accurate parameterisatie van numerieke warmtetransportmodellen van belang is voor de nauwkeurigheid van de voorspellingen. In **Hoofdstuk 5** worden de implicaties van dit onderzoek geëvalueerd en de onderzoeksvragen beantwoord. Concluderend kan met behulp van numerieke warmtetransportmodellen de thermische eigenschappen van de ondergrond worden bepaald zonder deze expliciet te meten. Deze methode kan wijdverspreid worden toegepast op bestaande temperatuur-tijdreeksen die worden verzameld in permafrostgebieden. Hiermee kan een ruimtelijk patroon van thermische eigenschappen worden bepaald,

wat van belang is voor het modelleren van permafrost vries- en dooi dynamieken over grote gebieden. Door de thermische eigenschappen van permafrost numeriek te bepalen, kan de onzekerheid van langetermijn permafrostvoorspellingen worden gereduceerd. De toepassingen om met ERT permafrost dynamiek te monitoren nemen toe door de observaties te corrigeren voor variaties in temperatuur. Hiermee is het een geschikte non-invasieve methode om het vries- en dooifront mee te detecteren.

Acknowledgements

You have reached the final chapter of my thesis. For those of you who have read all previous chapters, I hope you enjoyed reading it, for those who have skipped some parts, I fully understand. Here I would like to take the opportunity to thank all of the people who have supported me during my PhD.

First of all I would like to thank my supervisors Victor and Martine for giving me the opportunity to be part of the CARBOFLOW project and guiding me through all my phases of my PhD. Victor, thank you for all the freedom you gave me to shape the project and positive support during the seemingly never-ending experiments. Furthermore, I really appreciate the nice discussions we have had and the clear feedback you have always provided from different perspectives, which made me critically review my work. Martine, thank you for all your support and positive feedback on my work. Your pragmatic view kept the project moving forward as I could sometimes find myself spending a lot of time on tiny details. Additionally, I much appreciate the many opportunities you both have provided me with to be involved in education, taking me along with fieldwork not necessarily always related to my work, which I have always found to be refreshing next to my own project.

The research would not have been possible without all the technical support I received. Pieter, you have made an invaluable contribution to my PhD. Next to the many hours we have spent on designing the technical details of the setup, I really enjoyed the coffee breaks we had, having all sorts of technical discussions, whether or not related to work. Additionally, I would like to thank Harm, David and everyone from Tupola and the Unifarm for the contributions to my lab work.

Henk and Linda, thank you for the willingness to help me as my paranymphs. With you guys around at the office, there hasn't been a day without laughter. Next to that, many thanks to my other office mates Ruben, Daan and Henk, all part of the (recently dubbed) man cave office. We've always had a great atmosphere, both figuratively and literally, in our office, which makes it a pleasure to work at the office. Furthermore, many thanks to all of the PhD's and Post doc's in our hallway, Roeland, Reinier, Rose, Mo, Rahel, Nazwa, Janneke, Marjanne, Judith, Sjoukje, Iris and Joris for the many nice breaks and sometimes quite distracting outbreaks of laughter.

Thanks to all the other supportive colleagues at HWM, it is really nice to be part of such an open inviting group. I have enjoyed the nice lunch walks, discussions and the many activities, such as the writing weeks, the field excursions to Limburg, Hupsel and the Ardennes. Especially many thanks to Roel, Ryan, Martine, Tessa, Sjoukje,

and Janneke for the great week and lots of fun we had in Iceland.

A big thanks goes out to my family, parents, brother and sister, and friends, for always supporting me and showing the interest in my PhD work, despite my perhaps somewhat vague descriptions of permafrost and numerical models. Last but not least, Nienke, thank you for the unwavering support you gave me throughout my entire PhD and for being always there. I'm eagerly anticipating all the wonderful experiences we'll share as we journey into the future together.

Jelte de Bruin
Wageningen, May 2024

List of publications

Peer-reviewed journal papers | In this thesis

de Bruin, J. G. H., Bense, V. F., van der Ploeg, M. J. (2021). Inferring Permafrost Active Layer Thermal Properties From Numerical Model Optimization, *Geophysical Research Letters*, 48, e2021GL093306, doi:10.1029/2021GL093306.

de Bruin, J. G. H., Bense, V. F., van der Ploeg, M. J. (2023). Soil thermal properties during freeze–thaw dynamics as function of variable organic carbon and grain size distribution, *Vadose Zone Journal*, 22(3), e20252, doi:10.1002/vzj2.20252.

Journal paper in preparation | In this thesis

de Bruin, J. G. H., Bense, V. F., van der Ploeg, M. J., Binley, A., (2024). Large scale column experiment using 3D time-lapse electrical resistivity tomography (ERT) to investigate the permafrost freeze-thaw front, *Submitted to Geophysical Research Letters*.

Peer-reviewed journal papers | Other

Bense, V. F., Kurylyk, B. L., de Bruin, J. G. H., Visser, P., (2020). Repeated Subsurface Thermal Profiling to Reveal Temporal Variability in Deep Groundwater Flow Conditions, *Water Resources Research*, 65(6), e2019WR026913, 10.1029/2019WR026913.

Netherlands Research School for the
Socio-Economic and Natural Sciences of the Environment

D I P L O M A

for specialised PhD training

The Netherlands research school for the
Socio-Economic and Natural Sciences of the Environment
(SENSE) declares that

Jelte Geert Hendrik de Bruin

born on the 11th of July 1994 in Ede, The Netherlands

has successfully fulfilled all requirements of the
educational PhD programme of SENSE.

Wageningen, the 26th of June 2024

SENSE coordinator PhD education	The SENSE Director
Dr Ir Peter Vermeulen	Dr Jampel Dell'Angelo

The SENSE Research School declares that **Jelte Geert Hendrik de Bruin** has successfully fulfilled all requirements of the educational PhD programme of SENSE with a work load of 41.5 EC, including the following activities:

SENSE PhD Courses

- Environmental research in context (2019)
- Embracing openness: an introduction to Open Science practices (2023)
- Research in context activity: Distributing geophysics across disciplines (2024)

Other PhD and Advanced MSc Courses

- Project and Time management, Wageningen University (2023)

Management and Didactic Skills Training

- Supervising MSc student with thesis '*Estimating Thermal Properties by Numerical Modelling of Active Layer Temperature Changes*' (2019)
- Setting, executing and managing a research project for Vitens (2023)
- Teaching in the BSc courses 'Field Practical Hydrology, Water Quality and Meteorology (2019-2020) and 'Hydrogeology' (2019+2021), and the MSc courses 'Catchment and Climate Hydrology' (2022) and 'Advanced Hydrogeology' (2023)
- Organising field excursion for BSc courses 'Field Practical Hydrology, Water Quality and Meteorology (2023)

Oral Presentations

- *Discovering the missing link between groundwater flow and carbon transport in a thawing permafrost environment.* EGU General Assembly – CatchNet splinter 7-12 April 2019, Vienna, Austria
- *Inferring permafrost thermal properties from freeze-thaw column experiments and numerical modelling.* EGU conference 2022, 23-27 May 2022, Vienna Austria
- ***Best outstanding student and PhD candidate award*** *for: Detecting permafrost freeze-thaw front propagation using time- laps ERT observations in a large column experiment.* EGU conference 2023, 24-28 April 2023, Vienna, Austria

The research was financially fully funded by the Dutch Research Council (NWO) under the project name CARBOFLOW and Grant number ALWOP.237. The research was carried out at the Hydrology and Environmental Hydraulics Group, Department of Environmental Sciences, Wageningen University & Research (Wageningen, the Netherlands). Financial support from Wageningen University for printing this thesis is gratefully acknowledged.

Cover design	Jelte de Bruin
Layout	Jelte de Bruin, using LaTeX 2ε
Printed by	ProefschriftMaken on FSC-certified paper